12-2013

Structure and Energetics of Nanoparticles and Ionomer Films in Fuel Cell Catalyst Layers

Qianping He
University of Tennessee - Knoxville, qhe5@utk.edu

To the Graduate Council:

I am submitting herewith a dissertation written by Qianping He entitled "Structure and Energetics of Nanoparticles and Ionomer Films in Fuel Cell Catalyst Layers." I have examined the final electronic copy of this dissertation for form and content and recommend that it be accepted in partial fulfillment of the requirements for the degree of Doctor of Philosophy, with a major in Chemical Engineering.

David J. Keffer, David C. Joy, Major Professor

We have read this dissertation and recommend its acceptance:

Gerd Duscher, Ramki Kalyanaraman

Accepted for the Council:

Carolyn R. Hodges

Vice Provost and Dean of the Graduate School

(Original signatures are on file with official student records.)

Structure and Energetics of Nanoparticles and Ionomer Films in Fuel Cell Catalyst Layers

A Dissertation Presented for the

Doctor of Philosophy

Degree

The University of Tennessee, Knoxville

Qianping He

December 2013

DEDICATION

I dedicate this work to my wonderful parents, who didn't even understand a single word of this dissertation, but they carefully went over this work page by page. I would never be where I am today without their nurturing, guidance, love and care throughout my childhood, teenage years and young adult years. I love you, Mom and Dad!

To my husband, who never gave up on me and accompanied me during this long and tough journey. You make me want to be a better woman!

To my dear sister, who always fights over everything with me when we are together, but who misses me a lot when we are apart. Thank you very much for taking care of our parents and making me feel less guilty when I cannot spend holidays at home.

To my close friend (Zhao Wu), who is such a good listener when I need to talk. She never judges and I always feel much better after talking to her.

Of course, enough cannot be said to my advisors David C. Joy and David J. Keffer. Dr. Joy taught me how to use the microscope by hand. I will never forget the day that he sat on his knees and taught me how to get the best resolution image. Unlike other famous professors, he is always there for me when I need him.

Dr. Keffer is the most organized person I've ever met in my life. If it were not for him, it would never have been possible for me to publish any papers before graduation. He helped me develop a lot of good habits that will benefit me all of my life. He is the kind of professor who cares about getting the students graduated from school. I feel very lucky to have him as one of my major professors.

ACKNOWLEDGEMENTS

This work is supported by the National Science Foundation through Grant No. DGE0801470, "Sustainable Technology through Advanced Interdisciplinary Research" (STAIR), awarded to the University of Tennessee, Knoxville.

Experimental parts of this work were conducted at the Center for Nanophase Materials Sciences at Oak Ridge National Laboratory (ORNL), sponsored by the Scientific User Facilities Division, Office of Basic Energy Sciences, and U.S. Department of Energy.

There have been a number of people along the way that have made this journey come to a successful end. Jane Breder, program coordinator in the STAIR program, took care of everything else to let us focus on science. Dale Hensley and Jihua Chen, ORNL staff scientists, offered me every help I needed to finish my experiments. And to my fellow STAIR students, I am grateful to be part of this talented and diverse group. Also to my committee members, Prof. Ramki Kalyanaraman and Prof. Gerd Dusher, thank you very much for their valuable advises and being flexible on scheduling the defense date.

ABSTRACT

Improving the durability and utilization efficiency of the platinum-on-carbon (Pt/C) catalyst is of vital importance to the commercialization of polymer electrolyte membrane fuel cells (PEMFC). This body of work provides molecular level insights to aid the fulfillment of this goal. Task 1 describes the use of molecular dynamics (MD) simulation in an effort to understand the Pt/C degradation issue from the nano-adhesion point of view. The roles of catalyst nanoparticle size, shape, Pt/C surface oxidation and the extent of ionomer film hydration are investigated to study their effects on nano-particle adhesion. It is found that the adhesion force strengthens as the Pt size goes up. Nanoparticles of tetrahedral shape exhibit relatively stronger connection with the carbon. The hydroxylated surface enhances nano-adhesion and epoxidized surface diminishes the adhesion. The presence of ionomer film strengthens the adhesion. Task 2 uses MD simulations to investigate the microstructure of the catalyst layer, which is essential information needed for increasing the catalyst utilization rate. The ionomer film thickness, hydration level, surface oxidation of Pt/C, presence of Pt or PtO catalysts are key variables studied for their effects on the catalyst layer microstructure and transport properties. It is concluded that the oxidation of the carbon surface and the presence of Pt or PtO catalyst drastically influence the ionomer film configuration and the water distribution on the surface. The thickness of the ionomer film is directly related with its ability to retain water. Task 3 describes experimental work exploring the effect of radiation damage on the microscopic characterization of the catalyst layer of PEMFCs. It

also provides information on the feasibility of in-situ nano-adhesion measurements inside the SEM. It is found that the radiation damage of the catalyst sample usually starts from the interface of Pt/C and primarily occurs in the form of mass loss accompanied by atomic displacement and edge curl. The results indicate the low reliability of the in-situ nano-adhesion measurement. All three tasks serve to expand the fundamental understanding of the microstructure of the catalyst layer, which contribute to the development of a more durable, less expensive and better performing PEMFC.

Table of Contents

LIST OF TABLES

LIST OF FIGURES

CHAPTER 1: INTRODUCTION

Due to the fact that natural fossil fuel resources are being depleted and the negative consequences caused by use of fossil fuels as a power source, such as severe pollution, extensive mining of the world's resources, and political control and domination of countries that have extensive resources[1], a new power source is needed that is energy efficient, has low pollutant emissions and has an unlimited supply of fuel. Hydrogen can fulfill all of the global power needs while meeting the efficiency and environmental expectations. Technological improvements to fuel cells, which are the devices that convert chemical energy stored in hydrogen to electrical energy, are necessary before the widespread adoption of the hydrogen powered economy.

Polymer electrolyte membrane fuel cells (PEMFCs) are the most popular type of fuel cell, due to their high energy conversion efficiency and power density, fast startup and low/zero emission level[2]. Yet, despite these advantages, there are still several hurdles that prevent PEMFCs from being competitive to existing power sources. The high cost associated with the use of carbon supported catalysts and system early failure due to component degradation are two of the major hurdles that mitigate the advantages inherent in PEMFCs for commercial applications[3]. The need for improving the carbon supported catalyst durability as well as increasing catalyst utilization rate is pressing.

Carbon Supported Catalyst Degradation

The U.S. Department of Energy (DOE) lifetime targets for 2015 are 5000 h for transportation power systems and 40,000 h for stationary power systems[4], while the current PEMFC technology yields only 1700 h and 10,000 h, respectively[5]. One of the major causes of the relatively short lifetime of fuel cells is degradation of the fuel cell components[2], especially the degradation of carbon support catalysts[6].

Carbon supported platinum catalysts (Pt/C) have remained among the most preferable carbon support catalysts materials for PEMFCs. They have very high kinetics for the hydrogen oxidation reaction (HOR) and one of the best electrode performances at low temperature and in the acidic environment inside PEMFCs[7]. However, both the platinum catalyst and carbon support suffer from deactivation. For example, previous studies have found that platinum (Pt) particles suffer from poor durability and will rapidly lose electrochemical surface area (ESA) under operation[8-13]. The process is usually accompanied by the of Pt nanoparticle growth (Pt deactivation). Ferreira et al. proposed three fundamentally different mechanisms of Pt deactivation: (i) platinum dissolution and redeposition (the Ostwald ripening process), (ii) coalescence of platinum nanoparticles via platinum nanocrystalline migration on the carbon support and (iii) platinum particle agglomeration triggered by detachment of Pt particles from the carbon support (caused by carbon corrosion)[8]. Recently, Mayrhofer et al. proposed a new corrosion mechanism for Pt catalyst, demonstrating that whole Pt particles can detach from the support and dissolve into the electrolyte without redeposition[14]. Huang's group also reported the observation of detachment of small Pt clusters from the carbon support

in their MD simulations[15]. In addition, TEM images of catalyst materials before and after testing indicate that many platinum particles are not sufficiently anchored to the carbon support and move into the ionomer portion of the catalyst layer before testing, such as potential cycling[16]. Furthermore, Groves et al. has attributed the Pt catalyst detachment and agglomeration to the weak interaction between the Pt and carbon support[17]. This mechanism is also mentioned in several review papers regarding the durability enhancement of carbon supported platinum catalysts[18,19]. Experimental evidence also substantiates the link between binding energy and catalyst durability. For example, doping fullerenes with nitrogen increases the binding energy and also shows an increase in dispersion of platinum, a resistance to agglomeration of nanoparticles, and a less significant deterioration of activity when compared with pure carbon cases[20-25]. This example also indicates that surface functional groups on the carbon support catalysts can influence the catalyst durability by changing the binding energy between the support and the catalyst.

The oxidation of both the carbon support and platinum nanoparticles is another well-accepted phenomenon that could cause Pt/C degradation during PEMFC operation[26]. Activated carbon is subject to oxidizing conditions in its various applications, i.e. the carbon surface can be covered by different surface oxygen groups or even experience CO_2 evolution during operation[27]. Both can greatly change the chemical and textural characteristics of the carbon support surface and thus further influence the interaction between the carbon support and the Pt nanoparticles. It is believed that CO_2 evaporation results in a weaker interaction between the carbon support and the Pt nanoparticles, as a

result of which, Pt will be lost from the electrode and aggregate to larger particles, resulting in a reduction in the electrochemically active surface area and corresponding loss of catalyst activity[19]. However, there are different opinions on how the presence of surface oxygen groups affects the interaction between the carbon support and the Pt nanoparticles. According to Giordano and co-workers, the surface oxygen-containing complexes facilitate the CO_2 evolution, which results in a weakened interaction between the carbon support and the metal nanoparticles[28,29]. Colmenares et al. has also achieved similar conclusions recently[30]. Kinoshita and Bett, however, believe that oxidation of carbon to CO_2 is inhibited by the formation of stable carbon oxides[27]. In other words, stable carbon surface oxides can prevent the Pt nano-particle loss due to CO_2 evolution.

Similar to the carbon support, the catalyst metal also undergoes oxidation by direct reaction with oxygen or by reactions through water oxidations in aqueous solution, which is regarded as one of the most important interfacial processes in surface science, electrocatalysis, and corrosion science[31]. The role of oxidized Pt compounds in the reactivity of Pt is still under debate. It has been suggested that oxidized Pt surfaces are more reactive than metallic Pt for CO oxidation[32-35]. Dam et al. showed that Pt dissolution in fuel cells is reduced when a protective oxide layer is present[36]. Hull et al. reported high reactivity for PtOx(Shell)/Pt(core)-carbon nanotube catalysts[37]. However, Gasteiger et al. believe that the formation of PtO and subsequent Pt dissolution are the reason for the temporal decay in the performance of Pt-based fuel cell electrodes[38].

Many of the Pt/C degradation mechanisms discussed above originate in detachment of the Pt nanoparticle from the substrate surface, which could possibly arise

from a weak binding energy between the catalyst and the carbon support. When the interaction between Pt and its substrate is not strong enough, nanoparticle detachment could easily happen under certain conditions. For example, the mechanical vibration during the automobile transportation when fuel cells are used as an alternative energy source in vehicular applications could cause shearing stresses between the bipolar plate (BP), gas diffusion layer (GDL) and membrane electrode assembly (MEA), which may lead to the deformation of MEA including the catalyst layer. The deformation of materials surrounding the Pt nanoparticles on the carbon substrate may cause the Pt nanoparticle to detach from the carbon substrate, especially in cases when Pt nanoparticles are not sufficiently anchored to the carbon support. Also, the surface texture change may affect the adhesion between the catalyst and the support and causing subsequent catalyst detachment and agglomeration.

Investigating the nanoparticle adhesion between Pt and its carbon support could help us characterize the strength of the nanoparticle interaction with the substrate, and thus allow us to estimate how easily catalysts could be detached from the carbon support, providing both a better fundamental understanding of the mechanisms in ESA loss as well as shedding light on addressing practical issues such as how to improve the Pt/C catalyst durability.

Increasing Carbon Support Catalyst Utilization Rate

A more efficient utilization of all catalyst present[39] requires a fundamental understanding of the catalyst layer nanostructure. The key to excellent performance with low catalyst loading is the creation of an optimized contact area between the

membrane/catalyst/support/vapor interfaces in the catalyst layer to ensure good electronic and ionic conductivities[40]. Wilson et al.[39], proposed the 'thin film catalyst layer' (5-10 μm[41,42]) that possesses optimized properties of thinness, uniformity and the proper ratio of ionomers and supported catalyst in the catalyst layer of PEMFCs and found a substantial increase in the specific activities of the Pt catalyst compared to the conventional catalyst layer. They specifically emphasized the effect of catalyst layer thickness on fuel cell performance.

The catalyst layer typically contains recast ionomer in order to provide a pathway for proton transport from the catalyst nanoparticle to the polymer electrolyte membrane (PEM). This ionomer is thought to form a film on the catalyst support. Cheng et al. illustrated the necessity of a thin ionomer film (less than 15 nm, usually proportional to the radius of an agglomerated particle that is composed of the ionomer, gas voids, liquid water and catalyst[43,44]) around the supported catalyst by showing that low Pt catalyst utilization can result from catalyst particles being covered by "thick Nafion layers or clumps" from scanning and transmission electron microscopy (SEM/TEM) images of the thin film catalyst[45]. Nafion, a perfluorosulfonic acid polymer electrolyte, is the current industry standard used in proton exchange membranes. It is also used as "recast ionomer" in the catalyst layer to form the ionomer film. Recently, Samsung has been working on increasing the catalyst utilization with ionomer nano-dispersion, which is a technique that allows control of ionomer dimension in the catalyst layer to ensure that it is thin and homogeneously distributed around the Pt/C nanoparticle[46]. In their report, they introduce the concept of an interfacial bonding layer to represent the thin interface

between the catalyst layer and the membrane electrolyte. They illustrate the importance of the microstructure of this interfacial bonding layer on proton transfer[46]. A schematic of the interface between the catalyst layer and the polymer electrolyte membrane is shown in **Figure 1**. The red rectangular denotes the location of interfacial bonding layer of the anode. The details of the microstructure in this area remain unknown. However, it is clear that the performance of fuel cell can be improved if a better control of the structure in the interfacial bonding layer and the catalyst layer as a whole is possible. A fundamental understanding of the structure/property relationships at work in the catalyst layer can provide guidance for the further development of optimized devices.

In addition to the thickness of the ionomer film, there are other features that influence catalyst utilization and fuel cell performance. The oxidation states of both platinum nanoparticle and the carbon support are among them. The carbon supported platinum catalyst (Pt/C) undergoes oxidation under PEMFC operation[19], which can greatly change the chemical nature of the surface as well as the surface roughness, both of which may impact interactions with catalyst nanoparticles and the ionomer film.

Another feature that influences catalyst utilization and fuel cell performance is the humidity level, which has a strong effect on the morphology of the hydrated ionomer film. The effect of humidity level on the morphology of the "bulk" hydrated membrane has been extensively studied both experimentally and theoretically[47-65]. It is generally accepted that hydrated Nafion exhibits a morphology with nanophase-segregation, consisting of a hydrophobic domain (fluorinated polymer backbone) and a hydrophilic domain (water, sulfonate groups, etc.)[66]. The isolated hydrophilic domain of the Nafion

at lower water contents will increase in size and eventually form continuous channels at higher hydration levels[67]. However, most of these studies have been focused on the bulk phase, which might exhibit different features compared with the Nafion thin film located at the interface. Theoretical work has been published on the molecular-level structure of membrane/catalyst/vapor and membrane/support/vapor interfaces previously by our group[68]. However, the local nanoscale structure of the membrane/catalyst/support/vapor interfaces, especially under the influence of variations of film thickness and surface oxidations, remains unexplored.

Purpose of This Work

Improving carbon supported catalyst durability and increasing carbon support catalyst utilization rate are two inherently related tasks, which are closely connected with the catalyst layer interfacial structure and are influenced by a set of synthesis and operating variables such as the ionomer film thickness, film hydration level, oxidation state of the contacting surface, etc. The work presented here contains three tasks to address the above mentioned issues. Task 1 calculated the nanoparticle adhesion between the catalyst and their carbon support to tackle the carbon support degradation issue. Task 2 examines the microstructure and properties of the interfacial layer of the catalyst under various operation conditions such as loss of Pt catalyst (Pt detachment), presence of surface oxidation, different thicknesses of the ionomer film as well as different hydration levels. In these two tasks, molecular dynamic simulations were conducted as the major investigating tool. Experimental investigation of the structure and energetics of the nanoparticles and ionomer film of the PEMFC catalyst layer via

electron microscopy is equally important. It provides us with direct evidence of the nanoscale structure and energetics. However, the inevitable feature of the electron microscope, i.e. the electron radiation damage, might introduce uncertainty and inaccuracy to the acquired experimental results. To understand the effect of electron radiation damage on the measurement of nano-adhesion between nanoparticles and its effect on the nano-structure characterization, task 3 is included as the last portion of this dissertation. In task 3, experimental work is presented as a preliminary attempt to evaluate the possibility of measuring the Pt/C nanoparticle adhesion in-situ from the SEM chamber. This task also helps to understand the effect of radiation damage on microscopic characterization of the catalyst layer. The information from these studies could be applied to the development of more durable Pt/C catalyst and optimizing the interfacial structure of the catalyst layer.

CHAPTER 2: SIMULATION METHODOLOGY

Molecular dynamics (MD) simulations is a computer simulation based on classical physics at the atomistic level. It generates information such as atom positions and velocities by numerically solving the Newton's equation of motion given an intermolecular potential. In the MD simulations, the force and potential between interacting atoms are defined by a molecular mechanics force field, an input. The technique is widely applied in chemical physics, material science and modeling of biomolecules[69].

In the molecular dynamics portion of the work (Tasks 1 and 2), classical molecular dynamics simulations in the canonical (NVT) ensemble are performed using an in-house code written in Fortran 90 and parallelized using MPI. A non-cubic parallelogram shape for the volume is used in this simulation to accommodate the crystallographic unit cell of the graphite surface. The simulation box has an x-length of 14.7 nm, y-length of 17.3 nm and z-length of 40.0 nm. The z-length was chosen to be sufficiently large to avoid non-physical contributions from periodic images of the system in the z-dimension. The angle from x-axis to y-axis is equal to 60°. The Nosé-Hoover thermostat is employed to maintain the system at a constant temperature of 298 K[70,71]. The two timescale r-RESPA method is incorporated to integrate the equations of motion with 1 fs for the large time step size and 0.1 fs for the intramolecular degrees of freedom[72].

Molecular Dynamics simulations require as input initial geometries as well as interaction potentials between all atoms. In the following section, we first describe the geometry of the unoxidized Pt nanoparticles, unoxidized carbon surface, oxidized Pt nanoparticle, oxidized surfaces and ionomer. We then present interaction potentials for all components in the simulation including the ionomer (Nafion), water, hydronium ions, pristine and oxidized graphite and pristine and oxidized Pt nanoparticles.

Molecular Models

Platinum Nanoparticle Model

Catalytic activity of Pt nanoparticles is strongly dependent on the particle size, shape and morphology. With advances in modern synthetic technology, Pt nanoparticles can be synthesized with various shapes (cubes, tetrahedrons, octahedrons, decahedrons, icosahedrons) bounded by different number of facets and with different defects[20,73,74]. Many of these shapes have been found successfully synthesized in a Nafion recast film with high yields[75-77]. In this work, four Pt nanoparticle shapes—cubic, tetrahedral, truncated octahedral and octahedral nanoparticles—were simulated. For each shape, three nominal sizes—2 nm, 4 nm and 6 nm—were simulated. The number of atoms in the nanoparticle ranged from 56 (2 nm tetrahedron) to 14896 (6 nm cube). As to the choice of nanoparticle size, we followed Ferreira et al[8], who performed a size distribution analysis of 200 Pt nanoparticles in the pristine Pt/C sample and powders scraped from the cycled membrane electrode assembly (MEA) cathode surface. They found a mean particle diameter of 2.8 nm for pristine Pt/C and 5.9 nm for the cycled sample.

The model nanoparticles were obtained from the bulk Pt crystal with an fcc structure, with corresponding lattice parameters ($a = b = c = 0.392420$ nm and $\alpha = \beta = \gamma = 90°$) and space group of Fm-3m[78]. The various shaped nanoparticles were obtained by making cuts in the bulk crystal along the appropriate planes. The cutting planes were different depending on the shape and were always parallel to the face that had to be exposed in each case. For example for the cubic shape, three cuts were made with planes parallel to the {1 0 0}, {0 1 0} and {0 0 1} faces. Thus a cubic particle enclosed by six 1 0 0 faces was built. The Pt models used in this work are defect free. While it is known that there are slight changes in lattice parameter as the size of the Pt nanoparticle decreases, that effect was not incorporated here[79]. Snapshots of the isolated Pt nanoparticles used in the simulation are shown in **Figure 2**. It should be mentioned that in this work Pt nanoparticles remain isolated since this work focuses on the interaction between Pt and its carbon support rather than the interaction among Pt nanoparticles. The agglomeration of Pt nanoparticles has not been considered in the simulations.

Pristine Carbon Support Model

Although carbon black (amorphous carbon) such as Vulcan XC-72 from E-TEK has been commonly used in industry as the carbon support for PEM fuel cells at the current stage [80], the carbon electrode is modeled as graphite here. The choice is justified as follows. First, compared with the amorphous carbon, graphite possesses more π sites (sp^2-hybridized carbon), which play the role of anchoring centers for Pt[81] and thus result in a strengthened metal-support interaction and resistance of Pt to sintering[82]. Second, with advances in catalyst structure, graphitized carbon support with enhanced catalyst

activity has improved[83-86]. Third, increasing attention is paid on the application of graphitic carbon (e.g. graphite nanofibers) as the catalyst support[87-89]. Last but not the least, there is a strong similarity in the structure of graphite and graphite nanofibers and the preponderance of data is available for the graphite model. The model is thus built by first obtaining a unit cell structure with corresponding unit cell parameters (a = 0.2461 nm, c = 0.6708 nm, Z = 4) and space group ($P6_3/mmc$)[90]. The unit cell is extended in x, y, z directions until the targeted size is achieved. The final structure used in our simulations contains seven layers to meet our cut-off distance (2.1 nm). The employment of the 7-layer graphite model is further justified by a calculation of the contribution of each graphite layer to the potential energy result. According to the calculation, it is found that at equilibrium separation distance (~ 0.3 nm), the first and second layer of the graphite contribute more than 99% to the results. And with the separation distance increasing, the role of the latter layers of graphite become important, for example, at 1.3 nm separation distance, the first three layers contribute 70%, 20% and 7% to the results respectively; and at largest separation distance, an almost even contribution of each layer to the result is obtained. However, since the potential energy approaches zero at large separation distance, the contribution distribution does not really matters. Thus, 7 layers are believed to be sufficient for the graphite model in the simulation. The lateral dimensions of the graphite slab are 17.3 nm and 14.7 nm. A snapshot of the graphite model used in our simulation is shown in **Figure 3**. In this work, we did not include textural defects on the pristine graphite surface, only the perfect graphite model is

considered. Snapshots and interactive structures of every system simulated and presented in this thesis are available in an online archival site[91].

Oxidized Platinum Nanoparticle Model

The oxidized platinum nanoparticle is modeled as PtO. Ono et al. reported that PtO is the dominant species stabilized on Pt nanoparticles supported on nanocrystalline oxides[92-94]. The PtO model has not been used in MD simulation before to the author's best knowledge. The precise structure of the PtO model is obtained according to Imai et al., who performed *in situ* and real-time monitoring of oxide growth at the surface of Pt nanoparticles in aqueous media, and proposed a molecular model of surface oxides on Pt 111 model surface[31]. Considering the fact that the PtO model is based on Pt 111 surface, we chose the Pt nanoparticle in a tetrahedron shape, since the tetrahedron Pt nanoparticle exposes four 111 faces. The nominal size of the tetrahedron Pt nanoparticles is chosen to be 4 nm, which is within the range of nanoparticle size distribution in the Pt/C sample[8]. Atomic oxygen atoms are then placed at every fcc-hollow site on the surface layer of Pt with a Pt-O bond length of 2.0 Å[31]. The finished PtO model thus has one monolayer of atomic oxygen atoms covered on the surface of the platinum nanoparticle. The inner core of the PtO nanoparticle is not affected by oxidation. A snapshot of the isolated PtO nanoparticles used in the simulation is shown in **Figure 4.** It should be pointed out here again that the agglomeration of PtO nanoparticles has not been considered in this work, and our nanoparticles remain isolated. The internal structure of the PtO nanoparticle is considered rigid as well.

As for the charge transfer from Pt to the absorbed oxygen species, x-ray absorption near edge structures (XANES) analysis indicated that the charge transfer is small and constant and is about 0.5 electrons per oxygen[31]. XANES analysis also indicates that the electronic alteration only occurs at the surface[31]. Based on these facts, the partial charge on the oxygen of PtO (total of 484 oxygen atoms in a 4 nm PtO) is fixed to be -0.5 e, and the partial charge on the Pt atoms that are in direct contact with the oxygen atom (total of 244 atoms in a 4 nm PtO) is 0.9918 e. For Pt atoms that are not on the surface, the charge is zero. This distribution results in a PtO nanoparticle with net zero charge.

Oxidized Carbon Support Model

The oxidized carbon support is modeled as a seven-layer graphite slab with surface epoxy groups or surface hydroxyl groups on the top graphene layer. The epoxy and hydroxyl functional groups are chosen as a relevant and appropriate form of carbon oxidation based on the results from NMR as well as predictions of first-principles atomistic modeling that has been verified by atomic force microscopy[95,96]. The oxygen atom is located 1.9 Å above the top carbon layer. The hydrogen atom of the hydroxyl group is 2.2 Å above the carbon grid. The bond length of O-H in the hydroxyl group is 0.96 Å as reported[97]. The graphite slab is identical as the model we used for pristine graphite. The graphite slab is either oxidized by epoxy groups or by hydroxyl groups. Mixed oxidation is not considered. In this work, we did not include vacancies and topological defects on the oxidized carbon surface, although a separate study of those effects would also be interesting. For each functional group, three oxidation extents—

10%, 25% and 50%—were chosen based on the results of Schniepp et al[96], who observed C/O ratio between 2:1 to 10:1 for epoxidized/hydroxylated graphite surface. It should be pointed out here that only the top layer of carbon is considered when the number of oxygen atom at each oxidation extent is determined. It should also be noted here that CO_2 evolution, which is considered as an independent carbon corrosion reaction that occurs concurrently but is unrelated with the formation of surface oxides[27] is not investigated in this work. Snapshots of the oxidized graphite are shown in **Figure 5.** As was the case for the PtO nanoparticle, the internal structure of the oxidized carbon surfaces is held rigid.

The oxidized surfaces are electrically neutral, but there is charge distribution at the surface. Based on the lack of information on charge distribution for the oxidized graphite, quantum chemical calculations were performed for a graphene fragment containing 24 carbon atoms with hydrogen capped on the edges and one functional group (epoxy or hydroxyl) located in the center ring. The optimized geometry and the partial charge on each atom were determined via Gaussian03 using the B3LYP functional supplemented with standard 6-311G (d,p) basis set[98,99]. The electron distributions were mapped onto partial charges by performing the natural bond orbital (NBO) analysis[98]. Details on the partial charge of all the atoms in the oxidized graphite are listed in **Table 1.** The determination of the partial charges of the oxidized graphite surface was the only first principles work done in this current contribution. All other potential parameters were taken from the literature.

Nafion, Water and Hydronium Ion Models

Recast polymer electrolyte is frequently included in the catalyst layer in order to provide a path for proton transport from the catalyst particle to the proton exchange membrane. In this work, Nafion, as the most common perfluorosulfonic acid PEM material used industrially, is selected as the recast polymer electrolyte. The model of Nafion used in this work has been previously used to study the bulk hydrated membrane[66,100]. The model consists of 15 monomers with an equivalent weight (EW; the molecular weight of the repeat unit) of 1144. See **Figure 6**. The film thickness is chosen to be nominally 1 nm in the nano-adhesion calculation session (task 1) to avoid the Pt particle being totally buried in the film (our smallest Pt particle measures 2 nm). Experimentally, there is an optimal recast Nafion content in the catalyst layer[101], because too little Nafion fails to provide a path for proton transport and too much buries the catalyst particles, presenting a mass-transfer barrier for the hydrogen fuel (at the anode). This thin film is an attempt to represent the desirable triple phase boundary of Nafion/Pt/gas and the choice of 1 nm thickness is believed to be optimal for the nano-adhesion calculation in this work. The system is analyzed at the λ = 3, 6, 9, 15 H_2O/HSO_3 nominal hydration levels for the pristine Pt/C system. These hydration levels span the range from minimally hydrated to well hydrated[66]. For the oxidized Pt/C system, only the hydration levels of λ = 3 and 9 H_2O/HSO_3 were investigated based on the results obtained from the non-oxidized Pt/C system. The number of each component in the non-oxidized Pt/C system of different hydration levels and different Pt sizes is listed in **Table 2**. The number of each component in the oxidized Pt/C system is the

same as that of the 4 nm Pt systems. A TIP3P model with a flexible OH bond is used for the water model [102,103]. The hydronium ion is similar to that of Urata et al, we use the same partial charges for the oxygen and hydrogen atoms[104].

Force Fields and Potentials

In the adhesion analyses, the LJ interaction potential are widely accepted and used in modeling adhesive contacts[105-107]. The interaction of the carbon of graphite and platinum of the nanoparticle with other atoms in the non-oxidized system are represented by LJ potentials (ε_{Pt}/k = 2336.0 K, σ_{Pt} = 0.241 nm, $\varepsilon_{graphite}/k$ = 28.0 K, $\sigma_{graphite}$ = 0.34 nm)[108-110]. It is worth pointing out here that although the LJ parameters for Pt were originally developed for the simulation of adsorption of Pt on graphite walls, our previous work has proven that it's also suitable to describe the interaction between Pt and organic molecules, such as Nafion, water and hydronium ion based on the fact that our simulations results match quite well with the results obtained from atomic level experiments (scanning tunneling microscope; core-level spectroscopy, i.e. XPS, XES, XAS; He atom scattering spectrum) as well as quantum mechanical calculations (DFT)[111]. It should also be noted that we are aware of the phenomena of deformed nanoparticles with a neck when detaching from the adhesive substrates[112]. In those simulations, the classical Johnson, Kendall, and Roberts (JKR)[113] and the Derjaugin, Muller, and Toporov (DMT)[114] theories are used to describe the adhesive contact between the substrate and nano-particles. However, both JKR and DMT theories are developed for the adhesion of elastic spheres on flat surfaces and their models fail to describe kinetic effects[115]. Moreover, according to Carrillo et al., the nanoparticle shape-

changing process during detachment is accompanied by rupture of adhesion bonds formed between the nanoparticle and the substrate[112]. In other words, the interaction between the nanoparticle and substrate should be large enough to form adhesion bonds so that the nanoparticle shape has to be changed to resist the detachment process. However, the binding energy between Pt and carbon surfaces calculated by the density functional theory has shown that no formal bond is formed between the platinum atom and the pristine carbon surface[17]. There is also no formal bond formed between PtO and oxidized graphite since the equilibrium distance between the bottom layer of PtO and the top layer of the oxidized graphite is much larger than the distance required to form a bond between them. Taking the hydroxylated graphite as an example, the equilibrium distance between the hydroxylated graphite and PtO is 2.60 Å while the bond length of the bond formed between hydroxylated graphite and PtO (the 'O-H' bond) measures 0.983 Å in average according to a recent neutron diffraction study[116]. Similarly, in the epoxidized graphite case, the bond length between 'O-O' is around 1.47 Å[117] and the equilibrium distance is 2.69 Å. Moreover, the presence of the oxide layer on the PtO nanoparticle surface serves as a protective film which actually prevents the nanoparticle from dissolution[36]. Based on the above factors, nanoparticle shape transformation[112] during detachment process is not considered in our simulations.

In the oxidized Pt/C systems, the intramolecular and intermolecular nonbonded interactions are composed of a Lennard-Jones (LJ) potential and a Columbic interaction. Although the force field applied in the work is non-polarizable, it is widely adopted in characterizing the microstructure, morphology and properties of the key components

(catalyst layer and polymer electrolyte) of the fuel cells, including systems with oxidation of Pt and Pt alloy supported nanoparticles over carbon[108-111,118-122]. The results obtained from those simulations were able to match the results from experiment or quantum mechanical simulations quite well[123-127]. The force field is thus justified to use in this work. These classical MD simulations do not allow for ionization of water molecules nor charge delocalization of the hydronium ion to Zundel or Eigen ions. While the presence of these larger ions is crucial for modeling proton transport, it is unclear whether they will have a significant impact on film and nanoparticle adhesion. Given current computational resources, in order to examine the changes in film morphology due to oxidation, these approximate, classical force fields have been used. As explained in the previous paragraph, the internal structure of the graphite layers as well as the PtO nanoparticle are rigid. Their interactions with the dynamic atoms in the system (of Nafion, H_2O and H_3O^+) are represented by LJ potentials and Columbic interactions. Details about the LJ parameter of PtO and the oxidized graphite are listed in **Table 1**. The LJ parameters for oxidized graphite are taken from Wu[109] et al., Lamas et al.[110] and Liem et al.[108] The LJ parameters for PtO are taken from Callejas-Tovar et al[122]. The potentials for Nafion, water and the hydronium ions used in this work is identical to that of our previous work[66]. The Nafion model is fully atomistic except for CF_3, CF_2, and CF. These CF groups are treated as united atom to reduce computational costs [128-131]. The atoms of Nafion, water and hydronium ions are charged, which allows us to take into account the forces among ions. We have included bond stretching, bending, torsion, intramolecular and intermolecular nonbonded interactions via the Lennard-Jones (LJ)

potential and Columbic interactions. The potential parameters of the Nafion model have been reported previously[66,132]. The bond distance, bond angles and force constants of hydronium ion are the same as in the TIP3P model[103]. Structural diffusion of protons is not allowed in our simulation given this potential; however this is not a limitation for the measurement of adhesion energies and forces.

The Lorentz-Berthelot mixing rules are invoked for all interspecies interactions, in order to maintain uniformity in the interaction potential and to remain consistent with the Nafion potential, which used them in its parameterization[128-131]. For the calculation of the electrostatic interactions, the spherically truncated, charge neutralized method of Wolf et al. is applied[133].

Simulation Procedure

In task 1, the nanoparticle supported over the graphite surface was initialized at the bottom of our simulation box with the catalyst nanoparticle (Pt or PtO) sitting in the center of graphite surface at the equilibrium distance of the bare system. The equilibrium distance between the catalyst nanoparticle and graphite is obtained by plotting the LJ potential of the catalyst and graphite versus different separation distances ranging from 0 to 20 nm. The initial configuration of Nafion, water molecules and hydronium ions were randomly placed around the catalyst in the system. In order to avoid a physical overlap, equilibration involved first a brief period (20 ps) of growing the atoms of Nafion, water and hydronium ion, by gradually increasing the LJ collision diameter. "Growing" of atoms is a standard technique for molecular simulation of dense but non-crystalline systems, which allows one to recreate a reasonable molecular-level initial estimate of the

structure that does not contain any overlap of atoms that could potentially result in unphysical large forces. This structure is thoroughly equilibrated before any data production begins. **Figure 7** is a snapshot of an equilibrated system containing a 2 nm cubic Pt nanoparticle at the hydration level of $\lambda = 3$ for the non-oxidized system. The equilibrated system displays several characteristic features. The Nafion molecules form a film on the surface. Some of Nafion forms a film around the nanoparticle. Water molecules and hydronium ions cluster around the sulfonic acid groups. Some small fraction of water molecules enter the vapor phase.

After the system is equilibrated, the catalyst nanoparticle is pulled from the graphite surface along the z-axis at a constant speed of 0.01 nm fs^{-1} to mimic the real detachment process. The choice of constant speed is based on the two facts: firstly, the maximum adhesion force depends weakly on the pulling velocity while the nanoscale intermittent behavior of species during the detachment process depends strongly on the pulling velocity[134]. It is thus believed that the effect investigated in task 1, i.e. the nanoparticle size, shape and the introduction of hydrated polymer on the nanoparticle adhesion etc. will not be affected by the choice of pulling velocity. Secondly, many experiments involving the measurement of nano-adhesion use constant pulling velocity[135,136]. To be compatible with the experiments and to keep our systems comparable, constant pulling speed is applied throughout the simulation. The potential energy and force for the nanoparticle are computed at each separation between nanoparticle and surface. The reported potential energy of the nanoparticle is the sum of all interactions between catalyst atoms and all other atoms in the carbon support and film.

The reported force on the nanoparticle is the z-component (normal to the graphite surface) of the force between catalyst atoms and all other atoms in the carbon support and film. For the readers to understand the results better, a list of major assumptions made in the nano-adhesion calculation is summarized in **Table 3**.

The same equilibration procedure of the simulation systems is applied for microstructure characterization in task 2. In the data production section, the radial distribution functions (RDFs) are calculated instead of the nano-adhesion force and binding energy. In this set of simulations, the microstructure of the Nafion ionomer film is investigated and a new variable 'film thickness' is introduced to study the film thickness effect on the ionomer film conformation.

CHAPTER 3: RESULTS AND DISCUSSION

The results and discussion section are organized into three tasks. In task 1, results of particle detachment simulations are presented. In each of these simulations, a nanoparticle is gradually detached from the carbon substrate surface. When present, the ionomer film is allowed to relax during the detachment process. These detachment simulations provide (i) binding energies, (ii) forces of adhesion, and (iii) molecular-mechanisms for polymer relaxation during the detachment process. The variables of interest include size and shape of nanoparticle, type and extent of oxidation of the nanoparticle and the substrate, as well as the presence and degree of hydration of the ionomer film.

In task 2, results of simulations in which the nanoparticle is allowed to remain at rest on the surface are presented. These simulations provide binding energy of the ionomer film as well as information regarding the nanoscale morphology of the hydrated film. The variables of interest in these simulations include film thickness, degree of hydration, type of oxidation of the nanoparticle and the substrate, and presence of the nanoparticle.

In task 3, results of experimental work examining radiation damage of the catalyst layer during characterization by microscopy are presented. This work provides a radiation damage mechanism of the catalyst layer of the PEMFCs, which is useful for interpreting the microscopic images of the CL sample. The results of this task also serve as preliminary research for measuring the nano-adhesion force inside a microscope. The

signal intensity change with the beam dose accumulation is monitored under different high voltages, scan speeds and sample compositions. EELS and EFTEM results are also included as key components to understand the CL radiation damage mechanism.

Task 1 Nanoparticle Adhesion

We begin the results and discussion section of the nano-adhesion calculation by presenting results from the bare system, in which there is no Nafion or water present. The results of the bare system do not require MD simulations, simply energy and force evaluations as a function of separation between the catalyst nanoparticle and the carbon support surface, which is different from any other systems that contain water and ionomers. The inclusion of the dry systems is intended to provide a baseline by which the impact of water and polymer film can be measured. In the following discussion, we use the term "bare" to indicate the absence of a polymer film on the surface and "clean" to indicate the absence of oxidation on the surface.

Bare Systems

In **Figures 8**(a) and **(b)**, the potential energy and normal force between the Pt and graphite (non-oxidized bare system) are plotted as a function of separation between the nanoparticle and surface for several nanoparticle sizes of cubic shape. Here the separation distance is defined as the distance between the center of carbon atoms forming the top layer of graphite and the center of Pt atoms forming the bottom layer of nanoparticle. The 'bare system' curve represents the cumulative LJ interaction between the nanoparticle and the surface. As shown in figure, when Pt and graphite are far apart,

the interaction energy and force are zero. As the distance of separation decreases, there are dispersive interactions that give rise to a potential energy well and a corresponding attractive (negative) force. There is a minimum in the energy well at a distance where the nanoparticle is resting on the surface. The minimum in this energy well corresponds to the "binding energy". At separations smaller than this equilibrium distance, the force is positive and the energy quickly increases due to repulsion between the C and Pt atoms. The "adhesion force" refers to the minimum in the force curve, or the inflection point in the potential energy.

For a cubic particle of size varying from 2 to 6 nm, the well is deeper for larger particles, simply because there are more Pt atoms in larger particles contributing to the attractive interaction. In **Figures 8(a)** and **(b)**, the net energy and force are plotted on a per particle basis rather than a per atom basis. On a per atom basis, the difference in the force and energy curves as a function of nanoparticle size is reduced, but the curves do not perfectly overlap, because the distribution of distance between Pt and C atoms is different for nanoparticles of different size. It should be pointed out that the binding energy per atom increases in magnitude as the size of the particle decreases, because in small nanoparticles a greater fraction of the Pt atoms are located closer to the minimum in the Lennard-Jones pairwise interaction potential. For example, these three sizes of nanoparticle cubes, the binding energy per Pt atom is -0.0031,-0.00163,-0.00109 aJ/Pt atom respectively with increasing size. It is also observed that the position of the equilibrium distance (where the force is zero) is relatively insensitive to nanoparticle size,

since this position is largely dictated by repulsion between the top layer of graphite and the bottom layer of Pt.

From a quantitative point of view, the binding energies for these cubic nanoparticles on clean graphite range from -16.3 to -2.1 aJ for the 6 nm to the 2 nm nanoparticles respectively. This range of binding energies can be alternatively expressed as -9815 to -1242 kJ/mole of nanoparticles or as -0.66 to -1.9 kJ/mole of Pt atom. Similarly, the adhesion forces for these nanoparticles on clean graphite range from -93.8 to -11.9 nN (per particle) for the 6 nm to the 2 nm nanoparticle respectively.

In **Figures 9(a)** and **(b)**, the potential energy and normal force between the Pt and graphite (bare system) are plotted as a function of separation between the nanoparticle and surface for several nanoparticle shapes with nominal size of 2 nm. The number of Pt atoms in each nanoparticle varies and is reported in **Table 4**. The cube has the most Pt atoms with 666 and the tetrahedron, made by cutting the 2 nm cube into a tetrahedral shape has only 56 atoms. The depth of the energy well corresponds to the number of Pt atoms in the nanoparticle except for the pair of "tetrahedron and octahedron". The tetrahedron has a slightly deeper energy well compared with the octahedron although it has the least number of atoms. This might be attributed to the fact that more atoms are located closer to the minimum in the Lennard-Jones pairwise interaction potential in tetrahedral Pt compared with the octahedron. However, plots of the energy on per Pt atom basis show a much smaller difference between particles of varying shape but do not fall on a unique master curve because the distribution of distances of Pt atoms from the graphite surface is a function of the nanoparticle shape. The binding energy on a per Pt

atom basis are reported in **Table 5**. We observe that the binding energy on a per particle basis does not have an obvious relationship with the total number of atoms in each shape. Instead, it is related with the ratio of number of atom at the bottom portion to the upper portion. When a larger portion of atoms are located in the bottom layer, it has a stronger binding energy. Thus the tetrahedron, (the majority of whose atoms are located closer to the bottom) has the highest binding energy.

Figure 10 shows the binding energy and adhesion force between the PtO and oxidized graphite surface in the bare system as a function of separation between the nanoparticle and surface for several extents of oxidation of the graphite surface. The separation distance here is defined the same as that in the non-oxidized system, i.e. the distance between the center of carbon atoms forming the top layer of graphite and the center of Pt atoms located at the bottom of PtO nanoparticles to be consistent with the non-oxidized Pt/C systems. In this system, the potential energy is the sum of cumulative LJ and Coulombic interactions between all the atoms of the oxidized graphite and PtO. As shown in the figure, the potential energy and force curve in the oxidized Pt/C system follow the same trend as that of the non-oxidized Pt/C system. As a reference, the binding energy and adhesion force calculated between a PtO particle and the clean and bare graphite surface are respectively -2.96 aJ (1 aJ = 10^{-18}J) and -15.36 nN. Quantitative values of the binding energy and adhesion force for all other systems are shown in **Table 6** and **Table 7**.

There are two obvious features in **Figure 10**. First the position of the minimum is shifted to greater distances relative to the clean graphite surface, which is reasonable

given that there are now two layers of oxides between the Pt of the nanoparticle and the C of the graphite. Second, the depth of the energy wells is shallower for the oxidized materials relative to the clean graphite surface. Because electrostatic interactions are typically much stronger than dispersive interactions, the intuitive expectation is that the binding energy should be stronger in the presence of oxidized surfaces, at least in those cases where the exposed layers of charge on the nanoparticle and surface are of opposite sign. However, we do not observe this behavior. In the case of the epoxidized surface, the top atomic layer of the surface are epoxy oxygen atoms and the bottom atomic layer of the nanoparticle are oxygen atoms, both of which are negatively charged. Electrostatic repulsion resulting in weaker binding is to be expected. Moreover, as the degree of epoxidation on the surface increases, the binding energy continues to weaken. However, in the case of the hydroxylated surface, hydrogen atoms with positive partial charge are exposed. Still, we observe a reduction in binding energy, though we do observe that as the degree of hydroxylation on the surface increases, the binding energy does strengthen, as it should. Therefore, the initial reduction in binding energy must be due to a loss in dispersion energy resulting from the greater separation between nanoparticle and surface.

The trends in the adhesion force are of course related to those in the binding energy, but their manifestation still requires some explanation. The change in the position of the minimum of the force curves is a direct consequence of the change in the position of the minimum in the energy due to the presence of the oxide layers. The adhesion forces are all weaker for the oxidized systems relative to the clean system, as were the binding energies. However, the trend in the adhesion force with respect to

oxidation is different than that observed for binding energies. For the hydroxylated surfaces, both binding energy and adhesion force increase in magnitude with increasing degree of hydroxylation. In contrast, for the epoxidized surfaces, the binding energy decreases while the adhesion force increases in magnitude with increasing degree of epoxidation. The explanation for this apparent discrepancy can be found in the long-range repulsion between the epoxidized surfaces and the oxidized nanoparticle. There the binding energy actually becomes positive before decaying to zero at large separation from the positive side. This long-range electrostatic repulsion results in a maximum in the potential energy curve. This feature is absent in the clean graphite and hydroxylated graphite systems which are attractive at large separations.

Wet Systems

In this section, we discuss the results of catalyst nanoparticle adhesion on wet systems. These systems contain a film of Nafion on the graphite surface at various hydration levels. This recast Nafion serves as a path for proton transport from the catalyst nanoparticle to the proton exchange membrane. It also acts as a binder for the nanoparticles. Sufficient Nafion is placed to form a uniform film of 1 nm thickness. However, none of the simulation snapshots reveal a uniform film, since the hydrated Nafion aggregates into clusters and does not remain distributed on the hydrophobic clean graphite surface. Furthermore, nominal water contents of λ = 3, 6, 9 and 15 H_2O/HSO_3 are investigated. Previous simulations of hydrated Nafion at the membrane/vapor interface or at the membrane/catalyst/vapor and membrane/graphite/vapor three-phase interfaces show that virtually all of the water is retained in the membrane for λ = 3

through 21 H_2O/HSO_3, with roughly only one molecule or less entering the vapor phase at any instant in time[68,118]. In this work, we use the nominal water contents, but it is observed that much of the water leaves the film and enters the vapor phase. This is consistent with experimental observations that the ability for Nafion to retain moisture decreases as the membrane thickness decreases[137]. It should be pointed out here that the evaporation of water molecules into the vapor phase does not affect the relationship between the λ value and hydration level, i.e., it is still true that a higher λ value represents a higher hydration level. We have verified this by calculating the average number of water molecules retained in the Nafion film (indicated by 'effective λ' value) for the 2 nm cubic Pt systems and all the oxidized Pt/C systems of different λ values. Results are presented in **Table 8**. In the oxidized Pt/C system, the amount of water retained in the film depends on the type and degree of oxidation on the surface, however, the relationship between the λ value and hydration level is still true, i.e. higher λ value represents a higher hydration level.

Calculation of the binding energy and adhesion forces from the wet simulations involves two components. The first is the energy and force between the rigid carbon support surface and the rigid catalyst nanoparticle. These energies and forces vary smoothly with separation as shown in **Figures 8, 9 and 10**. (This is the only contribution present in the dry systems.) The wet systems have a second contribution to the binding energy and adhesion forces, which are due to the interaction between the catalyst nanoparticle and the dynamic molecules in the system, including the Nafion, water molecules and hydronium ions. If these particles remained as a film, their contribution to

the binding energy and adhesion force would remain unambiguous. Since some of the water enter the vapor phase, the reported binding energy will of necessity include some energy from water adhered to the catalyst surface. It is worth pointing out here that compared to the dry system, the wet system exposed interesting phenomena such as polymer bridging etc., which makes the calculation of potential and force more complicated and difficult to estimate by simple back-of-the-envelope calculations.

- **Effect of Nafion at different humidity levels on catalyst adhesion**

Figure 11 shows the potential energy versus separation distance curve for systems containing a cubic Pt particle of 2 nm with varying water content. In **Figure 11**, it is clear that when Nafion and water are introduced to the system, the binding energy becomes stronger. Another immediately apparent feature of **Figure 11** is that the curves now contain fluctuations. On the smallest time scale (on the order of femtoseconds), these fluctuations are due to the dynamics of the mobile components (Nafion, H_2O and H_3O^+). At larger timescales (on the order of tens of picoseconds) these fluctuations are due to dynamics of relaxation processes of polymers in the system. Thus we observe non-monotonic trends in the binding energy as a function of separation. The molecular-level origin of this behavior will be discussed shortly.

In **Figure 12 (a)-(f)**, a series of snapshots describing the detachment of the 2 nm cubic Pt nanoparticle from the wet surface (λ=3) exposes the nature of this polymer relaxation. The nanoparticle is removed at a relatively high constant velocity. In this process, the polymer is both being stretched by the movement of the nanoparticle and is also undergoing internal relaxation both on the surface of the graphite and the surface of

the nanoparticle. As the separation increases, the polymer is further stretched until, in the case of **Figure 12**, it releases the nanoparticle and snaps back to the graphite surface.

In **Figure 13**, the force curves for the 2 nm cubic Pt systems are presented at different hydration levels. The degree of fluctuation in the forces is much greater than that in the binding energy, and is so large that it obscures the interpretation of the data. The origin of these fluctuations, large when compared to experiment, is due to the very high temporal resolution (sampling frequency) of the simulations, which is 1 ps. Because of this extraordinarily high temporal resolution, the curve captures fluctuations due to the short-time scale dynamics of the polymer film. It also provides an abundance of data, greater than 10^5 data points for any given simulation. Thus some filtering of the data is necessary in order to observe the dependence of the force on properties such as degree of hydration.

A filtered result of **Figure 13** is shown in **Figure 14**. Several filtering procedures were explored. A method is required preserves key features of the curves, such as the depth of the attractive well, but at the same time is capable of averaging out the temporal fluctuations. The filter used in this work is a combination of piecewise polynomial fitting and local averaging. The piecewise polynomial fitting is used at short lengths scales, less than 1 nm, to maintain the correct shape of the attractive well. Beyond 1 nm, local averaging is employed, which reduces the noise in a given spatial region, but also is capable of retaining distinct features due to observed molecular events. The local averaging was performed over a region of 1 nm and iteratively applied.

One can now study the binding energies of **Figure 11** and the filtered adhesion forces of **Figure 14** to understand the role of Nafion and water on nanoparticle adhesion. Compared to the bare system, Nafion at all water contents acts as a binding agent, increasing the magnitude of the binding energy and the adhesion force. The binding energy is increased by a factor of 4.31, 5.40, 4.63 and 4.61 for the λ = 3, 6, 9 and 15 respectively. The adhesion forces is increased by a factor of 1.40, 1.33, 1.26 and 1.32 for the λ = 3, 6, 9 and 15 respectively. However, it should be point out here for the second time that strengthening the metal-support interaction by introducing a thicker film is not encouraged because an excess of Nafion film in the catalyst layer will become a barrier for the reactant gas to access the reaction site and resulting in a malfunctioning fuel cell. It is worth noting that that at large separations, the energy does not return to zero because the Pt nanoparticle has dragged water (and in some cases Nafion) from the surface with it. The forces do return to zero at large distances because the distribution of the water around the Pt nanoparticle is uniform and does not exert a net force in the normal direction to the graphite plane (or any other direction for that matter).

Even at short distances, the dependence of the binding energy and adhesion force between the nanoparticle and the surface as a function of water content is nonlinear. As we can observe in the inset of **Figure 14**, the adhesion force decreases in magnitude from λ = 3, 6, and 9. In other words, in this range of water contents, the strength of adhesion weakens with increasing hydration. However, for the λ = 15 system, the maximum adhesion was slightly strengthened while it still does not exceed the maximum adhesion in λ= 3 system.

In an attempt to better understand the role that water plays in nanoparticle adhesion, it is important to separate out physical trends from statistical variation. In this work, only a single detachment event was performed for each combination of particle size, shape and water content. Therefore, our sampling is limited to a single event. As shown in **Figure 15**, the distribution of Nafion, water and hydronium ion around the Pt and graphite surface varies not only as a function of water content, but would also vary from one independent realization of the detachment event to another. Thus we report real, observed simulation results, which we believe to be typical and characteristic of each system. However, we also acknowledge that there is statistical variation that has not been quantified by this work. For example in some cases, the stretching of polymers as the Pt nanoparticle is removed from the graphite surface is observed (as shown in **Figure 12**) and in other cases, it is not observed. However, all phenomena reported here are observed in a sufficient number of different cases (a total number of 20 simulations were performed) for one to reliably accept that we did not observe a rare one-in-a-million event. For example, the phenomenon of polymer bridging is observed in many of these simulations.

With these cautionary disclaimers behind us, in **Figure 15**, we observe that as Nafion aggregated into non-uniform clusters on the graphite surface, part of the cluster maintained contact with the Pt nanoparticle at $\lambda = 3$, 6, and 9. However, at $\lambda = 15$ there is preferential adsorption of a water cluster around Pt surface, which excludes Nafion. This phenomenon was also observed previously for Pt nanoparticles embedded in a "bulk" Nafion membrane, where the water density increased near the Pt surface[111]. Therefore,

the most hydrated system has the least Nafion coverage on the Pt nanoparticle. Since Nafion is the major contributor to the increased adhesion in the system, it is understandable that when the Nafion-Pt interaction becomes weaker, the adhesion force becomes weaker. While this explanation has taken care of the question of why the more hydrated systems (λ = 6, 9 and 15) exhibit a weakened adhesion relative to λ = 3, it cannot explain the phenomena that the most hydrated system (λ = 15) has a slightly stronger adhesion when compared with the λ = 9 system.

Figure 16 provides a reasonable answer to this question, namely that the adhesion between Pt and graphite is not only related to the interaction between Pt and Nafion, it is also related to the adhesion between Nafion and the graphite surface. In **Figure 16(a)-(d)**, a snapshot at a large separation (30 nm) is shown for the 2 nm cubic nanoparticle at λ = 3, 6, 9 and 15 respectively. At λ = 3, all of the Nafion stays on the graphite surface. At λ = 6, some of the Nafion remains on the graphite surface but some is attached to the Pt nanoparticle. At λ = 9 and 15, most of the Nafion has detached from the graphite surface. That is the detachment of the Pt nanoparticle has led to the delamination of the Nafion film from the graphite surface. It just so happens in the individual realizations given here that only partial delamination occurs at λ = 15, allowing for bridges of polymer to remain, which serve to strengthen the adhesion force. No such bridges remain at this large separation in the simulations at λ = 6 and 9.

For the oxidized Pt/C system, the same data filtering procedure is applied to reduce the noise of the force curve. Due to the fact that the Nafion ionomer film has a possibility of totally delaminate from the epoxidized carbon surface when the degree of

oxidation is higher than 25% (more details will be given in task 2), the 50% epoxidized surface is not investigated for the nano-adhesion calculation. Thus, only 5 oxidized carbon surfaces i.e. 10%-50% hydroxylated surfaces and 10%-25% epoxidized surfaces are investigated. The corresponding potential and filtered force curves are shown in **Figure 17**. The clean graphite-clean 4 nm tetrahedron Pt system is also included as a reference. After examining the figures, it is observed that several primary features such as the strengthened binding energy and the curve fluctuation remain true after the introduction of wet film. However, there are several unique features that are only observed in the oxidized graphite systems. For example, we noted that at the largest separation distance (distance = 35 nm), none of the potential curves in the oxidized systems returns to zero. In the previous section, we have attributed this feature largely to the fact that there are Nafion polymers attached to the Pt nanoparticle at the end of simulation (see **Figure 16**). Nevertheless, in these oxidized systems, we did not observe any of Nafion polymer attached to the PtO at the end of simulation for all systems (see **Figure 18 (f)**). After further examination of the system, it is found that the non-zero potential at the end of the separation process is due to electrostatic interactions. (In the clean systems, the nanoparticle and graphite surface were uncharged.) By comparing the energy curves with the clean graphite-Pt system, one observes that the oxidation of Pt and carbon support has extended the interaction range between the nanoparticle and the carbon surface[121]. The deepening of the binding energy and extending of its range is a desirable characteristic for a film that is intended to function as a binder.

On unoxidized surfaces, a dependence of the binding energy and adhesion force on degree of hydration in the film was observed[121]. To investigate this effect, simulations were also performed at a higher water content of $\lambda = 9$. **Figure 19** plots the binding energy (a) and adhesion force (b) at hydration level of $\lambda = 9$ for the PtO nanoparticle on six surfaces. For the oxidized systems, the binding energy and adhesion force curve at $\lambda = 9$ are very similar to the $\lambda = 3$ system. All the adhesion forces in $\lambda = 9$ systems are enhanced compared with the corresponding system in $\lambda = 3$. However, from the binding energy point of view, epoxidized systems and hydroxylated systems show different trends. For the epoxidized system, the binding energy is enhanced for both oxidation levels (10% and 25%) with increasing hydration. However, for the hydroxylated system, the binding energy is enhanced by the addition of water at low oxidation extent (10%) and diminished at high oxidation extent (25% and 50%). An explanation for the complex behavior of the hydroxylated system is given below. Quantitative values of binding energy and adhesion force are also listed in **Table 6** and **Table 7**.

In the interest of generating a more finely resolved understanding of the role of hydration on nanoparticle adhesion, one surface, the 50% hydroxylated surface, was simulated at $\lambda = 3$, 6, 9 and 15. **Figure 20** plots the binding energy (a) and adhesion force (b) at hydration levels of $\lambda = 3$, 6, 9 and 15 for the PtO nanoparticle on the 50% hydroxylated surface. The bare surface with no hydrated film at all is also included for comparison. Relative to the bare surface, the magnitude of the binding energy is increased by a factor of 10.14, 10.63, 9.75 and 9.93 for the $\lambda = 3$, 6, 9 and 15 system respectively. Another feature apparent in **Figure 20** is that the introduction of mobile

components (Nafion, H_2O, and $H3O^+$) has shifted the equilibrium energy distance to the left, which is not observed in our previous non-oxidized graphite-Pt system. One also notices from **Figure 20 (a)** that the binding energy for the system first experiences a slight increase from $\lambda = 3$ to $\lambda = 6$ and then a decrease when the hydration level is higher than $\lambda = 6$. This is caused by the polymer conformation on the oxidized graphite surface: at low hydration levels ($\lambda = 3$ and 6), the polymer stays relatively flat and covers most space on the surface (see snapshots in **Figure 21 (a) and (b)**), which corresponds to the relatively stronger binding energy; while at high hydration levels, the polymer chains began to ball up (see snapshots in **Figure 21 (c) and (d)**) and resulted in a weaker connection with the hydroxylated graphite surface, which corresponds to the weakening in binding energy.

Figure 20(b) is the corresponding force curves of **Figure 20(a)**. It is observed that with increasing hydration level, the strength of adhesion is increased by a factor of 15.59, 16.47, 16.85 and 19.97 for $\lambda = 3$, 6, 9 and 15 respectively, which displays a monotonic relationship between the hydration level and the adhesion force. As observed in the non-oxidized graphite and Pt system, the magnitude of the adhesion force largely depends on two aspects: the interaction between the polymer binding agent (the Nafion film) with the carbon surface, and the interaction between the polymer binding agent with the nanoparticle. Since in this system, the interaction between the Nafion and the hydroxylated graphite surface is strong, and no polymer detachment from the oxidized graphite surface is observed at any hydration levels. The magnitude of the adhesion force largely depends on the interaction between the PtO and the Nafion polymer. After

examining the snapshot (see **Figure 22**), it is observed that the connection between PtO and the Nafion polymer is largely realized by the interaction between the sulfonic acid group on the Nafion side chain and the water molecules attached on the PtO surface. Therefore, the more water molecules attached to the PtO surface, the stronger the connection between PtO and Nafion chain will be. The number of water molecules hydrogen bound to the nanoparticle increases with degree of film hydration, from 2, 22, 31 to 73 respectively for the $\lambda = 3, 6, 9, 15$ systems.

- **Effect of catalyst nanoparticle shape on catalyst adhesion**

In this section, we investigate the effect of nanoparticle shape at two hydration levels, $\lambda = 3$ and $\lambda = 15$. It is true that different nanoparticle shapes expose different faces of the catalyst (Pt) crystal. It is likely that the guiding principle in terms of nanoparticle shape should be the choice of face that yields the highest electrochemical activity. Nevertheless, it remains important for nanoparticles of any shape to adhere to the surface. Additionally, due to the limit of lack of reliable oxidized Pt models, the catalyst shape in the oxidized system is not investigated.

In **Figure 23**, the adhesion force for four nanoparticle shapes is presented at $\lambda = 3$. For comparison purposes, the adhesion curves from the bare system are also included. From **Figure 23**, it is observed that the maximum adhesion is enhanced with the introduction of the wet film for all particle shapes. While all the other shapes are able to reach equilibrium at around the same position in the bare and wet systems, the tetrahedral Pt has shifted its equilibrium distance from 0.32 nm to 0.39 nm (see **Table 9**). After examining a snapshot for the tetrahedron at 3.9 nm, it is noticed that a layer of Nafion has

slipped between the Pt nanoparticle and the graphite surface, which is the cause of the equilibrium distance shift.

It is also interesting to observe the effect of nanoparticle shape on the ability to form polymer bridges, since it is at least partially through these bridges that the film fulfills its role as a binder. We intuitively expect the nanoparticle shapes with more Pt atoms to more strongly adhere to the polymer and encourage the formation and retention of bridges. In **Figure 24 (a)-(d)**, snapshots of the systems with the nanoparticle (cube, tetrahedron, truncated octahedron and octahedron respectively) at a separation distance = 7.5 nm are shown. In **Figure 25 (a)-(d)**, snapshots of the systems with the nanoparticle (cube, tetrahedron, truncated octahedron and octahedron respectively) at a separation distance = 12.0 nm are shown. From **Figure 24**, we can see that polymer bridges have formed in systems with three shapes of nanoparticles, all but the octahedron. In **Figure 25**, we observe that the polymer bridge has disappeared from the truncated octahedron at a separation of 12 nm. Thus we partially observe our expected trend. The particles with the most Pt atoms, the cube **(24 (a))** and the truncated octahedron **(24 (c))**, maintain bridges at 7.5 nm and the particle with the most Pt atoms, the cube (**25 (a)**), maintains polymer bridges at 12 nm. However, contrary to the simple rule that polymer binding to the Pt nanoparticle should be a function of number of Pt atoms in the nanoparticle; it is observed that the nanoparticle with the fewest Pt atoms, the tetrahedron, also maintains bridges through 12 nm. Apparently there is something to the tetrahedral shape that allows stronger adhesion to the polymer.

Figure 26 provides a close-up of the cubic and tetrahedral Pt nanoparticles at a separation of 12 nm, in order to better observe the polymer conformation on the Pt surface. As shown in **Figure 26 (a)**, the interaction between the cubic nanoparticle and Nafion is achieved through a tiny part of Nafion chain (mostly carbon) at the bottom of the cube (the majority of the polymer that were on the surface at distance = 7.5 nm have detached from the catalyst as the distance increased). In **Figure 26 (b),** the interaction between the tetrahedral nanoparticle and Nafion is achieved through several sulfonic acid groups attached both on the bottom and side of catalyst surface, interacting with water and hydronium ions. Obviously, the interaction involves both Coulombic attraction (interaction between hydronium ion and sulfonic acid groups) and LJ attraction will be stronger than LJ attraction alone. Thus the hydrated tetrahedral system has a long-range effect due to its unique 'anchor-like' structure, i.e. its base area is much larger compared to the upper point, which allows the Pt particles to act like an anchor and more securely bind polymers during the detachment process.

Having observed the impact of nanoparticle shape on nanoparticle adhesion at a relatively low nominal water content of λ=3, we now turn our attention to a higher water content of λ=15 in order to determine if the observations are independent of water content. **Figure 27** shows the filtered force results for the wettest systems (λ=15) studied here. Most of the results are consistent with the finding obtained at the low hydration level (λ=3). For example, the adhesion is enhanced by the introduction of the hydrated polymer film into the system, relative to the bare system. Moreover, was seen with nanoparticle size, as the hydration level goes up, more polymer will be brought away

during detachment, which results in more fluctuations in the binding energy and adhesion force as a function of separation. However, we do not observe anomalous behavior for the tetrahedral nanoparticle as was observed at the lower water content.

In **Figure 28 (a)** and **(b)** top and side views of a snapshot for the 2 nm tetrahedral nanoparticle at λ=15 are shown before the detachment process starts (after the system is fully equilibrated). As was the case for the cubic nanoparticle in **Figure 15**, at high water contents the tetrahedral nanoparticle is surrounded by water and is isolated from Nafion. Thus, it is not surprising that we do not see the bridging effect between Nafion/Pt and Nafion/graphite. In fact, as shown in **Figure 28 (c)**, there is no polymer bridging with the tetrahedral particle at high water contents even at the very small separation distance of 1.5 nm. Without this polymer bridging, the tetrahedral particle detaches relatively easily from the surface.

- **Effect of nanoparticle size on catalyst adhesion**

In this section, we investigate the effect of nanoparticle size at two hydration levels, $\lambda = 3$ and $\lambda = 15$. It is true that different nanoparticle size changes the ratio of catalyst surface area to catalyst volume and thus impacts the amount of catalyst that must be present in the system. Again, it is likely that the guiding principle in terms of nanoparticle size should be optimizing electrochemical activity. However, in this section, we show that adhesion is a function of nanoparticle size and thus may be considered as a factor in selecting catalyst nanoparticle sizes for optimal performance. Due to the same reason, i.e. lack of reliable molecular model on the oxidized Pt nanoparticle, the effect of nanoparticle size is only investigated for non-oxidized Pt/C systems.

Figure 29 and **Figure 30** show the size effect of Pt nanoparticle on adhesion force at two different water contents, $\lambda = 3$ and $\lambda = 15$. We noticed that for both hydration levels, the adhesion is a function of Pt size. As the nanoparticle size goes up, the adhesion force gets stronger, at both hydration levels. At $\lambda = 3$, the adhesion force is increased in magnitude by a factor of 1.40, 1.24, and 1.14 for the 2 nm, 4 nm and 6 nm nanoparticles respectively. At $\lambda = 15$, the adhesion force is increased in magnitude by a factor of 1.40, 1.43, and 1.31 for the 2 nm, 4 nm and 6 nm nanoparticles respectively.

- **Effect of oxidation of the Pt/C surface on the catalyst adhesion**

In this section, the effect of surface oxidation of the carbon surface is investigated. Two different functional groups are introduced to the graphite surface and the binding energy and adhesion force is calculated and compared with that of the non-oxidized Pt/C systems. The catalyst nanoparticle in this section in modeled as PtO.

It is observed in **Figure 17** that the binding energy is more favorable with the hydroxylated surface and becomes even more favorable as the degree of hydroxylation increases. Thus is demonstrated the idea that the intentional introduction of a specific surface functional group such as the hydroxyl group on the carbon surface can enhance adhesion between nano-particles and graphite, which may improve the practical performance of the Pt/C catalyst in a fuel cell device. Recently, a solution sonochemical oxidation method was used to introduce surface functional groups containing –C-OH, -C=O, -C-O-C- etc. on carbon nanotubes (CNT), where Pt nanoparticles were deposited, leading to enhanced electro-catalytic activity in the oxygen reduction reaction in fuel cells relative to unmodified CNTs[37].

Figure 17(b) provides the corresponding force curve for the λ = 3 systems discussed earlier. It is shown in the figure that the adhesion force for both epoxidized and hydroxylated system increases with the oxidation extent. Quantitative values for adhesion forces at λ = 3 are listed in **Table 7**. One feature worth noting in **Figure 17(b)** is that unlike the hydroxyl systems, the epoxy systems exhibit a repulsive force after the PtO is detached from the surface. This repulsive force indicates that the PtO nanoparticle experiences an electrostatic barrier to adhesion to the surface.

Conclusions of Task 1

The purpose of task 1 was to study the catalyst nanoparticle detachment mechanism from the nano-adhesion point of view. Molecular dynamics simulations were performed on various systems containing non-oxidized catalyst nanoparticles of different sizes, shapes and Nafion thin film at four hydration levels of λ = 3, 6, 9 and 15 to investigate that how the catalyst size, shape and its surrounding environment will affect the adhesion. Additionally, the effects of oxidation state of both the catalyst and carbon support surface is also investigated on the nanoparticle adhesion.

For the non-oxidized systems, we found that bigger nanoparticles yield better adhesion regardless of the humidity level. Additionally, nanoparticle shape of tetrahedron has a significant influence on nanoparticle adhesion. It acts like an anchor while detaching from the surface, which decreases its possibility of detaching from the surface and allows it to keep connected with its support through the bridged polymers. However, no significant effect on the nanoparticle adhesion was observed for all the other shapes (cube, octahedron and truncated octahedron). The slightly difference in adhesion

force for these three shapes are due to the atom quantity difference in each shape. As for the effects of Nafion film, it acts like a binder to keep Pt nanoparticles in place. The hydrophobic backbone will interact with the carbon support and the hydrophilic side chain can interact well with the Pt surface as well as the water molecules and hydronium ions that are attached on it. The hydration level has a rather complicated effect on adhesion: at low hydration levels, due to the fact that water molecules will accumulate in the vicinity of the Pt nanoparticle, Nafion polymer will be excluded causing a reduction of polymer-Pt interaction, and as a result of which, the adhesion force will decrease as the hydration level goes up. Furthermore, the extent of the decrease will be affected by the interaction between graphite surface and Nafion as well. When the humidity level increases beyond a certain point, polymer delamination occurs, the extent of delamination can influence the strength of interaction between Nafion and graphite. Nafion chains are more flexible at high humidity levels and there is a better chance for the hydrophobic backbone to transform to a more favorable configuration on the graphite surface, thus only partial delamination may occur. Partial delamination allows polymer chains to form bridges between graphite surface and Pt nanoparticle, which can enhance the adhesion force. The adhesion between the Pt catalyst and its support can be strengthened by controlling the nanoparticle size and shape as well as controlling the Nafion content and its humidity level in catalyst layer.

To investigate the impact of oxidation on nanoparticle adhesion for Pt/C catalysts in PEMFC catalyst layers, molecular dynamics simulations were performed on various systems containing PtO nanoparticles and two different kinds of oxidized graphite

surfaces (epoxidized and hydroxylated graphite) at different oxidation extents with the presence of Nafion thin film at four hydration levels of $\lambda = 3$, 6, 9, and 15. For the bare system (without a polymer film) adhesion between the PtO nanoparticle interacts more weakly than the Pt nanoparticles on unoxidized graphite. With the epoxidation of the graphite surface, the adhesion of PtO weakens further due to the electrostatic repulsion between the exposed oxygen atoms. However, with the hydroxylation of the graphite surface, the adhesion of PtO strengthens due to the electrostatic attraction between hydrogen on the surface and the oxygen on the nanoparticle.

The presence of the Nafion film acts like a binding agent, enhancing the binding energy and adhesion force between PtO and the hydroxylated surfaces. As the degree of hydroxylation increases, the adhesion force increases. The effect of hydration on the hydroxylated system depends on the degree of hydroxylation, i.e., at low oxidation extent (10%), a slight increase in the magnitude of binding energy is captured from $\lambda = 3$ to $\lambda = 9$; at higher oxidation extents (25% and 50%), the magnitude of the binding energy show a decrease from $\lambda = 3$ to $\lambda = 9$, which can be traced to changes in polymer conformation on the hydroxylated graphite due to the presence of varying amounts of water.

The impact of a Nafion film on an epoxidized surface is very different than that on the hydroxylated surface. At low levels of epoxidation, the adhesion is enhanced; however, at higher levels of epoxidation, where the film either partially or fully delaminates, there is no benefit to adhesion. The effect of hydration on the epoxidized system is to enhance binding with increased water content.

The extent and type of oxidation on a carbon support surface has a strong impact on the adhesion of the catalytic nanoparticles. We observe that it is possible to strengthen the adhesion of the film and catalyst nanoparticle to the surface by controlling the type and extent of oxidation as well as the humidity level in the catalyst layer of the PEMFC. This understanding provides a new perspective toward developing a more durable catalyst layer as well as for accounting for environmental conditions resulting in loss of electrochemical surface area.

Task 2 Microstructure and Properties of the Ionomer Film

In this task we discuss the microstructure and properties of the ionomer film of the catalyst layer. The results and discussion are organized into two parts. In the first part, a set of molecular dynamics (MD) simulations composed of an oxidized nanoparticle (4 nm PtO), various oxidized carbon substrates and a polymer binder at various degrees of hydration were conducted to study the effect of oxidation on the adhesion of the polymer film. The variables investigated in these simulations include the type (hydroxyl or epoxy) and extent of oxidation (10%-50% for hydroxyl and 10-25% for epoxy), the presence of polymer electrolyte binding film and extent of hydration. In this analysis, the binding between the polymer film and the carbon surface is most clearly revealed. In the second part, the nanoscale configuration of the hydrated Nafion film is investigated as a function of four variables: (1) film thickness, (2) surface oxidation, (3) presence of catalyst and (4) hydration level.

Part 1. Effect of Surface Oxidation on the Ionomer Film Conformation

Figure 31 show the equilibrium binding energy between the hydrated Nafion membrane and the oxidized rigid system (oxidized graphite and PtO) at different oxidation levels of graphite. From **Figure 31**, it is clear that some oxidation on the carbon surface (oxidation extent = 10%) enhances the strength of binding between the hydrated membrane and the substrate for both epoxidized and hydroxylated surfaces at both hydration levels. In other words, slight oxidation is beneficial for the stability of the interface of PEMFC catalyst layers from the binding energy point of view. However, after the oxidation extent exceeds 10%, the epoxidized and hydroxylated systems show different trends. For the epoxidized system, the magnitude of the binding energy begins to decrease with the increase of oxidation extent, which describes weaker binding between polymer film and graphite surface. In contrast, the hydroxylated system shows a plateau in binding energy after 10% oxidation. Therefore, from the binding energy point of view the hydroxylated graphite surface actually helps the hydrated membrane to fulfill its role as a binding agent. Snapshots showing the polymer conformation at $\lambda = 3$ for both epoxidized and hydroxylated graphite surface at oxidation rates of 10% and 50% are shown in **Figure 32 (a)-(d)** to further illustrate the point. Figure **32 (a)** and **(b)** represents the 10% and 50% the epoxidized system respectively. These pictures confirm the results in **Figure 31**. At the epoxidation extent of 50%, the binding energy is sufficiently weak that the film delaminates from the oxidized graphite surface. The only point of contact between the polymer and the surface is through the PtO nanoparticle. In contrast, from

Figure 32 (c) and **(d)**, the polymer film adheres to the hydroxylated graphite surface at both extents of oxidation.

The observations in **Figures 31** and **32** are quite surprising. Bare graphite is a hydrophobic material. Oxidation of the surface introduces polar groups, which intuitively should serve to more strongly bind, a polar molecule like Nafion, which has a sulfonate ion (q = -1 e) at the end of every side chain. This intuitive behavior is observed for the hydroxylated surface, although the effect seems to reach a plateau. However, for the epoxidized surface, the intuitive behavior is only observed at low oxidation levels. Further oxidation makes the surface even less favorable than the bare (completely unoxidized) graphite surface.

The different behavior of the polymer film on the surface of epoxidized and hydroxylated graphite can be explained by the different distribution of charge at the two surfaces. In the case of hydroxylation, the top most atomic layer of the graphite presents a positive charge (the partial charge of the hydrogen atom). However, in the case of epoxidation the top most atomic layer of the surface presents a negative charge (the partial charge of the oxygen). Thus the simulation introduces a fixed charge distribution in the oxidized graphite that results in a reorientation of the dynamic molecules in the film. The effects of this charge distribution are shown in **Figure 33**, which presents the charge distribution normal to the surface starting from the top layer of graphite (located at a position of 2.037 nm). The charge shown in the vertical axis is all the atoms located on that specific layer. **Figure 33 (a)** presents the charge distribution for a 50% hydroxylated graphite surface at different humidity levels. From the figure, it is noticed that after the

black line (representing total charge for the layer of hydrogen atoms in the hydroxyl group), there is a slightly positive charge peak (from a minority of hydrogen of adsorbed water), a negative peak (from oxygen of adsorbed water) and a positive peak (from the majority of hydrogen of adsorbed water). After a careful examine of the orientations of H_2O and H_3O^+ on the oxidized graphite surface, it is found that the water molecules prefer the orientation with the oxygen atoms in direct contact with the oxidized graphite surface and the two hydrogen atoms facing the vapor phase. This is an intuitive orientation since it allows the oxygen of water to hydrogen-bond with the hydrogen of the hydroxyl group. An illustrative snapshot is included in **Figure 33 (a1)**. A similar orientation is observed for hydronium ions in this layer with two of the three hydrogen atoms arranged away from the surface as illustrated in the second snapshot in **Figure 33 (a2)**. The unique orientation of both water and hydronium ions on the hydroxyl surface is caused by the positively charged hydroxyl atoms on top of the graphite surface. Therefore, Coulombic attraction results in the most stable orientation of water and hydronium ions with hydrogens facing the vapor phase. The positively charged hydrogen in both water and hydronium ions attract the sulfonic acid groups in the Nafion side chain, as a result of which, the polymer is strongly anchored on the hydroxylated graphite surface, which explains why the Nafion membrane remained adhered to this surface.

The same mechanism can be applied to explain the behavior on the epoxidized surface as well. At low oxidation rate, the graphite surface is not fully covered by the oxygen atoms from the epoxy group, which leaves some of the carbon atoms in the epoxidized graphite exposed to the water and hydronium ions. Since the epoxidized

carbon atoms are positively charged, water and hydronium ions simultaneously orient with the oxygen atoms in direct connect with the carbon atoms on the graphite surface, leaving their hydrogen atoms facing the vapor phase (**Figure 33 (b1)**), which become the anchor site for the side chain of the Nafion membrane. However, at higher extents of oxidation, the surface is dominated by the negatively charged oxygen atoms in the epoxy group, which tend to orient the water and hydronium ions with hydrogen atoms in direct contact with the oxidized graphite surface, leaving the negatively charged oxygen atoms from water and hydronium ions facing the vapor phase. See snapshots in **Figure 33 (b2) and (b3)**. The backbone of the Nafion membrane is hydrophobic and only weakly interacts with water. The significant interaction between Nafion and the aqueous layer is therefore through the sulfonate anions located on the end of each side chain. The negatively charged sulfonate groups repel the exposed negatively charged oxygen of the water molecules hydrogen-bound to the epoxy groups. In extreme conditions, this electrostatic repulsion results in delamination of the film.

In **Figure 33 (c)**, the charge distribution is reported at a low water content ($\lambda = 3$) for surfaces with various extents of epoxidation and hydroxylation. In general, we observe a damped oscillatory charge distribution extending out to 5 nm. Interestingly, much of the long-range structure of the charge distribution is the same for both extents and types of oxidation. The charge distribution in the first couple peaks, however, does depend on type and extent of oxidation. For example, at lower extents of hydroxylation, we observe a negative charge peak at 2.4 nm, whereas at the higher extent, we observe a positive charge peak. This is because at lower extents, water molecules are able to

approach hydroxyl groups from the side and form favorable interactions with the oxygen atom of the hydroxyl group.

In **Figure 33 (d)**, the charge distribution is reported at a higher water content (λ = 9) for surfaces with various extents of epoxidation and hydroxylation. Comparison of **Figures 33 (c)** and **(d)** shows that the increase in degree of hydration enhances the charge distribution effect in general. We do observe at high water content that the charge distribution is more pronounced in the 25% than the 50% epoxidized surface, opposite of the trend observed at low water content. The mechanism behind this can be understood by considering that, as more water and hydronium ions are introduced to the system, and multiple layers of water and hydronium ions are present on the surface, the water layer begins to show more bulk-like water properties, including a more random orientation of water[138] and thus the charge effect is less obvious for the 50% case. This trend is more obvious for the epoxidized surface than for the hydroxylated surface because the water retention ability of the epoxidized surface is greater. That the epoxidized surfaces retain more water is confirmed in **Table 8**, where the actual water content in the film (effective λ value) is listed. The effective λ value is higher for the epoxy system at the same oxidation extent.

Part 2. Nano-Characterization of the Nafion Ionomer Thin Film

In this part, nanoscale morphology of the hydrated ionomer film resting on the carbon support is investigated. The characterization of the Nafion thin film is done through presenting results of RDFs, coordination numbers, snapshots, film effective λ

values and surface areas. A complete description of the nanostructure of the ionomer film is created through the careful integration of these various pieces of information.

The logical organization of this part of simulations is readily apparent in **Table 10**. The effects of hydration, film thickness and surface oxidation on film morphology are investigated for systems with no catalyst (1st simulation group), comprising runs 1 through 12. Unoxidized systems containing a Pt nanoparticle (2nd simulation group) comprise the next four runs. Oxidized systems containing a PtO nanoparticle (3rd simulation group) comprise the final eight runs.

The RDFs describes the distribution of the density of a particular species as a function of distance from a reference particle[139]. In this work, five RDFs are calculated to describe the hydrophilic domain in the Nafion film, including the sulfonate-sulfonate (S of SO_3^-/S of SO_3^-), sulfonate-water, (S of SO_3^-/O of H_2O), sulfonate-hydronium ion (S of SO_3^-/O of H_3O^+), hydronium ion-water (O of H_3O^+/O of H_2O) and water-water (O of H_2O/O of H_2O) RDFs. We note that in **Figures 34** through **48**, all five RDFs for all twenty-four simulations are presented in a complete and methodical manner, organization are listed in **Table 11**. In this document, selected RDFs are presented and discussed. Note, we choose to present RDFs with units of density rather than the normalized (dimensionless) pair correlation functions (PCF), because the systems are inhomogeneous and the normalization constant that would relate the RDF to the PCF is poorly defined and varies from one system to the next.

A quantitative measure of the number of molecules of a given species within the first shell can be obtained by integrating the RDF over the first peak. This provides a

"coordination number" between pairs of species. The upper limit of integration is defined by the position of the first minimum following the first peak. This minimum is located at 6.9 Å for the sulfonate-sulfonate RDF, 6.0 Å for the sulfonate-water RDF, 5.5 Å for the sulfonate-hydronium ion RDF, 4.2 Å for the hydronium ion-water RDF and 5.1 Å for the water-water RDF. Coordination numbers for these five pairs for all twenty-four simulations are reported in the last five columns of **Table 10**.

❖ **Catalyst-Free Surfaces**

The first simulation group contains a total of 12 simulations. A full simulation matrix for three types of graphite surfaces (pristine, epoxidized, hydroxylated), two hydration levels and two film thicknesses are performed in this group of simulations.

In a bulk membrane, the hydration level of a membrane is well-defined, λ is the number of H_2O per HSO_3 (most of which have dissociated into SO_3^- and H_3O^+). In a film, which is in equilibrium with a gas phase, some water will leave the film in order to form an equilibrated vapor phase. The concept of an effective hydration level for a film, λ_{eff}, is introduced based on the fact that the ability for Nafion to retain moisture decreases as the membrane thickness decreases[137]. The same phenomena has been observed in our previous simulations[121,140]. The value of λ reported in **Table 10** gives the number of H_2O per HSO_3 in the simulation volume. The value of λ_{eff} reported in **Table 10** gives the number of H_2O per HSO_3 in the ionomer film, which does not include those water molecules that have entered the vapor phase. It is clear in **Table 10** that λ_{eff} is always smaller than the nominal λ and that any increase in λ corresponds to an increase in λ_{eff} when all other variables are held constant.

Before we engage in a quantitative analysis of the RDFs and coordination numbers, it can be useful to visually inspect snapshots that show a concrete realization of the conclusions deduced below. Two typical snapshots are shown in **Figure 49 (a)-(f)** to illustrate the morphology change of the hydrated Nafion film with respect to the humidity level change. These snapshots correspond to a 2 nm Nafion film on a 25% epoxidized graphite surface at hydration levels of $\lambda = 3$ **Figure 49 (a)-(c)** and $\lambda = 9$ **Figure 49 (d)–(f).** For each hydration level there is a top view of the film, a side view of the film, and a side view of the aqueous domain. The vapor phase water molecules and the carbon surface are omitted for a clearer view. The films were initially uniformly distributed over the carbon surface. During equilibration, the films underwent a relaxation that results in the inhomogeneous distribution over the carbon surface. The distribution is irregular in both the directions parallel to the surface as well as the direction normal to the surface. A noticeable increase in the water cluster size is observed from $\lambda = 3$ to $\lambda = 9$.

In bulk Nafion membranes, the aqueous domains contain water, the sulfonate groups and the hydronium ions. At low hydration levels, the aqueous clusters are small and poorly connected. In these small aqueous clusters, the sulfonate groups are more isolated from each other and the hydronium ions are tightly bound to the sulfonate anions[66]. As the hydration level increases, the aqueous clusters grow in size and become better connected. This change in nanostructure of the aqueous domain is reflected in all five of these RDFs. Larger water clusters allow (1) increased aggregation of the sulfonate groups, (2) increased hydration of the sulfonate group by water molecules, (3) decreased association between the sulfonate group and the hydronium ion as the

hydronium ion is able to explore more space in the aqueous domain, (4) increased hydration of the hydronium ion by water, and (5) increased water-water association[66]. In the first twelve simulations (all of which have no catalyst), there are six pairs of simulations in which nothing is changed but the water content. In all six cases, through an examination of **Table 10**, we observe that all five of these trends are obeyed. As the hydration level is increased, we observe (1) an increase in the sulfonate-sulfonate coordination number, (2) an increase in the sulfonate-water coordination number, (3) a decrease in the sulfonate-hydronium ion coordination number, (4) an increase in the hydronium ion-water coordination number and (5) an increase in the water-water coordination number. Thus all the expectations for the effect of hydration level on the nanostructure of the Nafion thin film based on the behavior of the bulk membrane are met. In addition to the coordination numbers presented in **Table 10**, the effect of hydration level can also be observed directly in the RDFs, of which the sulfonate-sulfonate is presented in **Figure 34** and all five RDFs are presented in **Figures 34** through **38**.

We begin the analysis of the effect of film thickness on film morphology with a comparison of snapshots in **Figure 50 (a)** and **(b)**. These snapshots correspond to a pristine (unoxidized) graphite surface at $\lambda = 9$ for a film thickness of 1 nm **(a)** and 2 nm **(b)**. The vapor phase water molecules are omitted for a clearer view. It can be seen that proportionally more water molecules are retained in the thicker film, which is both visible to the eye and reflected from the film effective λ values (**Table 10**), i.e. the film effective λ increases from 3.8 (1 nm) to 7.8 (2 nm) for the pristine graphite system at the hydration

level of $\lambda = 9$. Thus, one of the major effects of the film thickness on the morphology of the hydrated film is an enhanced ability to retain moisture with increasing film thickness, which is consistent with the experimental results[137].

Additionally, a thicker film has more contact points on the carbon support and is less prone to ball up as shown in **Figure 50.** In **Figure 50 (c)** and **(d)**, the film thickness difference in the 1 nm film and 2 nm film for the pristine graphite surface at the hydration level of $\lambda = 9$ are presented. The yellow dashed lines, separated by a distance of ~2.6 nm, are put there as the benchmark for the film thickness, which surprisingly indicate that the nominal 1 nm and 2 nm film do not have much difference in thickness. The result is not predicted since the 2 nm film is made by overlapping two 1 nm films, thus the 2 nm film would be exactly twice as thick as the 1 nm film, if the ionomer film kept their original contact points with the carbon support during the simulation. The explanation lies in the fact that what we describe as film thickness is actually the extent of ionomer film coverage on the surface. Nominal thickness refer to the ionomer film uniformly spread over the graphite surface; it is apparent that a certain degree of film ball-up occurred in both films regarding the fact that the carbon support in both cases is not 100% covered by the ionomer film (see **Figure 50 (a) and (b)**), although the ionomer film is initially evenly spread over the carbon surface. The inhomogeneous distribution of the ionomer film around the carbon support was also reported experimentally and was identified as one of the major reasons for the poor transport of protons as well as the low utilization of catalyst nanoparticles[45]. In the thinner film (1 nm), the phenomena of film balling up is more severe, which diminishes a large number of contact points between the ionomer

film and the carbon support. Thus a thicker film (more contact points) is desirable for achieving a better path for proton transport from the catalyst to the PEM, although too thick a film will bury the catalyst nanoparticles, presenting a mass transfer barrier to the vapor phase fuel.

To quantify the ionomer distribution, we have reported a film surface area in **Table 10**. This surface area is based on the use of a zero-volume probe to measure the exposed surface area of the atoms in the hydrated film, including Nafion, hydronium ions and those waters that remained in the film. For a perfectly laminar film, doubling the thickness would have a negligible effect on the surface area, since the area of the top and bottom of the film would not have changed. In these cases, some balling up of the film always occurs and an increase in film thickness results in a drastic increase in film surface area. In five of the six pairs of simulations in which nothing is changed but the film thickness, doubling the film thickness results in greater than a doubling of the film surface area. In the sixth pair (the hydroxylated surface at $\lambda = 3$), the surface area of the thicker film is almost doubled.

The observations from the snapshots, namely that with increasing film thickness we should observe better water retention and less balling-up, impact the RDFs in opposite ways. Greater water retention argues for larger aqueous clusters, but a flatter film argues for smaller, better distributed water clusters. The RDFs and the coordination numbers reflect these competing trends. For all six comparable pairs of simulations, the sulfonate-sulfonate coordination numbers are lower and the sulfonate-hydronium ion coordination numbers are greater with increasing film thickness, consistent with better distributed

water channels. However, for all six comparable pairs of simulations, there is better hydration of both the sulfonate and hydronium ions by water and increased water-water association, consistent with more water retained in the film.

To sum up this section, there are three major features for the effect of thickness on the morphology of the Nafion film: First, the ability to retain water is noticeably enhanced for the thicker film. Second, films of nominal 1 nm and 2 nm uniform thickness ball-up and expose portions of the support surface, with the fraction of exposed surface decreasing with increasing amount of ionomer. Third, the film thickness influences the morphology of the aqueous domain through which proton transport occurs.

It is well known that both the graphite surface and the catalyst undergo oxidation during operation[19]. The effect of oxidation is usually considered as a drawback that reduces fuel cell durability. However, suggestions are also available in the literature which indicates that appropriate surface oxygen groups can enhance the performance of the Pt/C catalysts[27,32,33,35]. Most of the available papers focus on discussing the effect of surface oxidation on the Pt/C degradation. There remains a lack of published work discussing the effect of oxidation on the Nafion film morphology, which is the subject of this section. There are three carbon support surfaces discussed in this section, the pristine graphite surface, a graphite surface with 25% epoxidation and a graphite surface with 25% hydroxylation. The key difference between these surfaces lies in the charge distribution on the surface. The pristine graphite surface presents no significant charge (at least relative to the other two cases). The epoxidized surface presents the oxygen, which contains a negative partial charge. The hydroxylated surface presents the

positively charged hydrogen atoms of the –OH groups. As has been shown previously, this charge distribution has a dramatic impact on film adhesion[140]. Small amounts of epoxidation and hydroxylation enhance adhesion. Large extents of epoxidation actually result in delamination, whereas large extents of hydroxylation continue to promote adhesion of Nafion. Based on **Figure 31**, we expect the 25% hydroxylated surface to enhance adhesion relative to the pristine surface and 25% epoxidized surface to impact structure but not to strongly impact the overall energy of adhesion. In our simulations, we have occasionally observed delamination for the 1 nm film on 25% epoxidized graphite surface (**Figure 51**) but never for the 2 nm film. This is consistent with our finding in the previous section that a thicker film experiences less balling-up and therefore has an enhanced tendency to remain laminated to the carbon support.

In the previous section (part 1), we argued that the charge distribution in the direction perpendicular to the oxidized graphite surface plays an important role in determining the film conformation and adhesion. The charge distributions at the contact layer (where the ionomer film are in direct contact with the graphite surface) are the most important, since it reflects the orientation of those charged specious (mostly water molecules, hydronium ions and sulfonate groups), which directly determine if preferable hydrogen bonds can be formed to enhance the adhesion between the film and the support. To have an idea of what the contact layer looks like, snapshots showing atoms in the film that are in direct contact with the oxidized surface are shown in **Figure 52** for a 1 nm film at $\lambda = 9$ on the hydroxylated **(a)** and epoxidized **(b)** surfaces. It is observed in the snapshot that more negatively charged sulfonic acid groups are present on the

hydroxylated graphite surface contributing to the adhesion between the film and the hydroxylated surface. Also more water molecules are in direct contact with the hydroxylated surface and are oriented in such a way that they form favorable hydrogen bonds with the surface (The distribution of specific conformations of water and hydronium in 1 nm films was presented previously.[140]). The aggregation of the sulfonate groups and water molecules near the hydroxylated surface result in an aqueous partial monolayer on the hydroxylated surface. Unlike the hydroxylated case, the epoxidized surface does not easily form bonds with the sulfonate group of the ionomer film due to Coulombic repulsion. Thus, the only way for the ionomer film to stay on the epoxidized surface is through the hydrogen bond with water and hydronium ions that are attracted to the surface. This is why there are less contact points between the epoxidized surface and the ionomer film. As the film thickness increases, the effect of this interfacial charge diminishes. Thus the 2 nm films show less change as a result of the surface oxidation, especially for the low hydration level systems.

The presence of an enhanced aqueous layer at the hydroxylated carbon surface should be manifested in the RDFs and associated coordination numbers. The sulfonate-sulfonate RDF appears most sensitive to surface oxidation. For all four sets of simulations in which nothing but the surface oxidation is changed, there is greatest sulfonate-sulfonate aggregation on the pristine surface, followed by the hydroxylated surface and then the epoxidized surface. Thus the charged surface appears to result in a more uniform distribution of sulfonate atoms over the surface, but the enhanced water at

the hydroxylated surface allows for some regrouping. There is very little impact of surface oxidation evident in the other four RDFs.

The distribution of water in the thin film is however affected by surface oxidation. It is observed that λ_{eff} of the film on the epoxidized graphite surface is generally higher compared with the film on the hydroxylated graphite surface. This is consistent with our previous observations: the hydrophilic domain of the ionomer film is located near the hydroxylated graphite surface; the water molecules are either trapped between the graphite surface and the hydrophobic portion of the ionomer film or located on the hydroxylated graphite surface that is far away from the ionomer. Only the water molecules that are trapped between the film and the support are counted for the calculation of $\lambda_{eff.}$ From the snapshots shown in **Figure 53**, it is clear that in the hydroxylated system, there is almost no water molecule in the upper portion of the Nafion film (the region that located far away from the oxidized graphite surface). However, in the epoxidized system, water molecules have a more even distribution within the film, both the lower portion (the region that is close to the oxidized graphite surface) and the upper portion of the film.

- **Unoxidized Systems with Nanoparticles**

The second simulation group contains a total of four simulations, each including a pristine graphite surface and a single Pt nanoparticle. The simulations include two hydration levels (λ = 3 and 9) and two film thicknesses (1 nm and 2 nm). The purpose of these simulations is to observe the impact of the presence of a Pt nanoparticle on the observations reported for the unoxidized and catalyst-free systems above. The five RDFs

for each simulation are reported in **Figures 39** through **43.** The corresponding coordination numbers are reported in **Table 10**.

In previous work, we examined the impact of a platinum nanoparticle embedded in a bulk Nafion membrane on the nanostructure of the aqueous domain[138]. We found that typically there is a higher water and sulfonic acid group density near the platinum nanoparticles. The result is also confirmed by a molecular dynamics study of the PEM-Pt_{256}-graphite interface, which argues that the strong interaction of sulfonic sites with Pt provides hydrophilic sites near the platinum nanoparticle and favor the location of stable water clustering near the Pt catalyst[110]. In the present work, the same trend of water and sulfonic acid density change near the platinum nanoparticles are observed.

The effect of the presence of a nanoparticle is likely restricted to the local proximity of the nanoparticle. The characteristics averaged over the entire film in the simulation, such as those in the RDFs and the coordination number should have at best a weak response to this introduction. Such is the case. The most significant difference in coordination numbers that we observed between systems with and without the Pt nanoparticle occurred for the 2 nm films, in which the sulfonate-sulfonate, sulfonate-hydronium, and water-water coordination numbers increased, while the sulfonate-water and hydronium-water coordination numbers decrease. The rationale is as follows: the Pt nanoparticle has a strong attraction to water molecules, as a result of which, a considerable amount of water molecules relocate themselves to be close to the Pt nanoparticle. This causes the water molecules near the sulfonic acid group and hydronium ion to decrease, and resulting in the drop in the hydration of sulfonate and

hydronium ions. Poorer hydration of the sulfonate group results in enhanced association of the sulfonate with hydronium ions. The water-water coordination number increases due to the aggregation of water around the Pt nanoparticle.

Snapshots illustrating the water distribution after introducing the Pt catalyst are shown in **Figure 54**. Obviously, after the introduction of Pt nanoparticle, the Pt nanoparticle attracted a considerable amount of water molecules to its surface, resulting in the majority of the surface of the Pt nanoparticle covered by a water layer, which contributes to the increase of water-water coordination number.

- **Oxidized Systems with Nanoparticles**

The third and final simulation group contains a total of eight simulations, each including an oxidized graphite surface and a single PtO nanoparticle. The simulations include a complete simulation matrix for two hydration levels (λ = 3 and 9), two film thicknesses (1 nm and 2 nm) and two types of oxidation (25% hydroxylation and 25% epoxidation). The purpose of these simulations is to observe the impact of the presence of a PtO nanoparticle on the observations reported for the oxidized and catalyst-free systems above. The five RDFs for each simulation are reported in **Figures 44** through **48**. The corresponding coordination numbers are reported in **Table 10**.

We observe that in addition to water molecules, a considerable amount of sulfonate groups and hydronium ions form preferentially around the PtO nanoparticle due to the strong electrostatic attractions between the negatively charged oxygen atoms on PtO and positively charged hydronium ions, which bring sulfonate groups with them to some extent. This aqueous surface layer is thus different from that at the Pt nanoparticle

surface, which seemed largely composed of water molecules, see **Figure 55 (a) and (b)**. It is clear that compared with the Pt surface (**Figure 55 (a)**), there are more sulfonate groups and hydroniums ions on the PtO surface (**Figure 55 (b)**).

To the extent that this nanoparticle acts as a hydrophilic anchor, the enhancement of water, hydronium ions and sulfonate groups directly at the surface of the nanoparticle can be propagated out to portions of the hydrated ionomer film not directly in contact with the nanoparticle, forming a better connected hydrophilic domain. **Figure 56 (a) and (b)** illustrate this point, through a comparison of the aqueous domain in a film in which no catalyst particle is present **(a)** and on in which an oxidized catalyst particle is present **(b)**. **Figure 56** not only shows that more sulfonate group and hydronium ions are located at the PtO surface but also a more continuous and larger hydrophilic domain. For most systems, water retention in the membrane also increases as a result of the presence of the PtO particle, based on comparison of the λ_{eff} for the eight pairs of simulations in which nothing is changed but the presence of the nanoparticle. But since the enhancement of water retention due to the presence of the nanoparticle is relatively localized and modest in magnitude, most of the various changes in RDFs reported in the previous section as a result of an increase in hydration are not observed.

It is found that all of the effects of film thickness on film nanostructure in the catalyst-free systems remain true in the PtO system. For example, the sulfonate-sulfonate coordination number decreases and the sulfonate-hydronium ion coordination number increases with increasing film thickness due to the flatter conformation for the thicker film. The coordination numbers of sulfonate-water, hydronium-water and water-water

increase due to better water retention. Thus, it is concluded that the introduction of PtO catalyst doesn't change the effect of film thickness. Additionally, the introduction of PtO nanoparticles also has negligible influence to the conclusion of surface oxidation on the film conformation due to the reason that the effects of the introduction of PtO is restricted to a local area near the catalyst.

Conclusions of Task 2

The purpose of part 1 of this task was to study the impact of oxidation on polymer film and nanoparticle adhesion for Pt/C catalysts in PEMFC catalyst layers. Molecular dynamics simulations were performed on various systems containing PtO nanoparticles and two different kinds of oxidized graphite surfaces (epoxidized and hydroxylated graphite) at different oxidation extents with the presence of Nafion thin film at four hydration levels of λ = 3, 6, 9, and 15. For the polymer electrolyte binding energy on the oxidized graphite surface, it is found that the epoxy and hydroxyl groups have very different effects on the binding energy of the polymer film. At a low extent of oxidation (10%), both surface oxides increase the binding energy between the Nafion polymer and the oxidized graphite surface. At high oxidation extents (25% and 50%), the hydroxylated graphite surface shows an increase in the magnitude of the binding energy, while the epoxidized graphite surface shows a decrease resulting eventually in film delamination. The dramatically different behavior of polymer on the two oxidized graphite surfaces is caused by the water/hydronium ion orientation on the oxidized graphite surface.

In part 2 of task 2, the effects of hydration level ($\lambda = 3$ and $\lambda = 9$), film thickness (1 nm and 2 nm), carbon support type (hydroxylated, epoxidized and pristine) and the presence of catalyst (Pt or PtO) on the morphology and property of the ionomer film in the catalyst layer of a PEMFC were investigated. Molecular dynamics simulations were performed for a total of 24 simulations. In the first set of simulations, the effect of hydration, film thickness and carbon support oxidation on the structure of the ionomer film are explored for systems with no catalyst. It is found that systems that are initialized with a uniform distribution of ionomer film on the surface relax to form highly irregular patches of hydrated ionomer on the surface, in which inhomogeneity in the film is found in both the lateral and perpendicular directions relative to the graphite surface. It is also found that the morphology of the aqueous domain in Nafion thin films change with degree of hydration in a qualitatively similar manner to bulk Nafion membranes, although the degree of water retention in these film is significantly lower. Specifically, high hydration level results in larger aqueous cluster size and thus a better connected hydrophilic domain, which will benefit the transport of proton. The thicker films retain more water and are less susceptible to delamination. Hydroxylation of the carbon support enhances ionomer film adhesion relative to the pristine surface. On the other hand, epoxidation of the carbon support can result in partial film delamination.

The most significant effect of presence of a Pt nanoparticle on the pristine graphite surface is the attraction of water molecules on the Pt nanoparticle surface, which forms an aqueous nanodomain on the Pt nanoparticle surface. In all simulations we observed good contact between the nanoparticle and the ionomer film. Breakages in the

pathway for proton transport from the catalyst to the membrane are therefore more likely to occur at points on the support surface where the catalyst is not located.

The impact of the presence of a PtO nanoparticle on an oxidized carbon surface is due to the charge distribution on the PtO surface, which creates a strong attraction not only to water molecules but also to sulfonate groups and hydronium ions. This changes the conformation of the nearby ionomer film, resulting in a better connected aqueous domain around the nanoparticle.

The insights from these simulations provide a molecular-level basis for the experimental observations that there is an optimal content of recast ionomer in the catalyst layer. If too little ionomer is present or if the film is not sufficiently hydrated, there is no pathway for proton transport from the catalyst to the PEM. Of course, if there is too much ionomer, the catalyst maybe buried under the film and rendered unreachable by the fuel in the vapor phase. This part also implies that epoxidation of the carbon surface during operation can result in ionomer film delamination, which reduces the binding energy of the catalysts, a possible precursor to catalyst detachment.

Task 3 Microscopic Analysis of Nafion Radiation Damage

In contrast to the tasks 1 and 2, the results of task 3 are based on experimental investigations of the catalyst layer. This work represents a preliminary study to investigate the possibility of measuring the nano-adhesion experimentally. Additionally, it helps to understand the effect of radiation damage on microscopic characterization of the catalyst layer. Nano-scale characterization often involves the use of Transmission Electron Microscopy (TEM) and Scanning Electron Microscopy (SEM)). However, while providing useful nanoscale information, the electron beam used in SEM and TEM can cause temporary or permanent change in the surface or bulk structure of the specimen[141]. Here, a detailed investigation of the radiation damage mechanism of the CL of PEMFCs, which contains both Nafion and carbon-supported platinum (Pt/C) catalyst, is conducted.

Background

As mentioned in previous tasks, characterizing the microstructure of the catalyst layer (CL) helps to elucidate microstructure-related process occurring during operation and degradation mechanisms contributing to PEMFC performance loss. Transmission Electron Microscopy (TEM) and Scanning Electron Microscopy (SEM) are essential and powerful analytical and imaging techniques for the evaluation of microstructural and microchemical changes that determine fuel cell performance stability. Many research groups take advantage of TEM and SEM in investigating the microstructural changes in the MEA of PEMFC [142-146]. However, while providing useful nanoscale information, the

electron beam used in SEM and TEM can cause temporary or permanent change in the surface or bulk structure of the specimen[141], especially for soft materials such as Nafion[147]. Under this constraint, the effects of radiation damage on the CL samples should be monitored and understood in order to ensure that the morphological effects being studied are intrinsic to material and not a consequence of the damage imposed by the electron beam damage. Verifying the effect of electron beam on the sample morphology modifications becomes even more important for in-situ experiments in the SEM chamber or in dynamic environmental TEM, which require that the image conditions (incident energy, beam current, aperture, working distance, scan speed etc.) be adjusted constantly to keep the sample stable[148,149].

Qualitative aspects of the mechanism of radiation damage in pure Nafion are well understood. For example, it is reported that the major component of Nafion exhibits substantial mass loss and instability under irradiation[150,151]. However, a detailed understanding of the radiation damage mechanism of the CL of PEMFCs, which contains both Nafion and carbon-supported platinum (Pt/C) catalyst, is not yet available. In the work described here, high angle annular dark field (HAADF) STEM images of CL samples containing 44 wt% Nafion were recorded as a function of the integrated beam dose using a Zeiss MERLIN SEM operated in scanning transmission (STEM) mode to investigate the effect of high-voltage scan speed on CL radiation damage. The choice of Nafion composition (44 wt%) is based on the experimental optimized Nafion content in the CL[101]. Radiation damage of CL samples with other Nafion content (29 and 76 wt%) and pure Nafion are also investigated to study the effect of components and composition

of the substance on radiation damage, which is believed to be relevant[152]. High resolution low loss electron energy loss spectrum (EELS) is recorded to confirm the mass loss of Nafion. Energy filtered transmission electron microscope (EFTEM) analysis is applied as key component to understand the radiation damage mechanism in CLs.

Experiment Details

- **Preparation of CLs and samples for TEM and STEM measurements**

Catalyst layers were prepared by a 'thin film decal' methods with several different Nafion to Pt/C ratios (29%, 44% and 76% of Nafion loading) by weight[39,153,154]. Following Sun et al.[155], minor modifications to the standard decal method are made; however the resulting CL samples should have similar characteristics to those of the CLs in MEAs since they experienced the standard procedure of MEA fabrication process. Catalyst inks were prepared by mixing a carbon support catalyst (XC-72, 20% Platinum on Vulcan) with distilled water, 5% Nafion solution (EW 1100, Ion power, Inc.) and isopropanol. The mixer was first ultrasonically agitated for 10 min and then stirred overnight to form a homogeneous ink. The catalyst ink was then brushed onto a decal surface of PTFE and dried until all the solvent evaporated. The samples with 76 wt% were dried at 80 °C in the vacuum oven; 44 wt% and 29 wt% samples were dried at room temperature. The process of brushing and heating is repeated until sufficient amount of material is deposit for testing. The catalyst layer formed on the decal was then hot pressed at 454 kg/cm^2 and 140 °C for 10 min. After hot pressing, the decals were soaked for 2 hours in 0.5 M sulfonic acid and immersed in deionized water for another 2 hours at

80 °C. The CLs were finally dried at room temperature. For comparison, pure Nafion film is also included to study the effect of Pt loading.

For the preparation of TEM and STEM samples, a small sample was first cut from the MEAs and then embedded in a low viscosity epoxy resin. The epoxy block is then sectioned with a Leica ultramicrotome at room temperature. The resultant film thickness is about 80 nm. The ultramicrotomed samples are finally transferred onto nickel-based TEM grids with 600 meshes.

- **HAADF STEM measurements**

The magnitude of the High-Angle Annular Dark-Field (HAADF) signal is linearly proportional to the mass-thickness of the specimen[156]. Therefore, thicker regions of the sample or areas with high density will appear bright, whilst a hole through the sample in the beam path will appear darker. To make measurements the probe beam (incident I = 197 µA; EHT = 15 KV, 20KV and 30 KV), is scanned at TV rates (351.85 $\mu m^2 s^{-1}$, 35.30 $\mu m^2 s^{-1}$ and 2.31 $\mu m^2 s^{-1}$) in a square raster (8.22 µm*8.59 µm) across the CL sample or pure Nafion sample for time periods varying from a few seconds up to of the order of several minutes. An image of the exposed area is then recorded. During the photo-recording, the beam is blanked for one or two seconds to provide a zero-signal ('black level') reference. The recorded STEM image is then analyzed by a histogram which identifies both the zero signal baseline value and the signal level in the irradiated region, which permits the brightness of the irradiated area to be properly determined. This procedure is then repeated, as required, to increase the deposited beam dose while simultaneously measuring the change in STEM image brightness. The relative change in

sample thickness with irradiation can then be found by plotting the signal intensity as a function of the beam dose deposited. To ensure that the intensity change is caused by radiation damage instead of system noise, five frames under the same irradiation conditions as those used for CL samples were acquired for Ferritin, which is stable under irradiation damage[157].

- **EFTEM and EELS analysis of the 44 wt% Nafion CL sample**

Transmission electron microscopy was used to study the CL sample structure before and after radiation damage as well as to provide information on chemical composition. A ZEISS LIBRA-120 equipped with an in-column (Omega) energy filter was used for high-resolution imaging. TEM experiments were performed at an acceleration voltage of 120kV, with an emission current of 5 μA, to ensure well-controlled electron-beam-induced sample damage so that the damage details can be captured before the whole sample is eaten up by the beam (usually a higher emission current is chosen for a high quality image, in which case, the Nafion sample will be eaten up by the beam very quickly). This equipment is especially suitable for acquiring electron energy loss (EELS) spectra and energy filtered TEM (EFTEM) images using electrons of specific energy loss, including elemental maps. For energy filtered imaging of Pt, the energy slit is adjusted to only allow electrons which have a specific amount of energy loss (Pt-$O_{2,3}$ edge 57 eV) to pass through.

For quantitative carbon, fluorine and sulfur mapping, a conventional three-window method was used with the two pre-edge windows providing background estimation. A typical energy window has a width of 20eV in the three-window imaging.

EELS spectrum is collected within a 1-micron-diameter area, followed by plural scattering removal.

Experiment Results

- **HAADF-STEM images, low loss EELS and signal intensity plots vs. beam dose**

A series of HAADF-STEM images are shown in **Figure 57** to illustrate the radiation damage process for the CL sample with 44 wt% Nafion. It is shown in the figure that with the beam dose increasing; the CL sample is damaged in such a way that the hole in the bottom left corner of the raster becomes larger, which indicates an obvious mass loss of CL component during the beam irradiation process. The elapsed time from **Figure 57(a)** to **Figure 57(d)** is 271 sec. Low loss EELS spectrums recorded for the 44 wt% Nafion CL sample in a chronological sequence confirm the mass loss of polymer with the beam dose increasing (**Figure 58 (a)**) by showing that the interband transition peak from π-π* (~6 eV) and the bulk plasmon peak[158] (~ 21 eV) decrease with the increase of beam dose. An EELS spectrum including the zero-loss peak is also included in **Figure 58 (b)** for the reader to have an idea of the sample thickness. The reason we believe that the 6 eV transition peak in the low loss EELS spectrum is a fingerprint for Nafion is based on the fact that the other two components in our sample do not have this characteristic peak according to their existing low loss EELS spectra[159,160].

To study the effect of incident energy on the CL radiation damage, beam dose vs. signal intensity plots of 44 wt% Nafion CLs at the scan speed of 35.30 $\mu m^2 s^{-1}$ are shown in **Figure 59**. The common curve behavior at all scan speeds is the presence of a plateau

at the initial accumulation of beam dose, followed by a gradual decrease with increasing beam dose to a second plateau. The first plateau can be explained by the fact that there exists a critical dose for the mass loss/structure loss for the sample undergoing radiation damages[141]. It is noticed from the figure that this critical dose is relatively insensitive to the incident energy change. The second plateau indicates that radiation damage will reach stable status after certain amount of beam dose, which indicates that most of the materials that are sensitive to radiation damage are gone. The presence of different slopes in the dropping part of the curve at different incident energies might be attributed to the different interaction of electrons with the sample at different incident energies. It is also observed that the lowest incident energy has the most drastic signal intensity change (high radiation damage). This observation matches the conclusion of Egerton et al[141], i.e. the inelastic damage cross section is inversely proposal to the incident electron speed. When the incident current is fixed, higher incident energy yields higher speed electrons, which penetrate the thin sample with less inelastic collisions and thus less inelastic damage (mass loss) to the thin sample. The sample used in our experiment has a thickness of 0.51 times mean free path (λ), which indicates that it is thin enough to avoid multiple scattering. Thus, it is suggested that radiation damage can be reduced by using high incident energy for thin samples (usually in the range of 0.3-1.0 times λ).

Figure 60 shows the signal intensity as a function of beam dose for 4 different Nafion wt% samples at the scan speed = 35.30 $\mu m^2 s^{-1}$ and EHT = 20 kV. It is noted that the Nafion composition in the sample will affect the degree of radiation damage: the CL sample with the lowest Nafion content (29 wt%) is most vulnerable to radiation damage

while the pure Nafion sample appears to be relatively more resistant to radiation damage for the same beam dose deposition. One possible explanation could be that the platinum nanoparticles in the CL sample play the role of facilitating the radiation damage process i.e. Pt acts like the catalyst. Therefore, it is not surprising that for the CL samples of high Pt/C composition (low Nafion content), there are more radiation active sites, as a result of which, the Nafion polymer in the CL samples of high Pt/C composition is more vulnerable compared with the samples of low Pt/C composition. Based on this explanation, it is expected that the Nafion located in the interface of Pt/C and Nafion will experience mass loss ahead of those located in the bulk. EFTEM images with Pt atoms highlighted taken in a chronological sequence well illustrates this point and are discussed shortly (section 3.2). From the first plateau of the curves, it is noticed that the critical beam dose varies with the Nafion content, the critical beam dose for 29 wt%, 44 wt%, 76 wt% CL and 100 % Nafion is $1.98*10^{7}$ $C.m^{-2}$, $3.81*10^{7}$ $C.m^{-2}$, $2.06*10^{7}$ $C.m^{-2}$ and $1.26*10^{7}$ $C.m^{-2}$ respectively. It is also interesting to observe that while the pure Nafion is relatively resistant to the beam radiation damage (since it undergoes the least signal intensity change with the same beam dose), it is the first to suffer from radiation damage compared with the CL samples.

To study the effect of scan speed on radiation damage, signal intensity change was plotted against time at three different scan speeds for samples of 44 wt% Nafion at EHT = 20 kV (see **Figure 61**). One observation from **Figure 61** is that at higher scan speeds (351.85 $\mu m^{2}s^{-1}$ and 35.30 $\mu m^{2}s^{-1}$), the signal intensity barely changed while at low

scan speed (2.31 $\mu m^2 s^{-1}$) the signal intensity changed drastically within the same amount of time. The scan speed is inversely related with the accumulated beam dose through

$$D_{dose} = \frac{I_{incident}}{V_{scan}} \times time \quad (1)$$

where D_{dose} is the accumulated beam dose, $I_{incident}$ is the incident current, V_{scan} is the scan speed and $time$ is the recording time. Thus it is obvious that a high scan speed results in low beam dose on the sample when other conditions are fixed. Since beam dose is proportional to the amount of radiation damage[161], a high scan speed is preferred from the perspective of reducing the extent of radiation damage.

- **Analytical TEM Images and Element Map of The 44 wt% CL after Damage**

Figure 62 shows a series of EFTEM images of a 44 wt% Nafion CL sample taken in a chronological sequence with the Pt element highlighted (appears bright). Based on the fact that holes in the sample also appear bright, an EFTEM image filtered at 0 eV is included in **Figure 63** to confirm that we are looking at real platinum particles instead of holes (the bright spots represents for Pt will appear dark in the 0 eV image). **Figure 63** confirms that most of the bright spots in the image are Pt particles. Based on the above observation, the features in **Figure 62** are discussed. One of the most obvious features revealed in **Figure 62** is that some of the platinum particles detached from the sample and were lost during the recording process. For example, refer to the 'circular' and 'triangular' mark in **Figure 62**. It is believed that the detachment of platinum particles is caused by the following mechanism: with the accumulation of beam dose, Nafion in the

CL sample starts to suffer from radiation damage and for those Nafion located around the platinum particle, the radiation damage process is facilitated because of the existence of platinum (catalyst). Since Nafion in the CL sample not only serves as the media for proton transport, but also serves as a binding agent to keep the platinum nanoparticle in position, it is possible that the platinum nanoparticles will detach from the surface due to lack of enough support. This explains why the CL sample that contains a high composition of Pt/C (catalyst) undergoes more drastic brightness intensity change as it appears in **Figure 60.** It has been suggested that an alternative cause of the loss of Pt nanoparticles would have something to do with the electrostatic repulsive force between the Pt and the surrounding environment after a certain amount of accumulation of charges on the sample surface. It is also worth pointing out that the high energy electrons can displace platinum particles off the specimen surface during the recording process ("electron beam sputtering") but this is not the cause of platinum detachment observed in **Figure 62**. This is because electron beam sputtering is categorized as elastic scattering damage, and it only occurs when the incident energy exceeds some threshold value. According to Egerton[141], the threshold value for platinum should be well above 200 keV. And for the TEM microscope we use, the highest possible incident energy is 120 keV, which rules out the electron beam sputtering mechanism in this case.

Another interesting feature observed in **Figure 62** is that the edge area of the sample (near the sample edge) is more vulnerable to radiation damage, where the sample suffers from mass loss and the edge area curls. By comparing **Figure 62 (a) and (c)**, one can easily observe the fact the sample from the edge area are eaten up by the electron

beam, i.e. the black area (hole) on the left side of the image has been expanded while the image has not been shifted right (refer to the position of the rectangle in the image, which remains at the same position in **Figure 62 (a)** and **(c)**). The reason for this could be the edge area is relatively thinner compared with the middle area.

The RGB image combining element maps of fluorine, carbon, sulfur of the 44 wt% Nafion CL sample before and after radiation damage is shown in **Figure 64** to study the variation of CL sample content before and after radiation damage. Obviously, the distribution of carbon changed drastically after exposed to electron beam. From **Figure 64 (b)**, it is noticed that at the edge of the burned hole, there is a carbon-rich zone (red area), which is believed to be the residue after radiation damage. Additionally, atomic displacement of fluorine is also obvious as shown in Figure 8 (b), where it accumulates in a place near the edge. It also should be mentioned that the element map for oxygen and platinum is not included in this RGB image because the most suitable ionization edge for the detection of oxygen and platinum occurs at relatively high energy losses (Pt: $M_{4,5}$-2122 eV and O: K-532 eV), where the intensity are relatively low and it is difficult to obtain spectral information with an optimize signal-to-noise ratio based on our sample thickness.

Conclusions of Task 3

The objective of task 3 was to investigate the microscope radiation damage mechanism of the catalyst layer of PEM fuel cells so that the researchers can be more cautious of their electron microscope results. For example, measuring the nano-force between the platinum catalyst and the carbon support of fuel cell electrode catalyst has

drawn research interest as one of the possible means to improve the fuel cell durability. With the aid of nano-force measurement sensors and electron microscope (SEM), it is now possible to conduct the measurement inside an SEM. However, this kind of measurement will require careful and slow operations, as a result of which, the sample need to be exposed to the beam for quite a long time, in which case, the radiation damage becomes important because it could drastically influence the accuracy of the measurement by destroying the Nafion polymer around the particles, which serves as a binding agent in the catalyst layer of PEM fuel cell.

After a series of careful investigations of the electron beam damage on samples of PEMFC catalyst layers, it is found that radiation damage to the CL of PEMFC usually occurs in the form of mass loss accompanied by variation of sample content and atom displacement of light atoms (such as Fluorine) in the Nafion polymer. Thin or defective areas of the CL sample appear more sensitive to radiation damage. The mass loss of the sample edges is accompanied by edge curl, which can cause ambiguity in imaging and quantitative measurement such as EELS spectrum. Moreover, existence of platinum particles in the CL sample facilitates the radiation damage of the surrounding Nafion, resulting in the detachment of the platinum nanoparticles due to lack of support. The feature makes the in-situ measurement of nano-adhesion inside the microscope inaccurate considering the binding agent role of the ionomer film around the catalyst nanoparticles as we illustrate in task 1. The measured nano-adhesion is estimate to be smaller than the real one to an unknown extent. Several strategies for mitigating the radiation damage are

also proposed, such as choosing a relatively higher voltage for a thin sample, a faster scan speed or lowering the beam dose within the reasonable imaging range.

CHAPTER 4: CONCLUSIONS

In this section of the disseration, we provide (i) summaries of each of the three tasks presented in the results and discussion section, (ii) a forward-looking statement on the significance and impact of this work and (iii) a description of promising future-work.

Summary of Task 1

Molecular dynamics simulations were performed to study the catalyst nanoparticle detachment mechanism from the nano-adhesion point of view in this task. The effects of nanoparticles sizes, shapes, Nafion thin film at different hydration levels (λ = 3, 6, 9 and 15) and the oxidation state of Pt/C on nanoparticle adhesion were investigated.

It is found that bigger nanoparticles yield better adhesion at all humidity levels. Additionally, nanoparticle shape of tetrahedron has a stronger connection to the carbon support compared to other shapes due to its 'anchor-like structure'. As for the effects of Nafion film, it acts like a binder to keep nanoparticles in place. The hydration level has a rather complicated effect on adhesion: at low hydration levels, the adhesion strength is dominated by the interaction between the nanoparticle and the polymer chain. Increasing the humidity level weakens this interaction and as a result of which, the adhesion force decreases as the hydration level goes up. At high hydration levels, the adhesion strength is dominated by the interaction between the graphite surface and Nafion. When the humidity level increases beyond a certain point, polymer chains become more flexible to

adjust to a more favorable configuration that yields a stronger connection with the carbon support, which can enhance the adhesion force.

As for the effect of surface oxidation on Pt/C, it is found that both the oxidation type and extent have effects on the nanoparticle adhesion. Generally speaking, the introduction of oxidation weakens the nano-adhesion between the carbon support and the catalyst. With the epoxidation of the graphite surface, the adhesion of PtO weakens further due to the electrostatic repulsion between the exposed oxygen atoms. However, with the hydroxylation of the graphite surface, the adhesion of PtO strengthens due to the electrostatic attraction between hydrogen on the surface and the oxygen on the nanoparticle.

The effect of oxidation extent on nano-adhesion is closely related with the ionomer film configuration on the surface, which will be influenced by the oxidation type and the humidity level of the system. At low levels of oxidation, the ionomer film stays firmly on the surface and the connection is stronger when the hydration level goes up. As a result of which, the binding energy for both epoxidized and hydroxylated surface increases. At high oxidation extent (25% and 50%), the binding energy decreases from $\lambda = 3$ to $\lambda = 9$ for the hydroxylated surface because the excess of water weakens the connection between the film and the hydroxylated surface. While for the epoxidized surface, as the degree of oxidation increases, the film is partially or fully detached from the surface, and its role as a binding agent is not fulfilled at those oxidation extents.

Summary of Task 2

Additional molecular dynamic simulation work was presented in task 2. Part 1 studied the impact of Pt/C oxidation on polymer film in PEMFC catalyst layers. Systems containing PtO nanoparticles and two different kinds of oxidized graphite surfaces (epoxidized and hydroxylated graphite) at different oxidation extents with the presence of Nafion thin film at four hydration levels of $\lambda = 3$, 6, 9, and 15 were investigated. Similar to the effect of oxidation of Pt/C on nanoparticle adhesion, it is found that the effect of oxidation of Pt/C depends on the oxidation type and degree of oxidation. At a low extent of oxidation (10%), both surface oxides increase the binding energy between the Nafion polymer and the oxidized graphite surface. At high oxidation extents (25% and 50%), the hydroxylated graphite surface shows an increase in the magnitude of the binding energy, while the epoxidized graphite surface shows a decrease resulting eventually in film delamination. The dramatically different behavior of polymer on the two oxidized graphite surfaces is caused by the water/hydronium ion orientation on the oxidized graphite surface.

In part 2 of task 2, the effects of hydration level ($\lambda = 3$ and $\lambda = 9$), film thickness (1 nm and 2 nm), carbon support type (hydroxylated, epoxidized and pristine) and the presence of catalyst (Pt or PtO) on the morphology and property of the ionomer film in the catalyst layer of a PEMFC were investigated. 24 simulations were grouped into three sets, they are i) systems with no catalysts, ii) unoxidized systems with Pt catalyst and iii) oxidized systems with PtO catalysts. In the first set of simulations, it is found that the ionomer film tends to form highly irregular patches of hydrated ionomer on the surface,

in which inhomogeneity in the film is found in both the lateral and perpendicular directions relative to the graphite surface. It is also found that the morphology of the aqueous domain in Nafion thin films change with degree of hydration in a qualitatively similar manner to bulk Nafion membranes, although the degree of water retention in these film is significantly lower. Additionally, the thicker films retain more water and are less susceptible to delamination. As for the effect of surface oxidation, hydroxylation of the carbon support enhances ionomer film adhesion relative to the pristine surface while epoxidation of the carbon support diminishes film adhesion.

In the second set of simulations, it is found that the presence of a Pt nanoparticle on the pristine graphite surface attracts water molecules on the surface, which forms an aqueous nanodomain on the surface. Good contact between the nanoparticle and the ionomer film is observed which leaves the breakages in the pathway for proton transport from the catalyst to the membrane to occur at points on the support surface where the catalyst is not located.

In the third set of simulations, the impact of the presence of a PtO nanoparticle is revealed. It is concluded that due to the charge distribution on the PtO surface, the PtO surface not only shows an strong attraction to water molecules but also to sulfonate groups and hydronium ions. As a result, the nearby ionomer film is in a better connection with the aqueous domain around the nanoparticle.

Summary of Task 3

In task 3, the radiation damage mechanism of the catalyst layer of PEMFCs is investigated. It is found that radiation damage to the CL of PEMFC usually occurs in the

form of mass loss accompanied by variation of sample content and atom displacement of light atoms (such as Fluorine) in the Nafion polymer. Thin or defective areas of the CL sample appear more sensitive to radiation damage. The mass loss of the sample edges is accompanied by edge curl. Moreover, the platinum particles in the CL sample will facilitate the radiation damage of the surrounding Nafion. Several strategies for mitigating the radiation damage are also proposed in this task, such as choosing a relatively higher voltage for a thin sample, a faster scan speed or lowering the beam dose within the reasonable imaging range.

Significance and Impact

The work presented here helps to better understand the nano-scale level structure and properties in the catalyst layer of the PEMFCs, which are difficult to visualize by experiment. The calculation of nano-adhesion between the catalyst and carbon support provides us with a new perspective of understanding the degradation mechanisms of carbon supported catalysts. The characterization of the Nafion ionomer film in the catalyst layer of PEMFCs is essential to increase the catalyst utilization rate, which will greatly reduce the current cost of the PEMFCs.

The experimental work deals with an unavoidable fact regarding the use of the powerful microscopic tools (SEM and TEM), which is the radiation damage. While we have to rely on the electron beam to obtain molecular level features of the sample, we have to live with the sample damage incurred by the electron beam. The experiments performed in the work shed light on the effect of radiation damage on the PEMFC catalyst layer sample characterization, especially to in-situ experiments such as

observation of nano-particle agglomeration, nano-adhesion measurement, etc. Without understanding the effect of radiation damage on the sample, it is meaningless to perform those experiments.

A meaningful contribution was made through this study to future hydrogen economy and catalyst industry involving the use of carbon supported catalysts. In this work, it has been shown that increasing the nano-adhesion force between the catalyst nanoparticle and its carbon substrate will effectively avoid the catalyst nanoparticle detachment and thus enhance the durability of the carbon supported catalyst. To do this, we can choose specific shapes and sizes of catalyst nanoparticles. We can also intentionally introduce specific functional groups onto the carbon surface, which will provide more stable anchor sites for the catalyst nanoparticles. Furthermore, the nano-adhesion between the catalyst and carbon support can also be strengthened by controlling ionomer film structure since we now know the factors that would influence its conformation and how the ionomer structure would influence the transport of proton and other species.

Future Work

From the point of view of understanding the degradation of carbon-supported catalysts and increasing catalyst utilization rate, future work involving systems containing more than one catalyst nanoparticle, carbon support with other defects such as vacancies and other textural anomalies due to carbon corrosion (e.g. pitting) would be useful. Additionally, in this work, the carbon support is simulated as graphite. However, there are other candidates such as carbon nanotube and carbon fiber, which are known to

be more resistant to carbon corrosion. It would be interesting to know how the nano-adhesion would change when the carbon substrate is replaced by those alternative carbon support materials. Similarly, different forms of catalysts can also be used in the nano-adhesion calculation. To reduce susceptibility to poisoning, Pt alloys are widely used as the cathode catalyst in PEMFCs. Nano-adhesion calculations involving Pt alloys or even other promising catalyst materials such as bio-inspired FePc-Py catalysts, which has recently drawn the industry attention, would be useful. Moreover, in the real catalyst layer, ionization of water molecules and charge delocalization of the hydronium ion to Zundel or Eigen ions occur. These larger ions are crucial for modeling proton transport; it is unclear whether they would have an impact on nanoparticle adhesion or ionomer film adhesion. Although simulations involving those species are beyond the scope of classical MD simulations, ab-initio MD simulations are capable of solving these problems. It is encouraged to include those effects in the future investigation. Last but not least, it would also be interesting to get the diffusivity of the specious such as the hydronium ions in the ionomer layer to see how the transportation property is related with the ionomer structure.

Experiments taking advantage of high-precision nano-scale force sensors can be conducted to experimentally measure the nano-adhesion between the support and catalyst. A comparison of that with the simulation data presented in this work will be interesting. Furthermore, to avoid or mitigate the radiation damage effect on the microstructure characterization inside microscopes, cryo-electron microscope is encouraged to use for imaging. Currently, there is a lack of sufficient connection

between the simulation results such as the ionomer film conformation located at the interface of electrode and electrolyte with its real conformation. It is important to verify the simulation results using experiments.

LIST OF REFERENCES

(1) Spiegel, C. *PEM fuel cell modeling and simulation using Matlab*, Elsevier: Oxford, 2008.

(2) Yu, Y.; Li, H.; Wang, H. J.; Yuan, X. Z.; Wang, G. J.; Pan, M. *Journal of Power Sources*, *205*, 10-23.

(3) Wilson, M. S.; Valerio, J. A.; Gottesfeld, S. *Electrochimica Acta* **1995**, *40*, 355-363.

(4) USDoE. Fuel Cell Technologies Program Multi-Year Research, Development and Demonstration Plan, 2007.

(5) T.Payne. Fuel Cells Durability & Performances; The Knowledge Press Inc.: Brookline, 2009.

(6) Beom, W. J.; Kalubarme, R. S.; Yun, K. S.; Park, C. J. *Applied Surface Science*, *257*, 9694-9702.

(7) Diloyan, G.; Sobel, M.; Das, K.; Hutapea, P. *Journal of Power Sources* **2012**, *214*, 59-67.

(8) Ferreira, P. J.; la O, G. J.; Shao-Horn, Y.; Morgan, D.; Makharia, R.; Kocha, S.; Gasteiger, H. A. *Journal of the Electrochemical Society* **2005**, *152*, A2256-A2271.

(9) Aragane, J.; Murahashi, T.; Odaka, T. *Journal of the Electrochemical Society* **1988**, *135*, 844-850.

(10) Blurton, K. F.; Kunz, H. R.; Rutt, D. R. *Electrochimica Acta* **1978**, *23*, 183-190.

(11) Gruver, G. A.; Pascoe, R. F.; Kunz, H. R. *Journal of the Electrochemical Society* **1980**, *127*, 1219-1224.

(12) Honji, A.; Mori, T.; Tamura, K.; Hishinuma, Y. *Journal of the Electrochemical Society* **1988**, *135*, 355-359.

(13) Bett, J. A. S.; Kinoshita, K.; Stonehart, P. *Journal of Catalysis* **1976**, *41*, 124-133.

(14) Mayrhofer, K. J. J.; Meier, J. C.; Ashton, S. J.; Wiberg, G. K. H.; Kraus, F.; Hanzlik, M.; Arenz, M. *Electrochemistry Communications* **2008**, *10*, 1144-1147.

(15) Ban, S.; Malek, K.; Huang, C. *Journal of Power Sources* **2013**, *221*, 21-27.

(16) More, K. L.; Reeves, K. S. "Microstructural characterization of PEM fuel cell MEAs"; 2005 DOE Hydrogen Program Review, 2005, Arlington, VA.

(17) Groves, M. N.; Malardier-Jugroot, C.; Jugroot, M. *Journal of Physical Chemistry C* **2012**, *116*, 10548-10556.

(18) Shao, Y. Y.; Yin, G. P.; Gao, Y. Z. *Journal of Power Sources* **2007**, *171*, 558-566.

(19) Yu, X. W.; Ye, S. Y. *Journal of Power Sources* **2007**, *172*, 145-154.

(20) Chen, Y. G.; Wang, J. J.; Liu, H.; Li, R. Y.; Sun, X. L.; Ye, S. Y.; Knights, S. *Electrochemistry Communications* **2009**, *11*, 2071-2076.

(21) Saha, M. S.; Li, R. Y.; Sun, X. L.; Ye, S. Y. *Electrochemistry Communications* **2009**, *11*, 438-441.

(22) Maiyalagan, T.; Viswanathan, B.; Varadaraju, U. *Electrochemistry Communications* **2005**, *7*, 905-912.

(23) Wu, G.; Li, D. Y.; Dai, C. S.; Wang, D. L.; Li, N. *Langmuir* **2008**, *24*, 3566-3575.

(24) Lepro, X.; Terres, E.; Vega-Cantu, Y.; Rodriguez-Macias, F. J.; Muramatsu, H.; Kim, Y. A.; Hayahsi, T.; Endo, M.; Miguel, T. R.; Terrones, M. *Chemical Physics Letters* **2008**, *463*, 124-129.

(25) Jafri, R. I.; Rajalakshmi, N.; Ramaprabhu, S. *Journal of Materials Chemistry* **2010**, *20*, 7114-7117.

(26) Cherstiouk, O. V.; Simonov, P. A.; Fenelonov, V. B.; Savinova, E. R. *Journal of Applied Electrochemistry* **2010**, *40*, 1933-1939.

(27) Kinoshit.K; Bett, J. *Carbon* **1973**, *11*, 237-247.

(28) Antonucci, P. L.; Pino, L.; Giordano, N.; Pinna, G. *Materials Chemistry and Physics* **1989**, *21*, 495-506.

(29) Giordano, N.; Antonucci, P. L.; Passalacqua, E.; Pino, L.; Arico, A. S.; Kinoshita, K. *Electrochimica Acta* **1991**, *36*, 1931-1935.

(30) Colmenares, L. C.; Wurth, A.; Jusys, Z.; Behm, R. J. *Journal of Power Sources* **2009**, *190*, 14-24.

(31) Imai, H.; Izumi, K.; Matsumoto, M.; Kubo, Y.; Kato, K.; Imai, Y. *Journal of the American Chemical Society* **2009**, *131*, 6293-6300.

(32) Hendriksen, B. L. M.; Frenken, J. W. M. *Physical Review Letters* **2002**, *89*.

(33) Hendriksen, B. L. M.; Bobaru, S. C.; Frenken, J. W. M. *Catalysis Today* **2005**, *105*, 234-243.

(34) Alayon, E. M. C.; Singh, J.; Nachtegaal, M.; Harfouche, M.; van Bokhoven, J. A. *Journal of Catalysis* **2009**, *263*, 228-238.

(35) Singh, J.; Nachtegaal, M.; Alayon, E. M. C.; Stotzel, J.; van Bokhoven, J. A. *Chemcatchem* **2010**, *2*, 653-657.

(36) Dam, V. A. T.; de Bruijn, F. A. *Journal of the Electrochemical Society* **2007**, *154*, B494-B499.

(37) Hull, R. V.; Li, L.; Xing, Y. C.; Chusuei, C. C. *Chemistry of Materials* **2006**, *18*, 1780-1788.

(38) Gasteiger, H. A.; Kocha, S. S.; Sompalli, B.; Wagner, F. T. *Applied Catalysis B-Environmental* **2005**, *56*, 9-35.

(39) Wilson, M. S.; Gottesfeld, S. *Journal of Applied Electrochemistry* **1992**, *22*, 1-7.

(40) Eikerling, M.; Kornyshev, A. A. *Journal of Electroanalytical Chemistry* **1998**, *453*, 89-106.

(41) Prasanna, M.; Cho, E. A.; Lim, T. H.; Oh, I. H. *Electrochimica Acta* **2008**, *53*, 5434-5441.

(42) Sun, L. L.; Ran, R.; Wang, G. X.; Shao, Z. P. *Solid State Ionics* **2008**, *179*, 960-965.

(43) Yoon, W.; Weber, A. Z. *Journal of the Electrochemical Society* **2011**, *158*, B1007-B1018.

(44) Eguchi, M.; Baba, K.; Onuma, T.; Yoshida, K.; Iwasawa, K.; Kobayashi, Y.; Uno, K.; Komatsu, K.; Kobori, M.; Nishitani-Gamo, M.; Ando, T. *Polymers* **2012**, *4*, 1645-1656.

(45) Cheng, X. L.; Yi, B. L.; Han, M.; Zhang, J. X.; Qiao, Y. G.; Yu, J. R. *Journal of Power Sources* **1999**, *79*, 75-81.

(46) Kim, H.-T. "Cost Effective and Durable Membrane Electrode Assembly for Automotive Applications"; 2012 Fuel Cell Seminar & Exposition, 2012, Mohegan Sun Convention Center, Uncasville, CT.

(47) Kreuer, K. D.; Paddison, S. J.; Spohr, E.; Schuster, M. *Chemical Reviews* **2004**, *104*, 4637-4678.

(48) Gierke, T. D.; Munn, G. E.; Wilson, F. C. *Journal of Polymer Science Part B-Polymer Physics* **1981**, *19*, 1687-1704.

(49) Hsu, W. Y.; Gierke, T. D. *Journal of Membrane Science* **1983**, *13*, 307-326.

(50) Yeager, H. L.; Steck, A. *Journal of the Electrochemical Society* **1981**, *128*, 1880-1884.

(51) Verbrugge, M. W.; Hill, R. F. *Journal of the Electrochemical Society* **1990**, *137*, 886-893.

(52) James, P. J.; Elliott, J. A.; McMaster, T. J.; Newton, J. M.; Elliott, A. M. S.; Hanna, S.; Miles, M. J. *Journal of Materials Science* **2000**, *35*, 5111-5119.

(53) Kreuer, K. D. *Journal of Membrane Science* **2001**, *185*, 29-39.

(54) Haubold, H. G.; Vad, T.; Jungbluth, H.; Hiller, P. *Electrochimica Acta* **2001**, *46*, 1559-1563.

(55) Rollet, A. L.; Gebel, G.; Simonin, J. P.; Turq, P. *Journal of Polymer Science Part B-Polymer Physics* **2001**, *39*, 548-558.

(56) Young, S. K.; Trevino, S. F.; Tan, N. C. B. *Journal of Polymer Science Part B-Polymer Physics* **2002**, *40*, 387-400.

(57) Fujimura, M.; Hashimoto, T.; Kawai, H. *Macromolecules* **1981**, *14*, 1309-1315.

(58) Fujimura, M.; Hashimoto, T.; Kawai, H. *Macromolecules* **1982**, *15*, 136-144.

(59) Lehmani, A.; Durand-Vidal, S.; Turq, P. *Journal of Applied Polymer Science* **1998**, *68*, 503-508.

(60) Porat, Z.; Fryer, J. R.; Huxham, M.; Rubinstein, I. *Journal of Physical Chemistry* **1995**, *99*, 4667-4671.

(61) Eikerling, M.; Kornyshev, A. A.; Stimming, U. *Journal of Physical Chemistry B* **1997**, *101*, 10807-10820.

(62) Datye, V. K.; Taylor, P. L.; Hopfinger, A. J. *Macromolecules* **1984**, *17*, 1704-1708.

(63) Mauritz, K. A.; Rogers, C. E. *Macromolecules* **1985**, *18*, 483-491.

(64) Elliott, J. A.; Hanna, S.; Elliott, A. M. S.; Cooley, G. E. *Macromolecules* **2000**, *33*, 4161-4171.

(65) Tovbin, Y. K.; Vasyatkin, N. F. *Colloids and Surfaces a-Physicochemical and Engineering Aspects* **1999**, *158*, 385-397.

(66) Liu, J.; Suraweera, N.; Keffer, D. J.; Cui, S.; Paddison, S. J. *Journal of Physical Chemistry C* **2010**, *114*, 11279-11292.

(67) Wu, D.; Paddison, S. J.; Elliott, J. A. *Energy & Environmental Science* **2008**, *1*, 284-293.

(68) Liu, J. W.; Selvan, M. E.; Cui, S.; Edwards, B. J.; Keffer, D. J.; Steele, W. V. *Journal of Physical Chemistry C* **2008**, *112*, 1985-1993.

(69) Alder, B. J.; Wainwright, T. E. *J. Chem. Phys.* **1959**, *31*, 459-466.

(70) Nose, S. *Molecular Physics* **1984**, *52*, 255-268.

(71) Nose, S. *J. Chem. Phys.* **1984**, *81*, 511-519.

(72) Tuckerman, M.; Berne, B. J.; Martyna, G. J. *J. Chem. Phys.* **1992**, *97*, 1990-2001.

(73) Peng, Z.; Yang, H. *Nano Today* **2009**, *4*, 143-164.

(74) Chen, J.; Lim, B.; Lee, E. P.; Xia, Y. *Nano Today* **2009**, *4*, 81-95.

(75) Lee, P.-C.; Han, T.-H.; Kim, D. O.; Lee, J.-H.; Kang, S.-J.; Chung, C.-H.; Lee, Y.; Cho, S. M.; Choi, H.-G.; Kim, T.; Lee, E.; Nam, J.-D. *Journal of Membrane Science* **2008**, *322*, 441-445.

(76) Fu, X. Y.; Wang, Y. A.; Wu, N. Z.; Gui, L. L.; Tang, Y. Q. *Langmuir* **2002**, *18*, 4619-4624.

(77) Subhramannia, M.; Pillai, V. K. *Journal of Materials Chemistry* **2008**, *18*, 5858-5870.

(78) Calvo-Munoz, E. M.; Selvan, M. E.; Xiong, R.; Ojha, M.; Keffer, D. J.; Nicholson, D. M.; Egami, T. *Physical Review E* **2011**, *83*.

(79) Qi, W. H.; Huang, B. Y.; Wang, M. P.; Yin, Z. M.; Li, J. *Journal of Nanoparticle Research* **2009**, *11*, 575-580.

(80) Yu, J. S. *Reviews on Advanced Materials Science* **2005**, *10*, 347-352.

(81) Coloma, F.; Sepulvedaescribano, A.; Fierro, J. L. G.; Rodriguezreinoso, F. *Langmuir* **1994**, *10*, 750-755.

(82) Coloma, F.; Sepulvedaescribano, A.; Rodriguezreinoso, F. *Journal of Catalysis* **1995**, *154*, 299-305.

(83) Lee, J.; Kim, J.; Hyeon, T. *Advanced Materials* **2006**, *18*, 2073-2094.

(84) Andrews, R.; Jacques, D.; Qian, D. L.; Rantell, T. *Accounts of Chemical Research* **2002**, *35*, 1008-1017.

(85) Dai, H. J. *Accounts of Chemical Research* **2002**, *35*, 1035-1044.

(86) De Jong, K. P.; Geus, J. W. *Catalysis Reviews-Science and Engineering* **2000**, *42*, 481-510.

(87) Dicks, A. L. *Journal of Power Sources* **2006**, *156*, 128-141.

(88) Serp, P.; Corrias, M.; Kalck, P. *Applied Catalysis a-General* **2003**, *253*, 337-358.

(89) Lee, K.; Zhang, J. J.; Wang, H. J.; Wilkinson, D. P. *Journal of Applied Electrochemistry* **2006**, *36*, 507-522.

(90) Anthony, J. W.; Bideaux, R. A.; BLadh, K. W.; Nichols, M. C. Handbook of Mineralogy; Mineral Data Publishing: Tucson, Arizona, 2003.

(91) Keffer, D. J., *https://trace.lib.utk.edu/home/davidkeffer/sites/atoms/animmn.html*.

(92) Croy, J. R.; Mostafa, S.; Liu, J.; Sohn, Y. H.; Heinrich, H.; Cuenya, B. R. *Catalysis Letters* **2007**, *119*, 209-216.

(93) Croy, J. R.; Mostafa, S.; Heinrich, H.; Cuenya, B. R. *Catalysis Letters* **2009**, *131*, 21-32.

(94) Naitabdi, A.; Behafarid, F.; Cuenya, B. R. *Applied Physics Letters* **2009**, *94*.

(95) Lerf, A.; He, H. Y.; Forster, M.; Klinowski, J. *Journal of Physical Chemistry B* **1998**, *102*, 4477-4482.

(96) Schniepp, H. C.; Li, J. L.; McAllister, M. J.; Sai, H.; Herrera-Alonso, M.; Adamson, D. H.; Prud'homme, R. K.; Car, R.; Saville, D. A.; Aksay, I. A. *Journal of Physical Chemistry B* **2006**, *110*, 8535-8539.

(97) Furmaniak, S.; Terzyk, A. P.; Gauden, P. A.; Harris, P. J. F.; Kowalczyk, P. *Journal of Physics-Condensed Matter* **2010**, *22*.

(98) M. J. Frisch, G. W. T., H. B. Schlegel, G. E. Scuseria,; M. A. Robb, J. R. C., J. A. Montgomery, Jr., T. Vreven,; K. N. Kudin, J. C. B., J. M. Millam, S. S. Iyengar, J. Tomasi,; V. Barone, B. M., M. Cossi, G. Scalmani, N. Rega,; G. A. Petersson, H. N., M. Hada, M. Ehara, K. Toyota,; R. Fukuda, J. H., M. Ishida, T. Nakajima, Y. Honda, O. Kitao,; H. Nakai, M. K., X. Li, J. E. Knox, H. P. Hratchian, J. B. Cross,; V. Bakken, C. A., J. Jaramillo, R. Gomperts, R. E. Stratmann,; O. Yazyev, A. J. A., R. Cammi, C. Pomelli, J. W. Ochterski,; P. Y. Ayala, K. M., G. A. Voth, P. Salvador, J. J. Dannenberg,;

V. G. Zakrzewski, S. D., A. D. Daniels, M. C. Strain,; O. Farkas, D. K. M., A. D. Rabuck, K. Raghavachari,; J. B. Foresman, J. V. O., Q. Cui, A. G. Baboul, S. Clifford,; J. Cioslowski, B. B. S., G. Liu, A. Liashenko, P. Piskorz,; I. Komaromi, R. L. M., D. J. Fox, T. Keith, M. A. Al-Laham,; C. Y. Peng, A. N., M. Challacombe, P. M. W. Gill,; B. Johnson, W. C., M. W. Wong, C. Gonzalez, and J. A. Pople,. **2004**, *Gaussian, Inc., Wallingford CT, 2004.*

(99) Becke, A. D. *J. Chem. Phys.* **1993**, *98*, 5648-5652.

(100) Selvan, M. E.; Keffer, D. J.; Cui, S. T. *Journal of Physical Chemistry C* **2011**, *115*, 18835-18846.

(101) Sasikumar, G.; Ihm, J. W.; Ryu, H. *Journal of Power Sources* **2004**, *132*, 11-17.

(102) Neria, E.; Fischer, S.; Karplus, M. *J. Chem. Phys.* **1996**, *105*, 1902-1921.

(103) Jorgensen, W. L.; Chandrasekhar, J.; Madura, J. D.; Impey, R. W.; Klein, M. L. *J. Chem. Phys.* **1983**, *79*, 926-935.

(104) Urata, S.; Irisawa, J.; Takada, A.; Shinoda, W.; Tsuzuki, S.; Mikami, M. *Journal of Physical Chemistry B* **2005**, *109*, 4269-4278.

(105) Fan, K. Q.; Jia, J. Y.; Zhu, Y. M.; Zhang, X. Y. *Chinese Physics B* **2011**, *20*.

(106) Feng, J. Q. *Colloids and Surfaces a-Physicochemical and Engineering Aspects* **2000**, *172*, 175-198.

(107) Attard, P.; Parker, J. L. *Physical Review A* **1992**, *46*, 7959-7971.

(108) Liem, S. Y.; Chan, K. Y. *Surface Science* **1995**, *328*, 119-128.

(109) Wu, G. W.; Chan, K. Y. *Journal of Electroanalytical Chemistry* **1998**, *450*, 225-231.

(110) Lamas, E. J.; Albuena, P. B. *Electrochimica Acta* **2006**, *51*, 5904-5911.

(111) Selvan, M. E.; He, Q.; Calvo-Munoz, E. M.; Keffer, D. J. *Journal of Physical Chemistry C* **2012**, *116*, 12890-12899.

(112) Carrillo, J. M. Y.; Dobrynin, A. V. *J. Chem. Phys.* **2012**, *137*.

(113) Johnson, K. L.; Kendall, K.; Roberts, A. D. *Proceedings of Royal Society London Series A* **1971**, *324*, 314.

(114) Derjaguin, B. V.; Muller, V. M.; Toporov, Y. P. *Progress in Surface Science* **1994**, *45*, 131-143.

(115) Ptak, A.; Kappl, M.; Moreno-Flores, S.; Gojzewski, H.; Butt, H. J. *Langmuir* **2009**, *25*, 256-261.

(116) Allen, F. H.; Bruno, I. J. *Acta Crystallographica Section B-Structural Science* **2010**, *66*, 380-386.

(117) Allen, F. H.; Kennard, O.; Watson, D. G.; Brammer, L.; Orpen, A. G.; Taylor, R. *Journal of the Chemical Society-Perkin Transactions 2* **1987**, S1-S19.

(118) Selvan, M. E.; Liu, J.; Keffer, D. J.; Cui, S.; Edwards, B. J.; Steele, W. V. *Journal of Physical Chemistry C* **2008**, *112*, 1975-1984.

(119) Liu, J.; Selvan, M. E.; Cui, S.; Edwards, B. J.; Keffer, D. J.; Steele, W. V. *Journal of Physical Chemistry C* **2008**, *112*, 1985-1993.

(120) Cui, S.; Liu, J.; Selvan, M. E.; Paddison, S. J.; Keffer, D. J.; Edwards, B. J. *Journal of Physical Chemistry B* **2008**, *112*, 13273-13284.

(121) He, Q.; Joy, D. C.; Keffer, D. J. *J. Power Sources* **2013**, *241*, 634-646.

(122) Callejas-Tovar, R.; Liao, W. T.; Mera, H.; Balbuena, P. B. *Journal of Physical Chemistry C* **2011**, *115*, 23768-23777.

(123) Schiros, T.; Andersson, K. J.; Pettersson, L. G. M.; Nilsson, A.; Ogasawara, H. *Journal of Electron Spectroscopy and Related Phenomena* **2010**, *177*, 85-98.

(124) Skulason, E.; Karlberg, G. S.; Rossmeisl, J.; Bligaard, T.; Greeley, J.; Jonsson, H.; Norskov, J. K. *Physical Chemistry Chemical Physics* **2007**, *9*, 3241-3250.

(125) Chen, S.; Ferreira, P. J.; Sheng, W.; Yabuuchi, N.; Allard, L. F.; Shao-Horn, Y. *Journal of the American Chemical Society* **2008**, *130*, 13818-13819.

(126) Chen, S.; Sheng, W.; Yabuuchi, N.; Ferreira, P. J.; Allard, L. F.; Shao-Horn, Y. *Journal of Physical Chemistry C* **2009**, *113*, 1109-1125.

(127) Chen, S.; Gasteiger, H. A.; Hayakawa, K.; Tada, T.; Shao-Horn, Y. *Journal of the Electrochemical Society* **2010**, *157*, A82-A97.

(128) Li, H. C.; McCabe, C.; Cui, S. T.; Cummings, P. T.; Cochran, H. D. *Molecular Physics* **2003**, *101*, 2157-2169.

(129) Cui, S. T.; Siepmann, J. I.; Cochran, H. D.; Cummings, P. T. *Fluid Phase Equilibria* **1998**, *146*, 51-61.

(130) Vishnyakov, A.; Neimark, A. V. *Journal of Physical Chemistry B* **2001**, *105*, 9586-9594.

(131) Vishnyakov, A.; Neimark, A. V. *Journal of Physical Chemistry B* **2001**, *105*, 7830-7834.

(132) Cui, S.; Liu, J.; Selvan, M. E.; Keffer, D. J.; Edwards, B. J.; Steele, W. V. *Journal of Physical Chemistry B* **2007**, *111*, 2208-2218.

(133) Wolf, D.; Keblinski, P.; Phillpot, S. R.; Eggebrecht, J. *J. Chem. Phys.* **1999**, *110*, 8254-8282.

(134) Kouji, M.; Naruo, S.; Makoto, I. *Carbon Nanotubes - From Research to Applications*, InTech, 2011.

(135) Khun, N. W.; Liu, E. *Surface & Coatings Technology* **2010**, *205*, 853-860.

(136) Zhang, X. L.; Zhong, X. H.; Meng, X.; Yi, G. W.; Jia, J. H. *Tribology Letters* **2012**, *46*, 65-73.

(137) Park, M. J.; Downing, K. H.; Jackson, A.; Gomez, E. D.; Minor, A. M.; Cookson, D.; Weber, A. Z.; Balsara, N. P. *Nano Letters* **2007**, *7*, 3547-3552.

(138) Selvan, M. E.; He, Q. P.; Calvo-Munoz, E. M.; Keffer, D. J. *Journal of Physical Chemistry C* **2012**, *116*, 12890-12899.

(139) McQuarrie, D. A. *Statistical Mechanics*, University Science Books: Sausalito,CA, 2000.

(140) He, Q.; Joy, D. C.; Keffer, D. J. *Royal Society of Chemistry Advances* **2013**, *3*, 15792-15804.

(141) Egerton, R. F.; Li, P.; Malac, M. *Micron* **2004**, *35*, 399-409.

(142) Akita, T.; Taniguchi, A.; Maekawa, J.; Sirorna, Z.; Tanaka, K.; Kohyama, M.; Yasuda, K. *J. Power Sources* **2006**, *159*, 461-467.

(143) Choi, I.; Lim, T.; Ahn, S. H.; Kwon, O. J.; Kim, J. J. Synthesis of Pt-based electrocatalysts with core-shell structure through electrochemical reduction for oxygen

reduction in PEMFC. In *Polymer Electrolyte Fuel Cells 11*; Gasteiger, H. A., Weber, A., Narayanan, S. R., Jones, D., Strasser, P., SwiderLyons, K., Buchi, F. N., Shirvanian, P., Nakagawa, H., Uchida, H., Mukerjee, S., Schmidt, T. J., Ramani, V., Fuller, T., Edmundson, M., Lamy, C., Mantz, R., Eds.; Electrochemical Soc Inc: Pennington, 2011; Vol. 41; pp 1051-1054.

(144) Ficicilar, B.; Bayrakceken, A.; Eroglu, I. *Int. J. Hydrogen Energy* **2010**, *35*, 9924-9933.

(145) Mamat, M. S.; Grigoriev, S. A.; Dzhus, K. A.; Grant, D. M.; Walker, G. S. *Int. J. Hydrogen Energy* **2010**, *35*, 7580-7587.

(146) Ma, S.; Solterbeck, C. H.; Odgaard, M.; Skou, E. *Appl. Phys. A-Mater. Sci. Process.* **2009**, *96*, 581-589.

(147) Mauritz, K. A.; Moore, R. B. *Chemical Reviews* **2004**, *104*, 4535-4585.

(148) Podor, R.; Ravaux, J.; Brau, H.-P. In Situ Experiments in the Scanning Electron Microscope Chamber. In *Scanning Electron Microscopy*; Kazmiruk, V., Ed.; InTech, 2012.

(149) Yoshida, K.; Zhang, X. D.; Bright, A. N.; Saitoh, K.; Tanaka, N. *Nanotechnology* **2013**, *24*.

(150) Bahr, G. F.; Johnson, F. B.; Zeitler, E. *Lab. Invest* **1965**, *14*, 337-395.

(151) Yakovlev, S.; Libera, M. *Microsc. Microanal.* **2006**, *12*, 996-997.

(152) Schneider, R. Scanning Electron Microscopy Studies of Nafion Deformation into Silicon Micro-Trenches for Fuel Cell Applications, Princeton University, 2008.

(153) Wilson, M. S.; Gottesfeld, S. *Journal of the Electrochemical Society* **1992**, *139*, L28-L30.

(154) Xie, J.; More, K. L.; Zawodzinski, T. A.; Smith, W. H. *Journal of the Electrochemical Society* **2004**, *151*, A1841-A1846.

(155) Sun, C. N.; More, K. L.; Zawodzinski, T. A. Investigation of Transport Properties, Microstructure, and Thermal Behavior of PEFC Catalyst Layers. In *Polymer Electrolyte Fuel Cells 10, Pts 1 and 2*; Gasteiger, H. A., Weber, A., Strasser, P., Edmundson, M., Lamy, C., Darling, R., Uchida, H., Schmidt, T. J., Shirvanian, P., Buchi, F. N., Mantz, R., Zawodzinski, T., Ramani, V., Fuller, T., Inaba, M., Jones, D., Narayanan, S. R., Eds., 2010; Vol. 33; pp 1207-1215.

(156) Joy, D. C.; Luo, S.; Gauvin, R.; Hovington, P.; Evans, N. *Scanning Microscopy* **1996**, *10*, 653-666.

(157) Galvez, N.; Fernandez, B.; Sanchez, P.; Cuesta, R.; Ceolin, M.; Clemente-Leon, M.; Trasobares, S.; Lopez-Haro, M.; Calvino, J. J.; Stephan, O.; Dominguez-Vera, J. M. *Journal of the American Chemical Society* **2008**, *130*, 8062-8068.

(158) Libera, M. R.; Disko, M. M. Electron Energy Loss Spectroscopy of Polymers. In *Transmission Electron Energy Loss Spectrometry in Materials Science and The EELS Atlas*; Ahn, C. C., Ed.; Wiley-VCH Verlag GmbH & Co. KGaA: Annandale, 2005.

(159) Murooka, Y.; Tanaka, N.; Hirono, S.; Hibino, M. *Materials Transactions* **2002**, *43*, 2092-2096.

(160) Ahn, C. C.; Krivanek, O. L.; Burgner, R. P.; Disko, M. M.; Swann, P. R. EELS ATLAS-A reference collection of electron energy loss spectra convering all stable elements, 1986.

(161) Fryer, J. R. *Ultramicroscopy* **1987**, *23*, 321-327.

APPENDIX

Tables

Table 1 Partial Charges and Lennard-Jones Parameters.

Partial charges and Lennard-Jones parameters for all the atoms in the oxidized graphite surfaces and oxidized platinum (PtO) nanoparticle.

epoxidized graphite[a]	**C0**	**C1**	**C2**	**C3**	**O**
partial charge (e)	0.0	0.25	0.5	0.75	-0.5
ε/k (K)	28	28	28	28	54.43
σ (Å)	3.4	3.4	3.4	3.4	3.05
hydroxylated graphite[b]	**C**	**CH**	**O**	**H**	
partial charge (e)	0.0	0.10	-0.32	0.22	
ε/k (K)	28.0	28.0	54.43	0.0	
σ (Å)	3.4	3.4	3.05	0.0	
oxidized platinum[c]	**Pt**	**Pt1**	**O**		
partial charge (e)	0.0	0.9918	-0.50		
ε/k (K)	2336	2336	77.75		
σ (Å)	2.41	2.41	3.165		

a. The number after 'C' represents the number of 'C-O' bonds formed on that particular carbon atom, for example, 'C0' represents for the carbon atom that has no epoxy functional group attached to it.

b. 'CH' represents for the carbon atom that has the hydroxyl group attached to it, and 'C' represents for the clean carbon atom.

c. 'Pt1' represents Pt atoms located on the nanoparticle surface and 'Pt' represents Pt atoms located in the core of PtO nanoparticle.

Table 2 The Number of Mobile Components in the Non-Oxidized Nano-Adhesion Measurement Systems.

Pt size	**2 nm**				**4 nm**				**6 nm**			
λ (H_2O/SO_3H)	3	6	9	15	3	6	9	15	3	6	9	15
number of Nafion	14	13	12	10	14	13	12	10	12	11	10	9
number of H_2O	420	975	1440	2100	420	975	1440	2100	360	825	2100	1890
Number of H_3O^+	210	195	180	150	210	195	180	150	180	165	150	135

Table 3 The Major Assumptions made in the Simulations of Task 1.

Assumptions:
1. The carbon electrode is modeled as pristine, epoxidized and hydroxylated graphite,.
2. The graphite model is defect free and contains 7 layers.
3. The catalyst nanoparticle is defect free and oxidation free.
4. Slight changes in the catalyst lattice parameter due to size are ignored.
5. The internal structures of catalyst and carbon electrode are rigid.
6. There is only one catalyst nanoparticle in the simulation box.
7. The CF groups in the Nafion molecules are treated as united atoms.
8. Structural diffusion of proton is not allowed.

Table 4 The Number of Atoms in Each Pt Nanoparticle.

	2 nm	4 nm	6 nm
cube	666	4631	14896
tetrahedron	56	364	1540
truncated octahedron	314	2735	8000
octahedron	80	660	2240

Table 5 The Binding Energies for the 2 nm Pt Nanoparticle.

2 nm Pt shape	binding energy per Pt atom basis	binding energy per Pt particle basis
cube	-0.0031 aJ	-2.0633 aJ
tetrahedron	-0.0044 aJ	-0.2467 aJ
truncated octahedron	-0.0013 aJ	-0.4115 aJ
octahedron	-0.0017 aJ	-0.1369 aJ

Table 6 Binding Energies for All Oxidized systems and Clean Graphite-Pt System.

λ	bare	3	9
clean graphite-Pt system	-0.53 aJ	-6.53 aJ	-7.22 aJ
10% hydroxylated graphite-PtO system	-1.44 aJ	-15.9 aJ	-16.0 aJ
25% hydroxylated graphite-PtO system	-1.73 aJ	-19.1 aJ	-17.3 aJ
50% hydroxylated graphite-PtO system	-2.45 aJ	-24.9 aJ	-23.9 aJ
10% epoxidized graphite-PtO system	-1.48 aJ	-14.9 aJ	-15.8 aJ
25% epoxidized graphite-PtO system	-1.45 aJ	-11.6 aJ	-13.7 aJ

Table 7 Adhesion Forces for All Oxidized Systems and Clean Graphite-Pt System.

λ	bare	3	9
clean graphite-Pt system	-0.29 nN	-6.21 nN	-7.36 nN
10% hydroxylated graphite-PtO system	-6.97 nN	-55.8 nN	-88.2 nN
25% hydroxylated graphite-PtO system	-9.44 nN	-122 nN	-150 nN
50% hydroxylated graphite-PtO system	-13.9 nN	-217 nN	-234 nN
10% epoxidized graphite-PtO system	-7.05 nN	-12.3 nN	-46.5 nN
25% epoxidized graphite-PtO system	-9.00 nN	-73.3 nN	-141 nN

Table 8 Average Number of Water Molecules Retained in the Catalyst Layer.

Average number of water molecules retained in the catalyst layer for the 2 nm cubic Pt systems (non-oxidized) and all the oxidized Pt/C systems at different hydration levels.

effective λ	3	6	9	15
2 nm cubic Pt/clean graphite system[a]	2.65	4.32	6.48	11.71
10% hydroxylated system	2.60	/[b]	6.78	/[b]
25% hydroxylated system	2.70	/[b]	7.69	/[b]
50% hydroxylated system	2.75	4.97	7.35	11.5
10% epoxidized system	2.89	/[b]	7.73	/[b]
25% epoxidized system	3.00	/[b]	8.94	/[b]
50% epoxidized system	3.00	5.76	8.60	14.0

a. All the other systems in the table contain a 4 nm tetrahedral PtO nanoparticle.

b. Not all combinations of oxidized carbon surface and hydration level were studied.

Table 9 Equilibrium Distances and Adhesion Forces.

Comparison of equilibrium distance and adhesion force for 2 nm Pt nanoparticle of different shapes at hydration level of $\lambda = 3$.

Pt shape	bare system equilibrium distance	$\lambda = 3$ system equilibrium distance	bare system adhesion force	$\lambda = 3$ system adhesion force	adhesion force gain per atom basis
cube	0.33 nm	0.32 nm	-11.88 nN	-16.62 nN	0.007 nN
tetrahedron	0.32 nm	0.39 nm	-1.37 nN	-3.79 nN	0.043 nN
truncated octahedron	0.32 nm	0.32 nm	-2.19 nN	-6.44 nN	0.014 nN
octahedron	0.31 nm	0.30 nm	-0.68 nN	-3.09 nN	0.030 nN

Table 10 Simulation Conditions and Coordination Numbers.

Simulation conditions, including surface oxidation, catalyst, film thickness, nominal and effective hydration levels, film surface area, and coordination numbers of S of SO_3^-/S of SO_3^- within 6.9 Å, S of SO_3^-/O of H_2O within 6.0 Å, S of SO_3^-/O of H_3O^+ within 5.5 Å, O of H_3O^+/O of H_2O within 4.2 Å and O of H_2O/O of H_2O within 5.1 Å.

run #	carbon surface	catalyst nanoparticle	nominal film thickness (nm)	nominal hydration (λ = H_2O per HSO_3)	effective hydration λ_{eff}	film surface area (10^5 Å^2)	$S(SO_3^-)$ - $S(SO_3^-)$	$S(SO_3^-)$ - $O(H_2O)$	$S(SO_3^-)$ - $O(H_3O^+)$	$O(H_2O)$ - $O(H_3O^+)$	$O(H_2O)$ - $O(H_2O)$
1	pristine	no catalyst	1	3	2.3	1.16	5.0	2.8	1.6	1.3	1.8
2	pristine	no catalyst	1	9	3.8	1.08	7.7	3.7	1.3	1.6	5.5
3	pristine	no catalyst	2	3	2.6	2.32	2.3	3.4	2.6	1.5	1.9
4	pristine	no catalyst	2	9	7.8	2.64	2.4	7.1	2.3	2.9	6.0
5	epoxidized	no catalyst	1	3	1.7	1.13	2.9	2.3	1.7	1.0	1.8
6	epoxidized	no catalyst	1	9	4.2	1.13	3.5	4.2	1.4	2.0	5.4
7	epoxidized	no catalyst	2	3	2.6	2.39	2.3	3.4	2.5	1.4	1.9
8	epoxidized	no catalyst	2	9	7.7	2.67	2.5	7.0	2.4	2.8	6.0
9	hydroxylated	no catalyst	1	3	2.3	1.17	3.2	2.2	1.6	1.1	2.1

Table 10 (continued)

run #	carbon surface	catalyst nanoparticle	nominal film thickness (nm)	nominal hydration (λ = H_2O per HSO_3)	effective hydration λ_{eff}	film surface area (10^5 Å^2)	$S(SO_3^-)$ - $S(SO_3^-)$	$S(SO_3^-)$ - $O(H_2O)$	$S(SO_3^-)$ - $O(H_3O^+)$	$O(H_2O)$ - $O(H_3O^+)$	$O(H_2O)$ - $O(H_2O)$
10	hydroxylated	no catalyst	1	9	3.4	1.08	6.6	3.8	1.4	1.6	5.2
11	hydroxylated	no catalyst	2	3	2.3	2.33	2.3	3.0	2.8	1.3	1.9
12	hydroxylated	no catalyst	2	9	7.5	2.65	2.6	6.6	2.4	2.8	5.7
13	pristine	Pt	1	3	2.2	1.14	5.1	2.8	1.7	1.3	1.6
14	pristine	Pt	1	9	3.9	1.09	6.3	4.4	1.3	1.7	5.2
15	pristine	Pt	2	3	2.5	2.30	3.1	2.7	3.0	1.3	2.3
16	pristine	Pt	2	9	8.0	2.66	2.7	6.6	2.5	2.7	6.2
17	epoxidized	PtO	1	3	1.8	1.14	5.5	1.9	1.6	0.9	1.0
18	epoxidized	PtO	1	9	5.5	1.19	5.8	4.7	1.3	2.1	4.2
19	epoxidized	PtO	2	3	2.6	2.37	2.8	2.9	2.8	1.3	2.0
20	epoxidized	PtO	2	9	8.5	2.71	2.4	6.6	2.4	2.6	5.7
21	hydroxylated	PtO	1	3	2.3	1.17	6.0	2.2	1.7	1.2	2.0

Table 10 (continued)

run #	carbon surface	catalyst nanoparticle	nominal film thickness (nm)	nominal hydration (λ = H_2O per HSO_3)	effective hydration λ_{eff}	film surface area (10^5 Å^2)	$S(SO_3^-)$ - $S(SO_3^-)$	$S(SO_3^-)$ - $O(H_2O)$	$S(SO_3^-)$ - $O(H_3O^+)$	$O(H_2O)$ - $O(H_3O^+)$	$O(H_2O)$ - $O(H_2O)$
22	hydroxylated	PtO	1	9	3.2	1.05	6.5	2.7	1.6	1.4	5.5
23	hydroxylated	PtO	2	3	2.6	2.37	2.3	3.2	2.7	1.4	2.2
24	hydroxylated	PtO	2	9	7.8	2.68	2.6	6.3	2.5	2.6	5.9

Table 11 Organization of Radial Density Distribution Figures.

The content of the figures of a complete set of fifteen radial density distributions presented task 2 is summarized in the table below.

	pristine & oxidized carbon surfaces in the absence of catalyst nanoparticles	**pristine carbon surface & Pt catalyst nanoparticle**	**oxidized carbon surface & PtO catalyst nanoparticle**
S of SO_3^-/S of SO_3^-	Figure 34	Figure 39	Figure 44
S of SO_3^-/O of H_2O	Figure 35	Figure 40	Figure 45
S of SO_3^-/O of H_3O^+	Figure 36	Figure 41	Figure 46
O of H_3O^+/O of H_2O	Figure 37	Figure 42	Figure 47
O of H_2O/O of H_2O	Figure 38	Figure 43	Figure 48

Figures

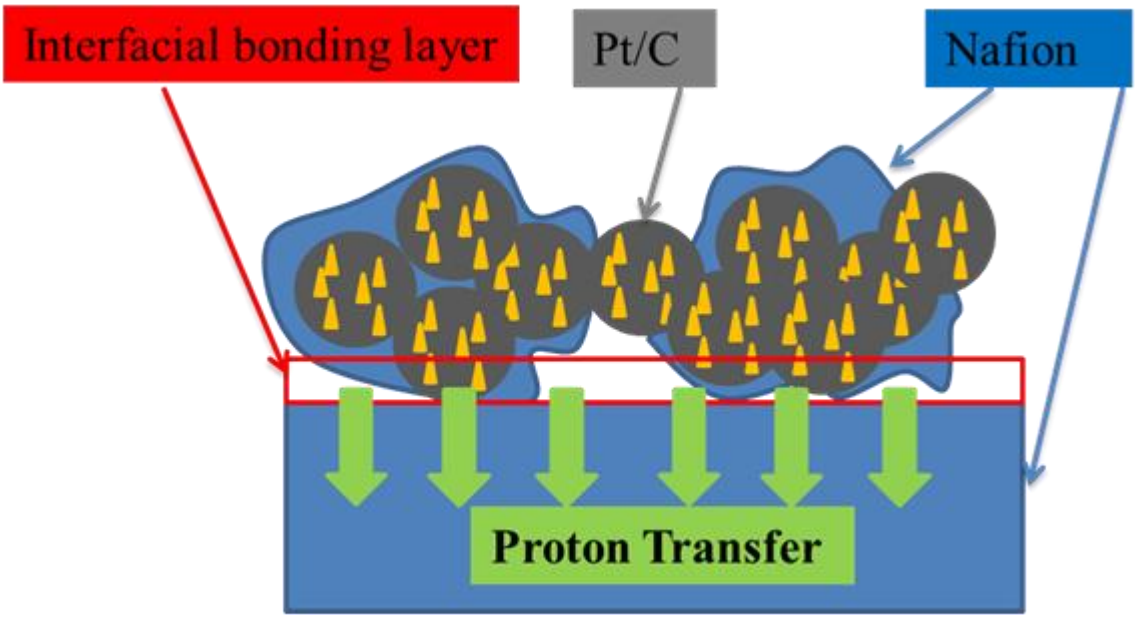

Figure 1 Interface of the Catalyst Layer and Electrolyte Membrane.

A schematic showing the interface of the catalyst layer and electrolyte membrane in polymer electrolyte membrane fuel cells. Color legend: blue is the Nafion ionomer, gold is the catalyst nanoparticles, grey is the carbon support. The green arrow denotes the proton passage and the red rectangular indicates the interfacial bonding region.

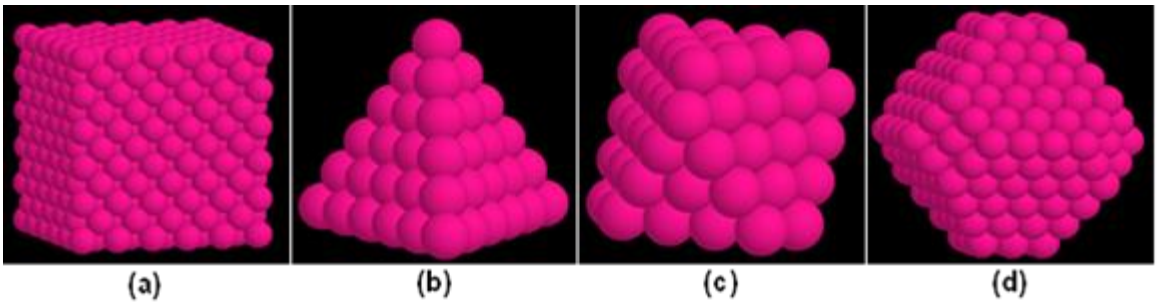

Figure 2 Pt Models.

Molecular models for the platinum nano-particle. (a) tetrahedron (b) cube (c) octahedron (d) truncated octahedron. Color legend: pink is platinum.

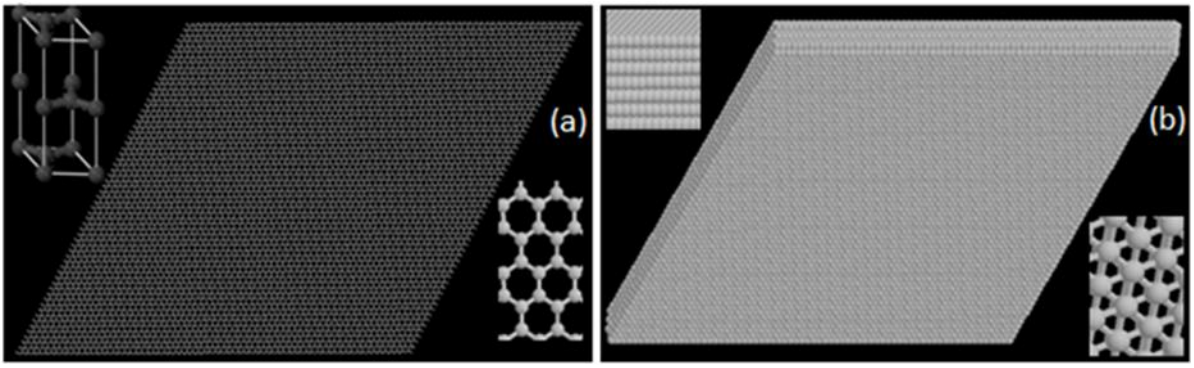

Figure 3 Clean Graphite Model.

Graphite model. (a) Single plane of graphite model with the graphite unit cell in the top left corner and a top view close-up of the graphite layer in the bottom right corner (b) seven-plane graphite model used in our simulation with a side view close-up in the top left corner and top view close-up in the bottom right corner. Color legend: grey is carbon.

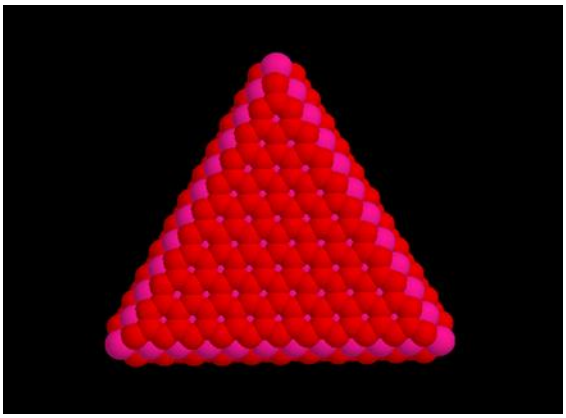

Figure 4 PtO Model.

Molecular models for the oxidized platinum nano-particle. Color legend: pink is platinum, red is oxygen.

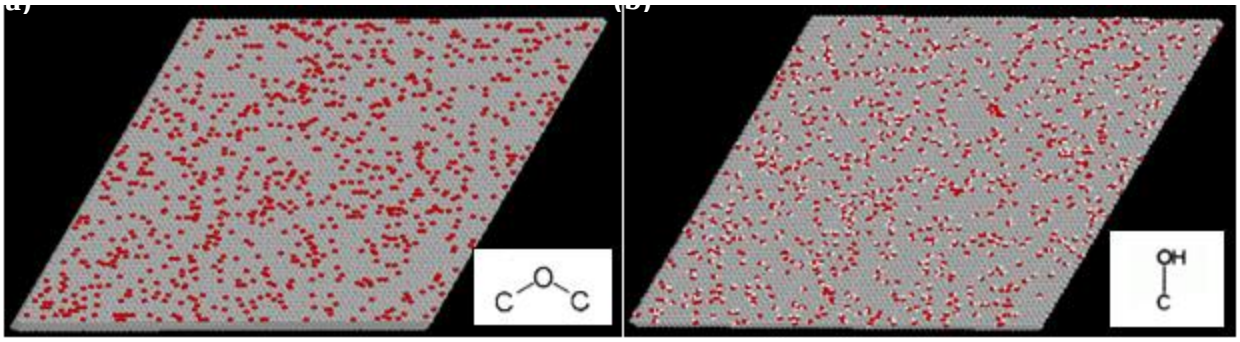

Figure 5 Oxidized Graphite Models.

Oxidized graphite model. (a) 10 % epoxidized graphite model with the epoxy functional group shown in the bottom right corner. (b) 10 % hydroxylated graphite with the hydroxyl functional group shown in the bottom right corner. Color legend: grey is C, red is O and white is H.

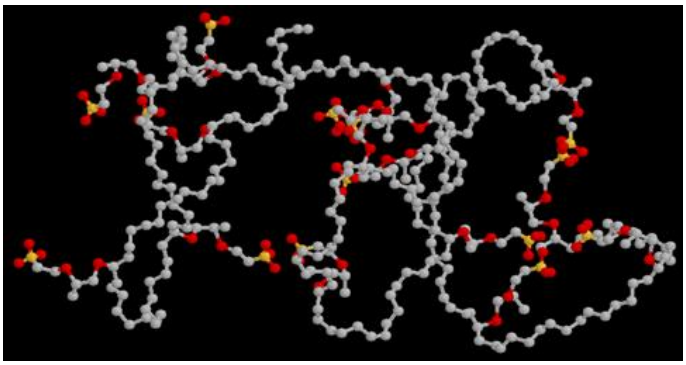

Figure 6 Nafion Model.

Nafion model. A single chain is shown. Color legend: grey is CF_x, orange is sulfur, red is oxygen.

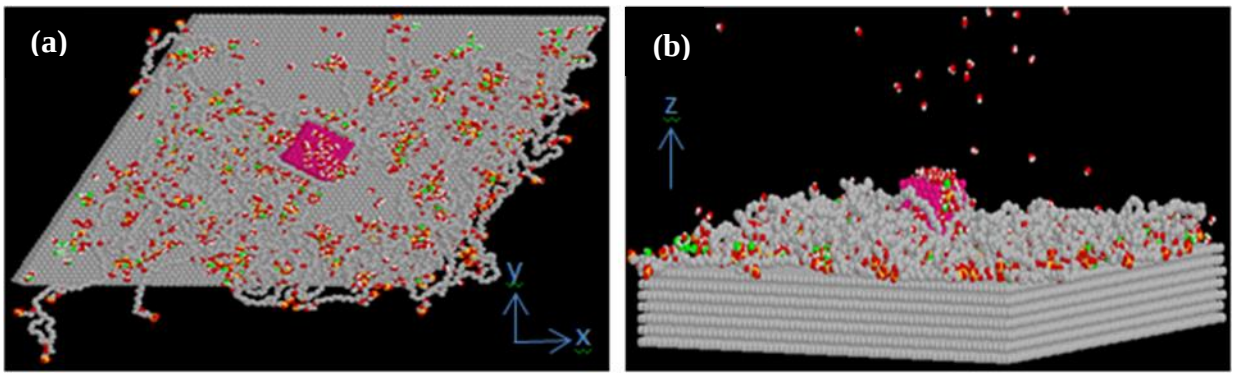

Figure 7 The Equilibrated Cubic Non-Oxidized Pt System.

Snapshot of an equilibrated system contains a 2 nm cubic Pt nanoparticle at the hydration level of λ=3. (a) top view (b) side view.

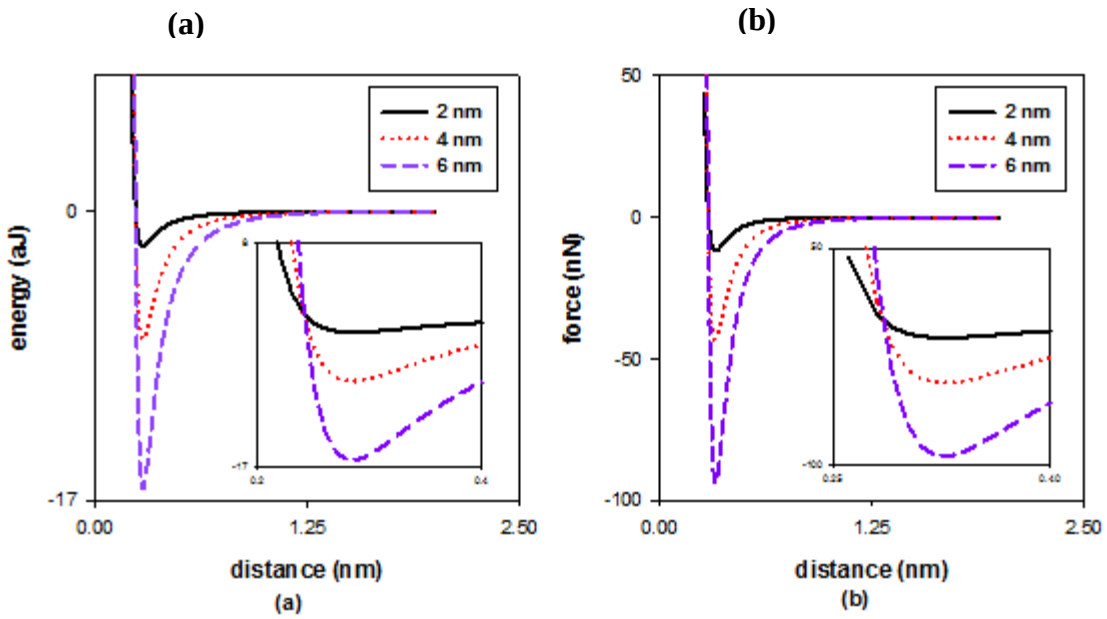

Potential and force curves for bare systems contain a cubic Pt of different sizes. (a) potential curve (b) force curve.

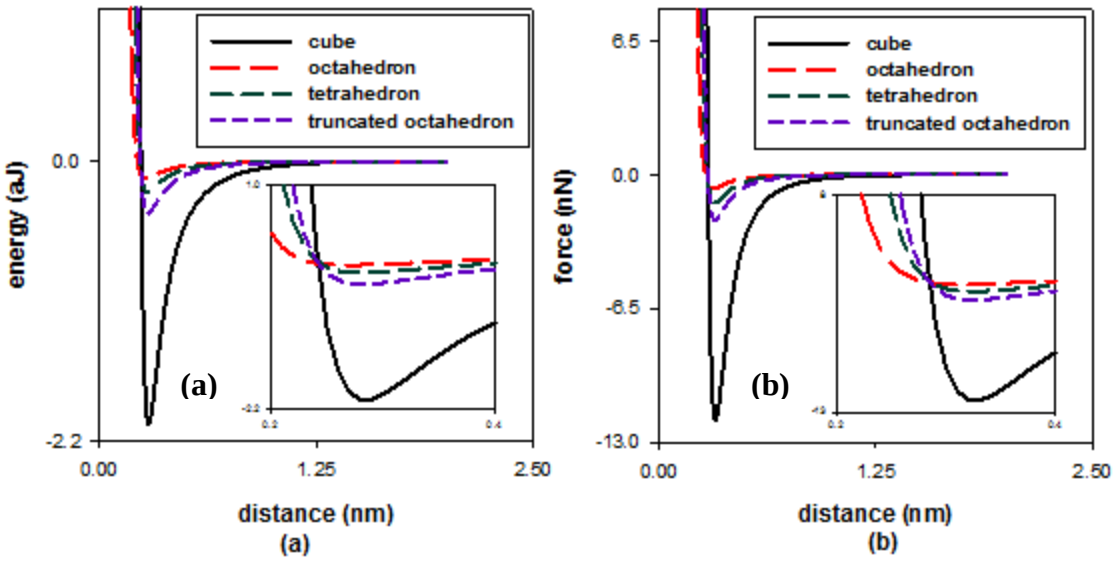

Figure 9 Potential and Force Curves for Bare Systems-Effect of Pt Shapes

Potential and force curves for bare systems contain a 2nm Pt of different shapes. (a) potential curve (b) force curve.

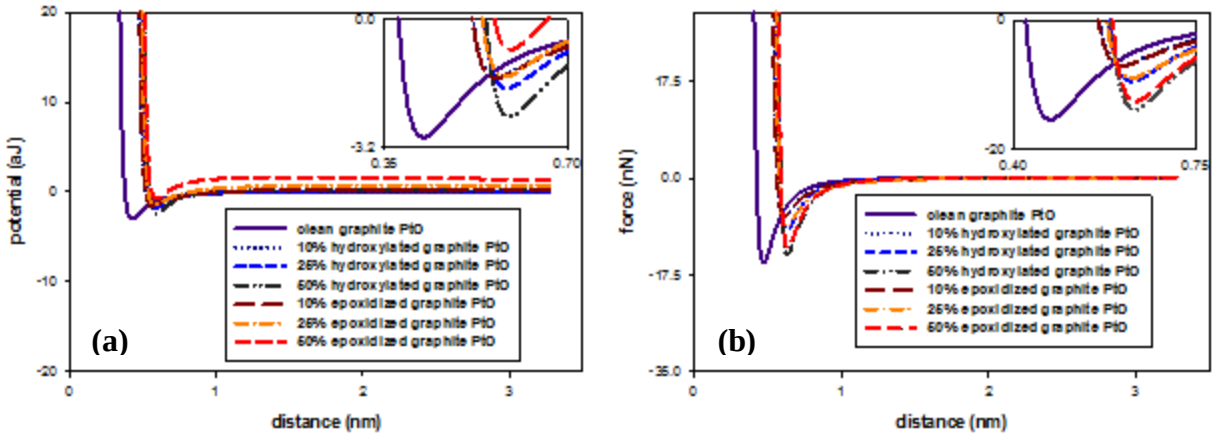

Figure 10 Potential and Force Curves for Oxidized Bare Systems.

Binding energy (a) and adhesion force (b) curves for all bare systems (no Nafion film).

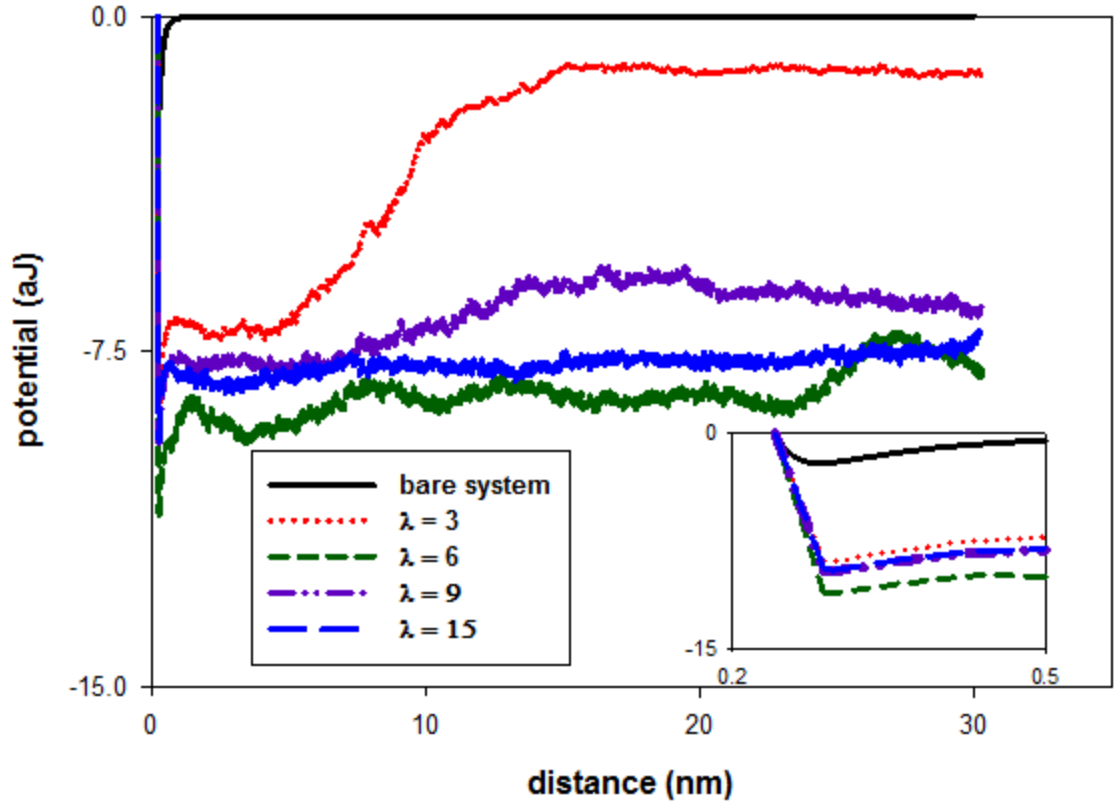

Figure 11 Potential Curves for Non-Oxidized Pt/C Systems.

Potential curves for non-oxidized Pt/C systems contain a 2 nm cubic Pt and different hydration levels.

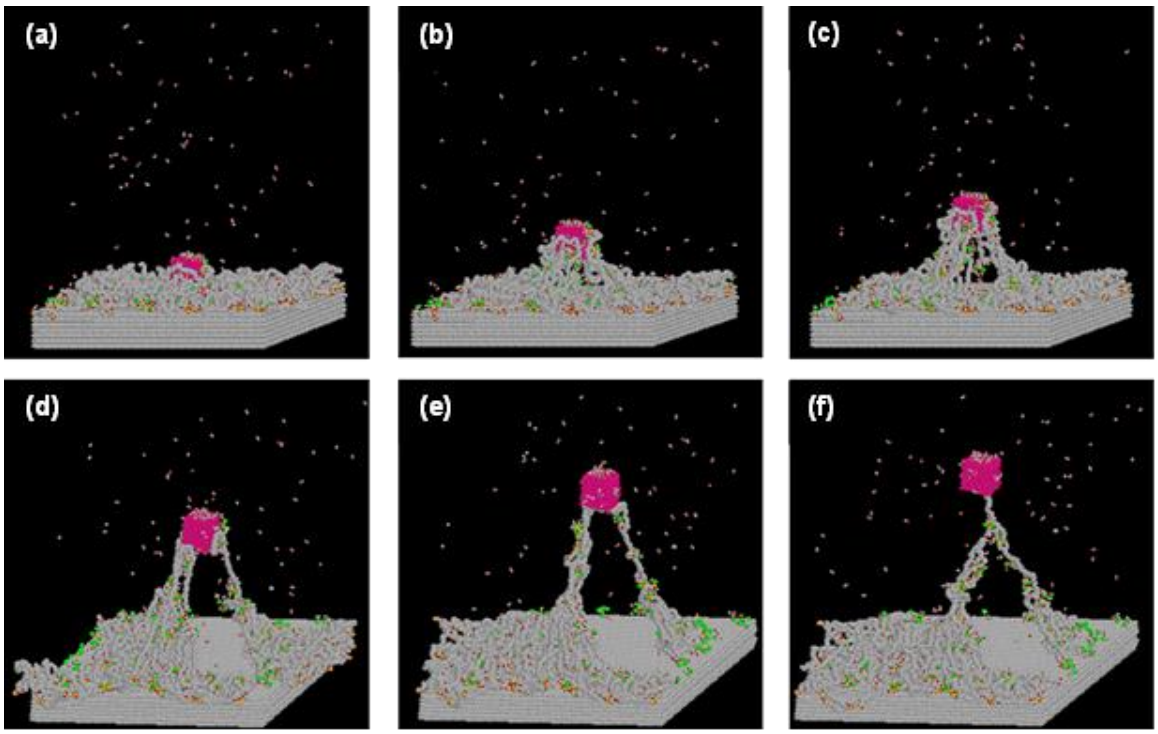

Figure 12 Snapshot of Pt Detachment Process.

Snapshots illustrating the process of Pt detachment from the graphite surface for a system includes a 2 nm cubic Pt at the hydration level of λ=3.

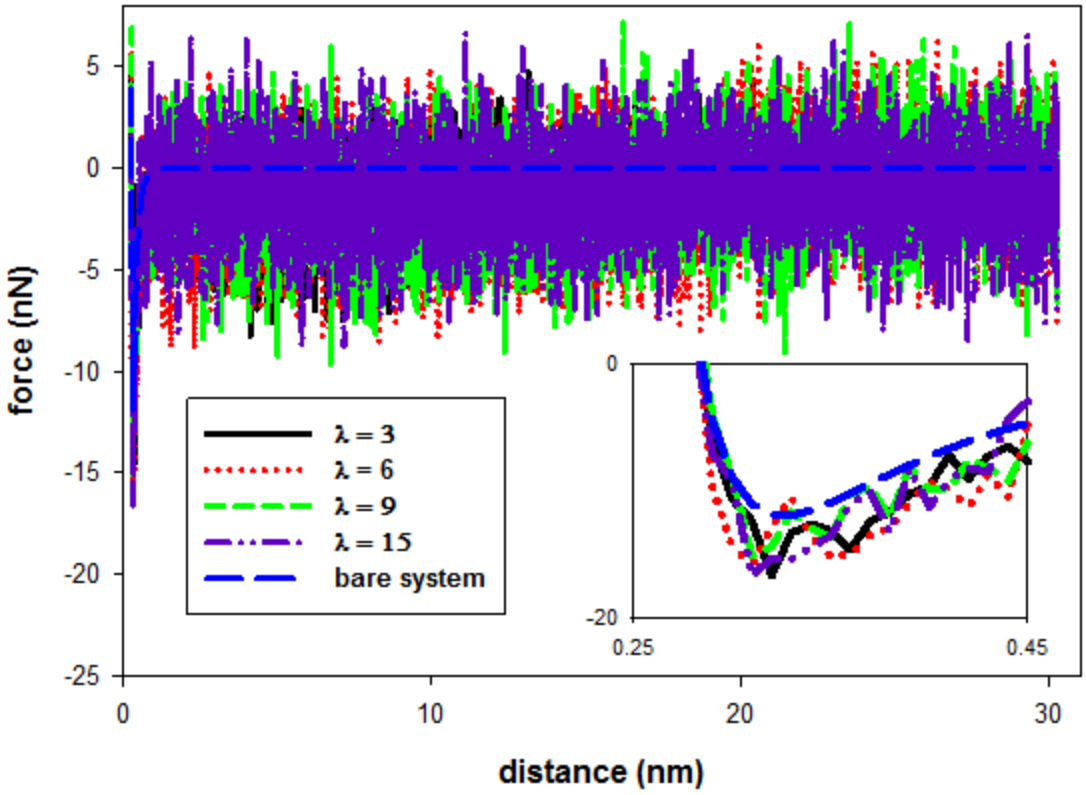

Figure 13 Force Curves for Non-Oxidized Pt/C Systems-Effect of Hydration.

Force curves for systems contain a 2 nm cubic Pt and different hydration levels.

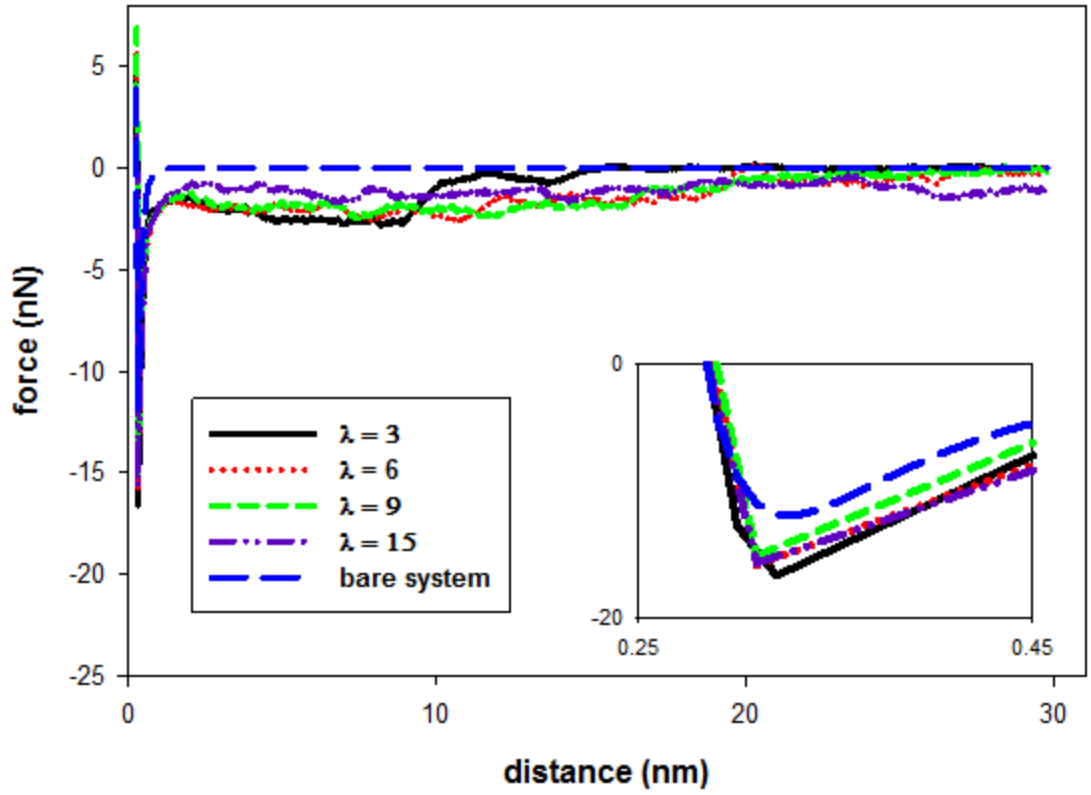

Figure 14 Filtered Force Curves for Non-Oxidized Pt/C systems.

Filtered force curves for systems contain a 2 nm cubic Pt and different hydration levels.

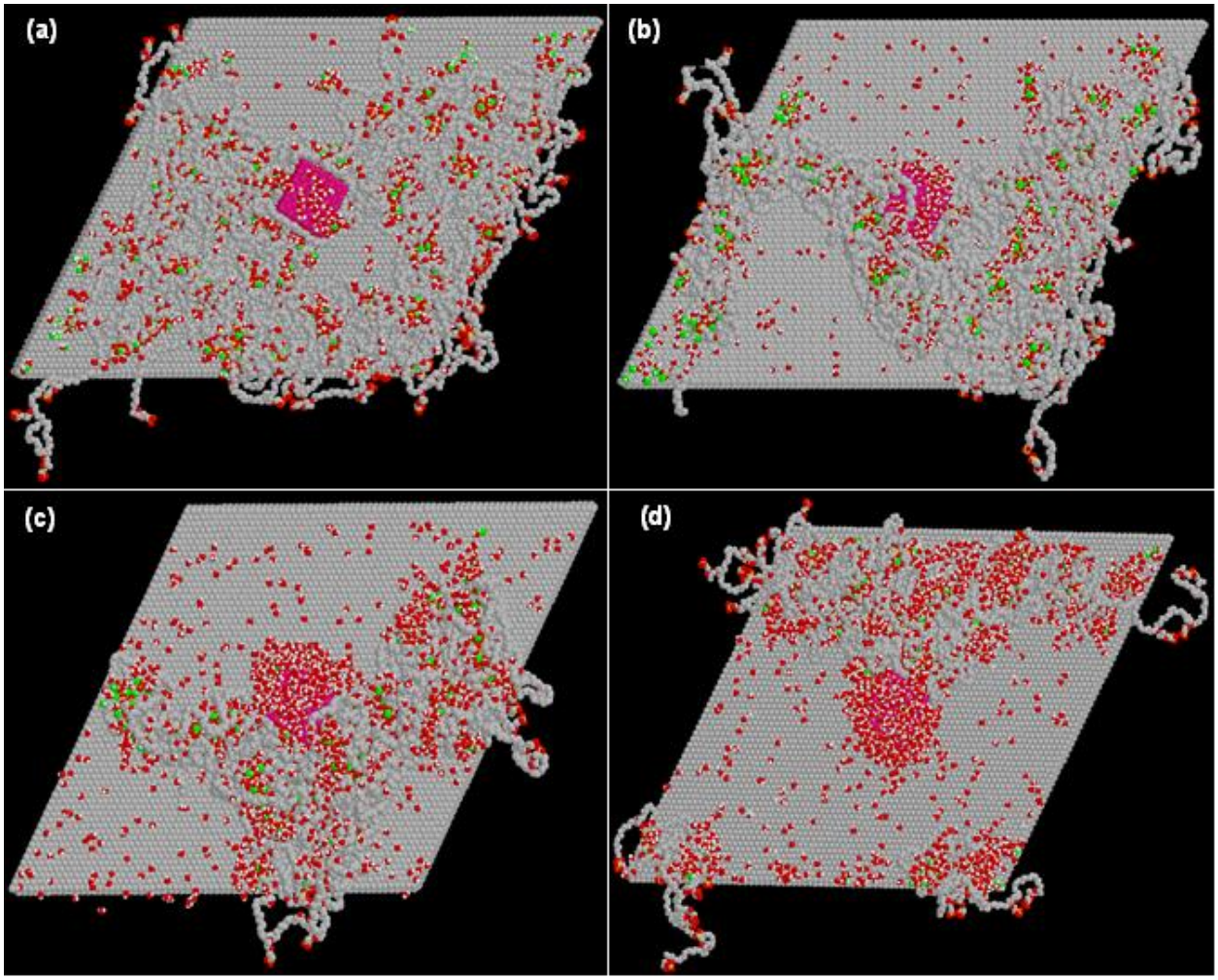

Figure 15 Snapshots of Equilibrated Non-Oxidized Pt/C Systems.

Equilibrated systems contain a 2 nm cubic Pt and different hydration levels at equilibrium distance (0.32 nm). (a) λ =3 (b) λ=6 (c) λ = 9 (d) λ = 15.

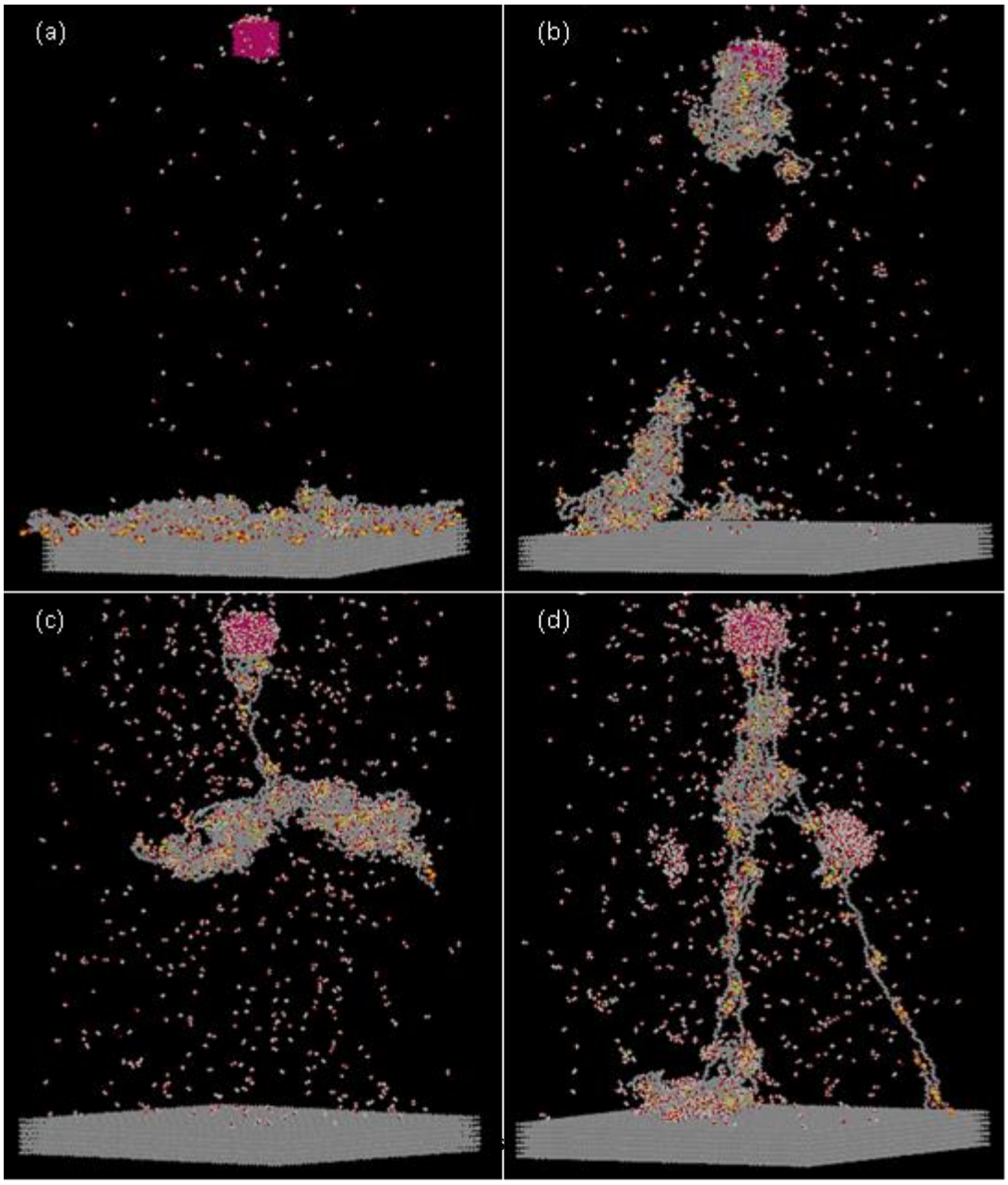

Snapshots of systems contain a 2 nm cubic Pt and different hydration levels at separation distance = 30 nm. (a) λ =3 (b) λ=6 (c) λ = 9 (d) λ = 15

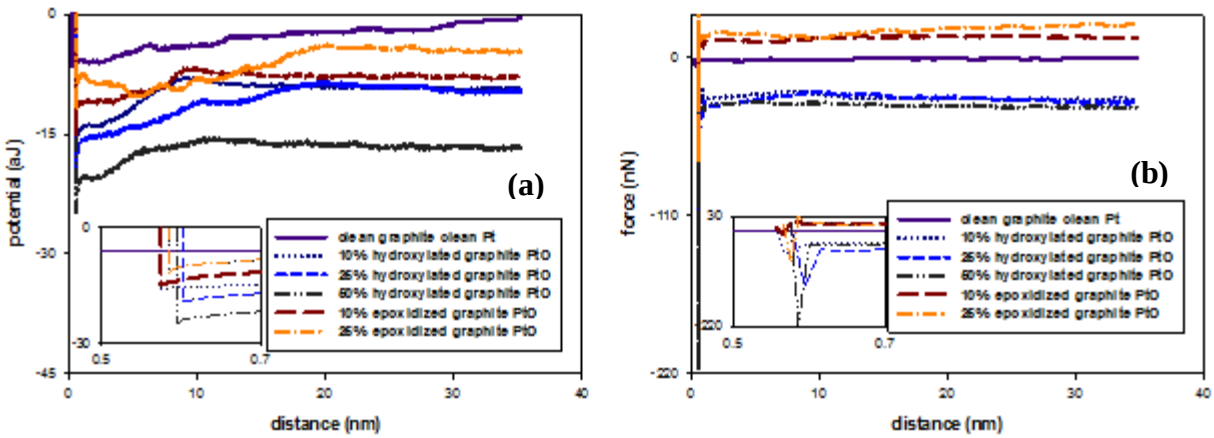

Figure 17 Potential and Force Curves for Oxidized Systems at the hydration level of λ = 3.

Binding energy (a) and adhesion force (b) curves for all surfaces at the hydration level of λ = 3.

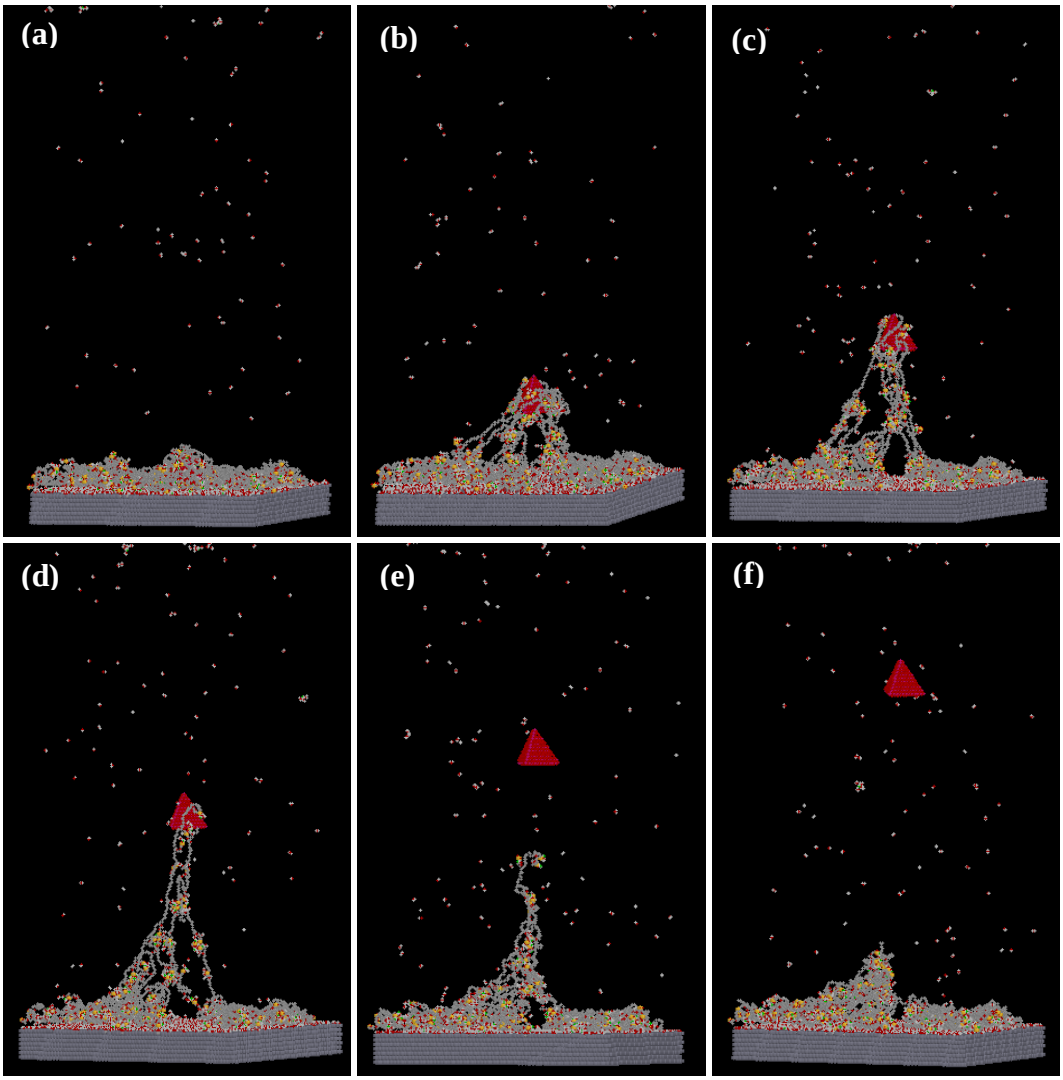

Figure 18 Snapshots Depicting PtO Detachment Process.

Snapshots illustrating the process of PtO detachment from the graphite surface for a system including a 25 % hydroxylated graphite surface at the hydration level of λ=3.

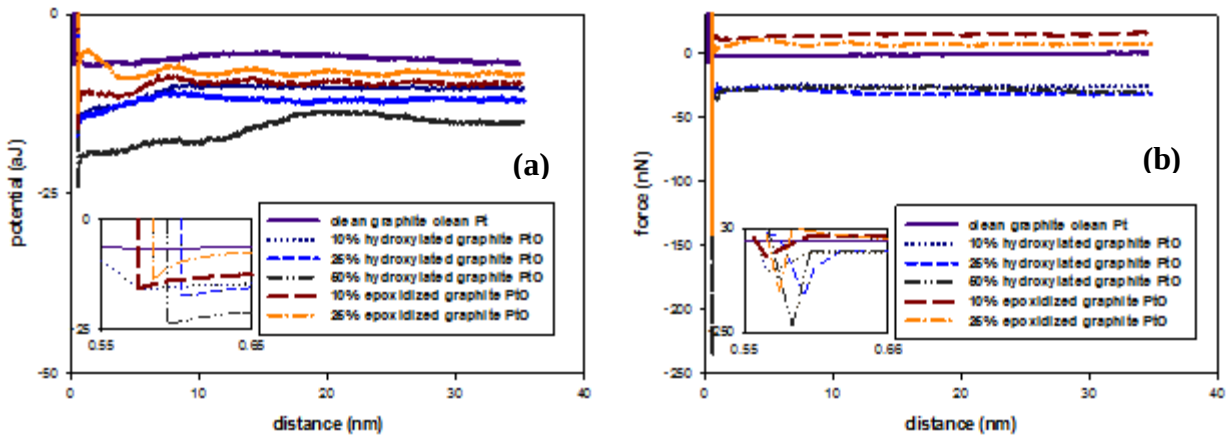

Figure 19 Potential and Force Curves for Oxidized Systems at the hydration level of λ = 9

Binding energy (a) and adhesion force (b) curves for all surfaces at the hydration level of λ = 9.

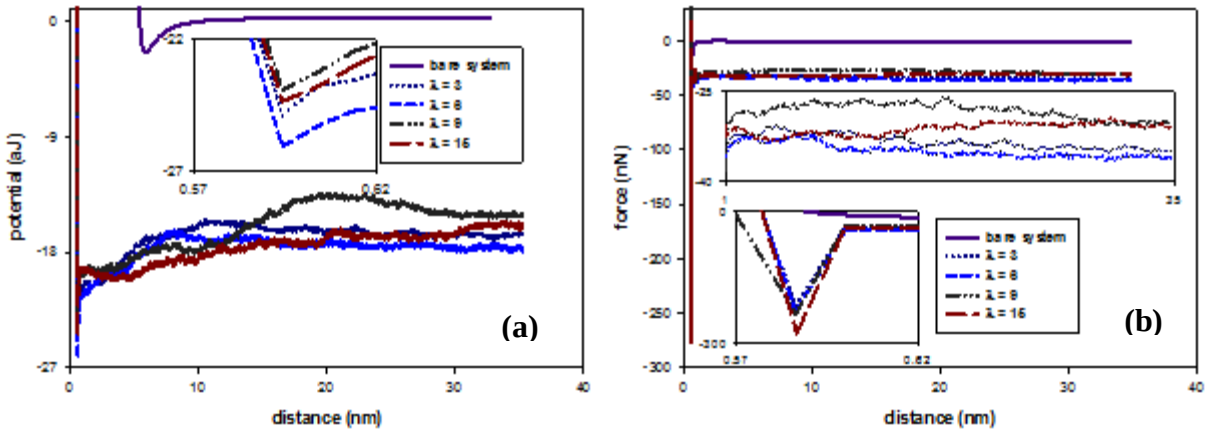

Figure 20 Potential and Force Curves for 50% Hydroxylated Systems.

Binding energy (a) and adhesion force (b) curves for the 50 % hydroxylated surface at hydration levels of λ = 3, 6, 9 and 15

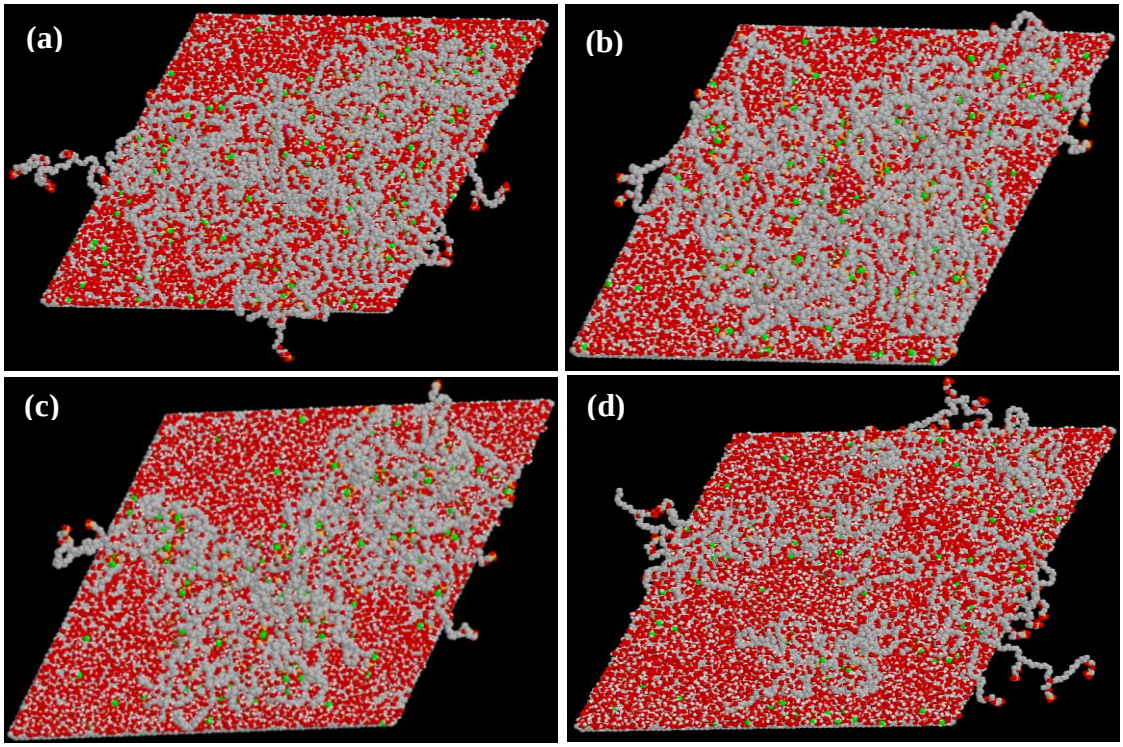

Figure 21 Snapshots of 50% Hydroxylated Systems.

Snapshots of 50 % hydroxylated system at the hydration level of λ = 3, 6, 9 and 15 showing the polymer conformation at the oxidized graphite surface. (a) λ = 3. (b) λ = 6. (c) λ = 9. (d) λ = 15.

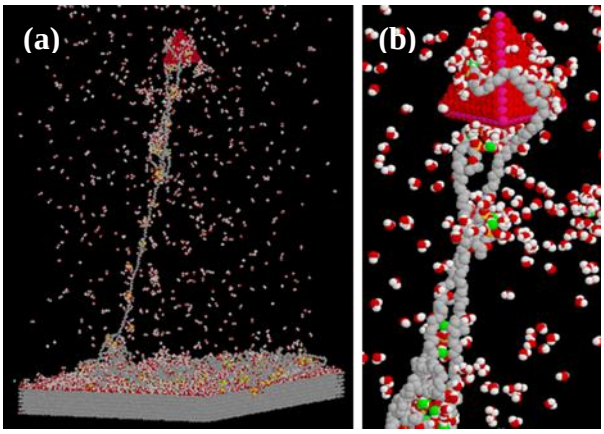

Figure 22 Snapshot of PtO Detachment with Close-up.

Snapshots of 50 % hydroxylated system at the hydration level of λ = 9 during detachment process. (a) full system (b) close-up of the nanoparticle.

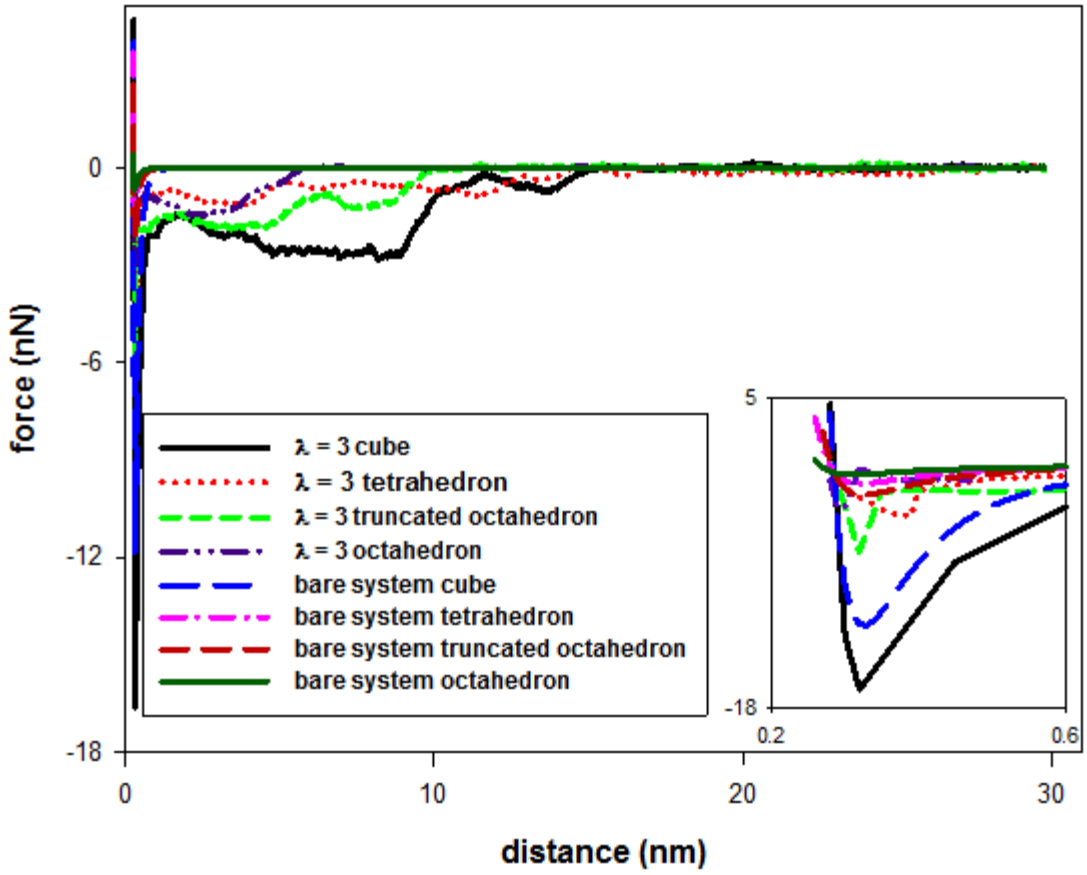

Figure 23 Force Curves of Pt/C systems for Bare and Wet systems (λ = 3).

Force curves for systems contain a 2 nm cubic Pt and different shapes at hydration level of λ = 3.

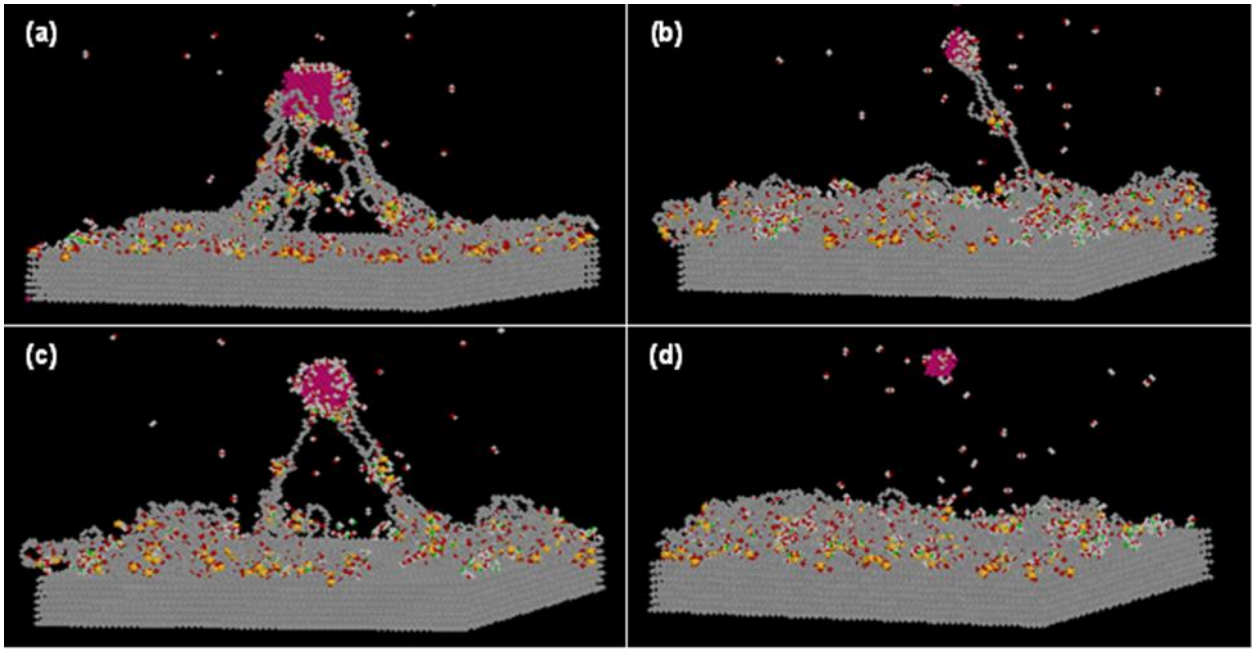

Figure 24 Snapshot of Pt/C systems at the Separation Distance of 7.5 nm.

Snapshots of systems contain a 2 nm Pt nanoparticle at the hydration level of λ = 3 at separation distance = 7.5 nm. (a) cube (b) tetrahedron (c) truncated octahedron (d) octahedron.

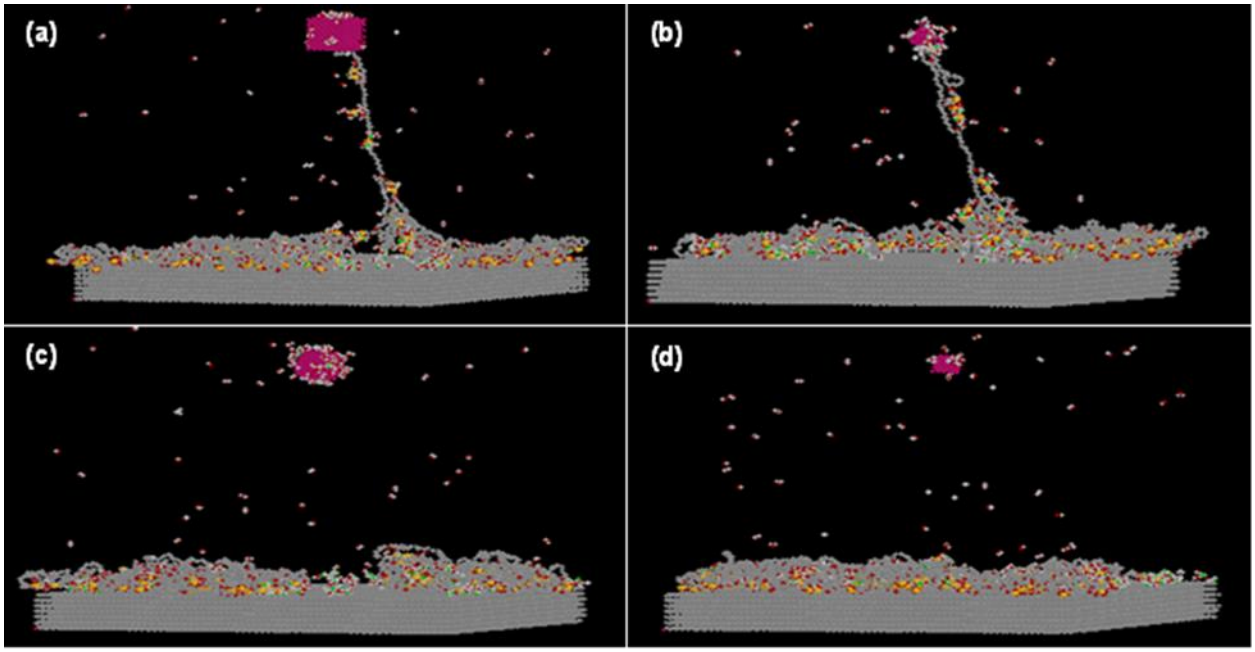

Figure 25 Snapshots of Pt/C systems at the Separation Distance of 12 nm.

Snapshots of systems contain a 2 nm Pt at the hydration level of $\lambda = 3$ at separation distance = 12 nm. (a) cube (b) tetrahedron (c) truncated octahedron (d) octahedron.

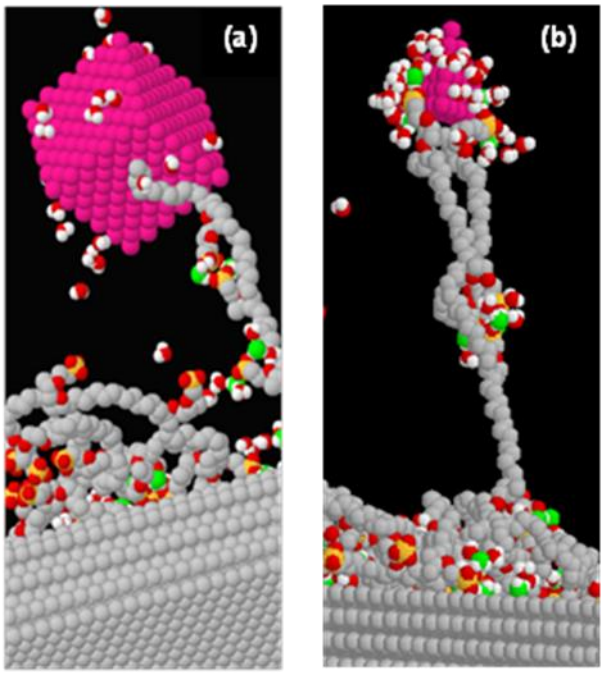

Figure 26 Snapshot of Pt detachment with close-up.

Close-up of systems contain a 2 nm Pt at the hydration level of $\lambda = 3$ at separation distance = 12 nm. (a) cube (b) tetrahedron.

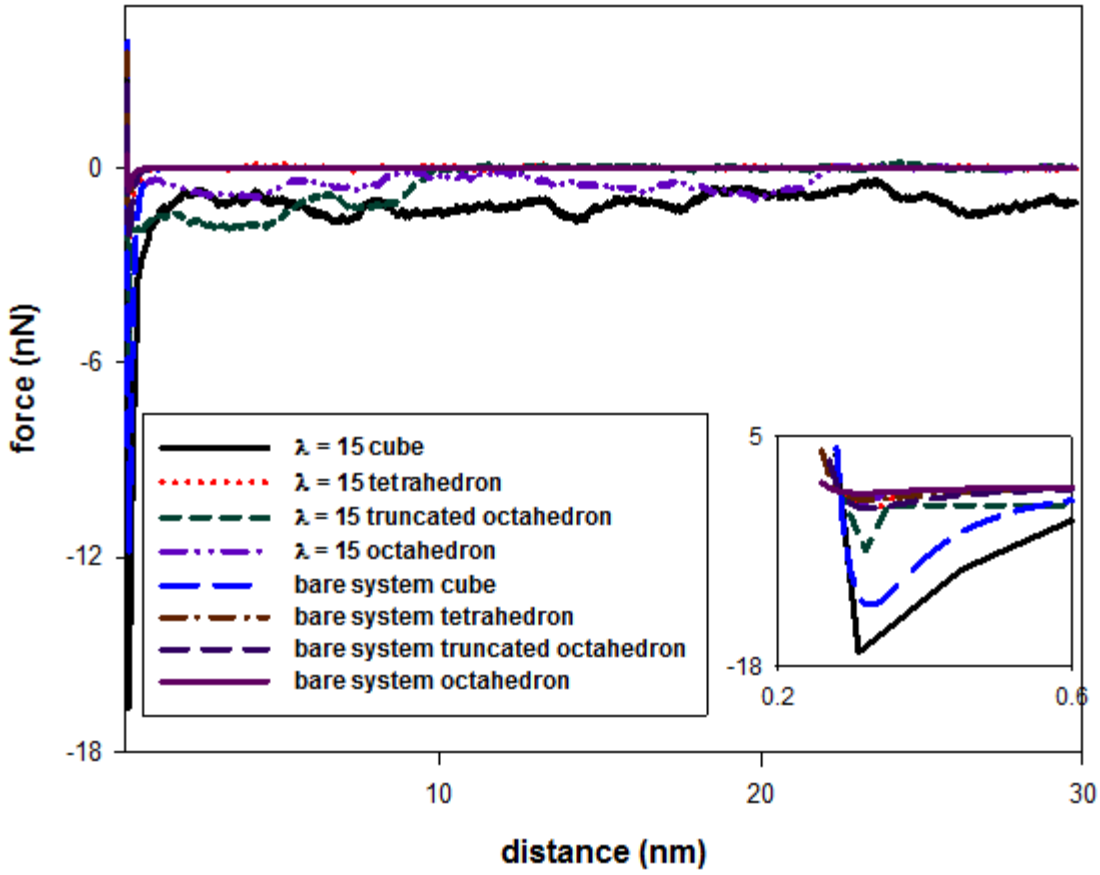

Figure 27 Force Curves for Pt/C Systems for Bare and Wet Systems (λ = 9).

Force curves for systems contain a 2 nm cubic Pt and different shapes at the hydration level λ = 15.

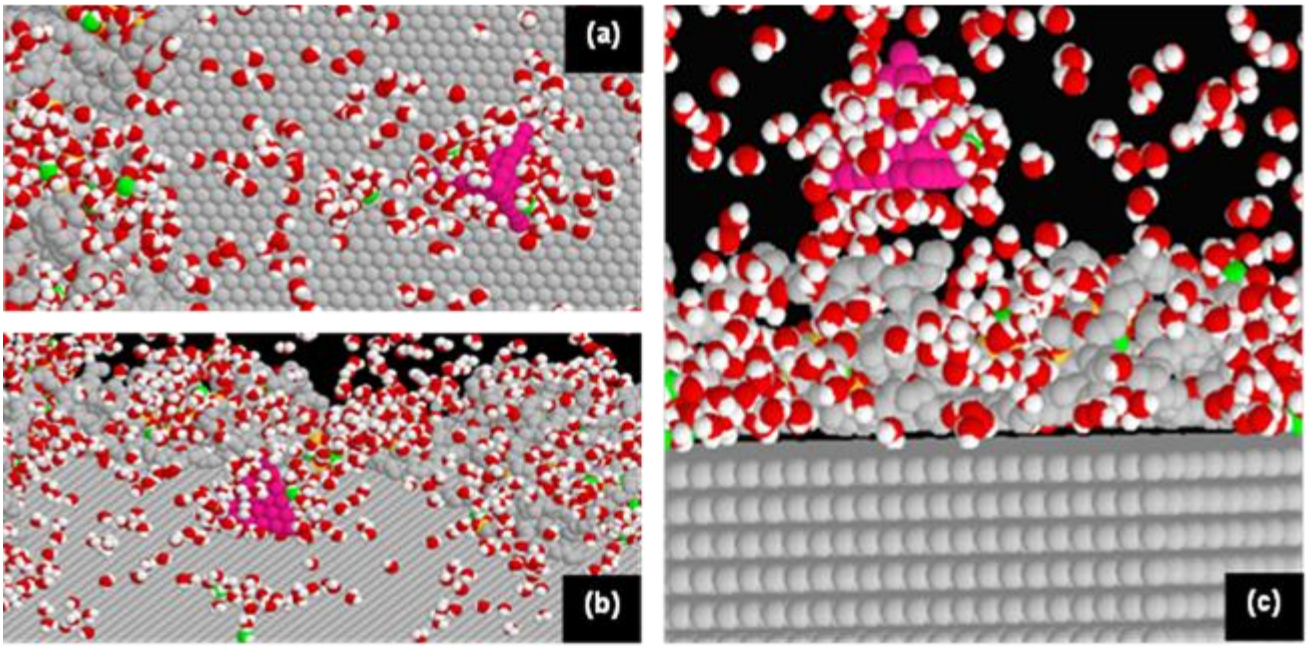

Snapshots of the system contains a 2 nm tetrahedral Pt at the hydration level of λ = 15. (a) top view of the system at the equilibrium distance (0.32 nm) (b) side view of the system at the equilibrium distance (0.32 nm) (c) side view of the system at a separation distance of 1.5 nm.

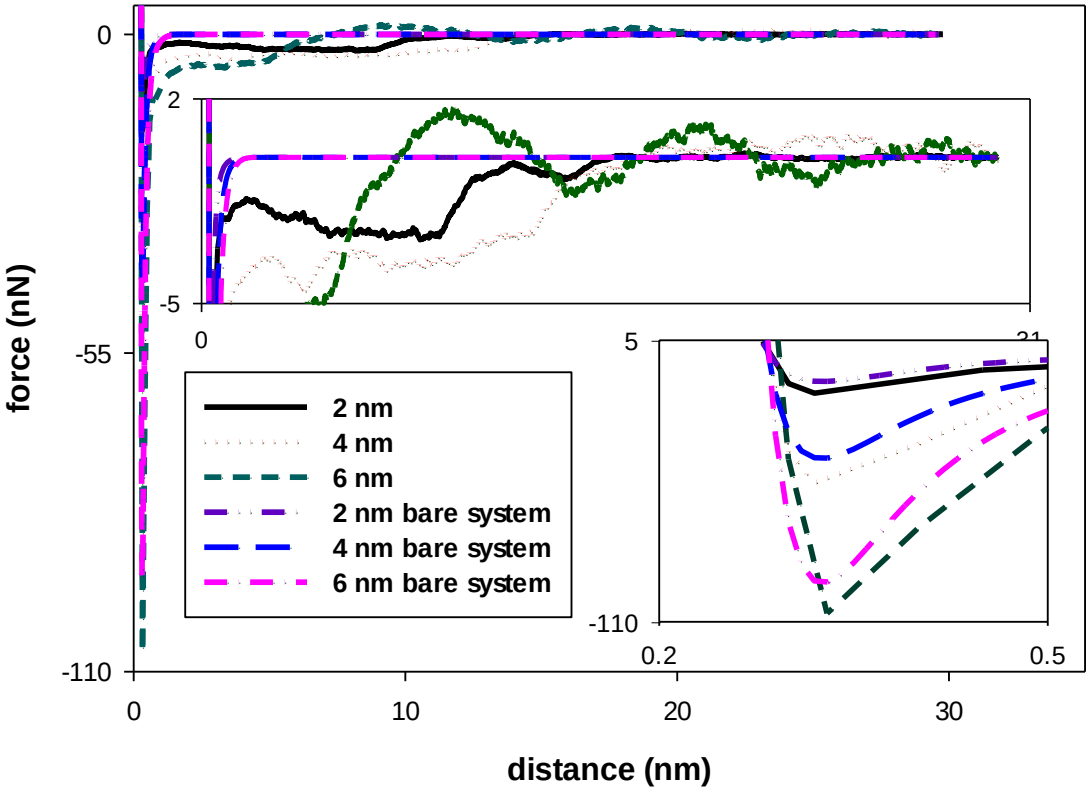

Figure 29 Force Curves for Cubic Pt/C Systems at the Hydration Level of λ = 3.

Force curves of systems contain a cubic Pt of various sizes at the hydration level of λ = 3.

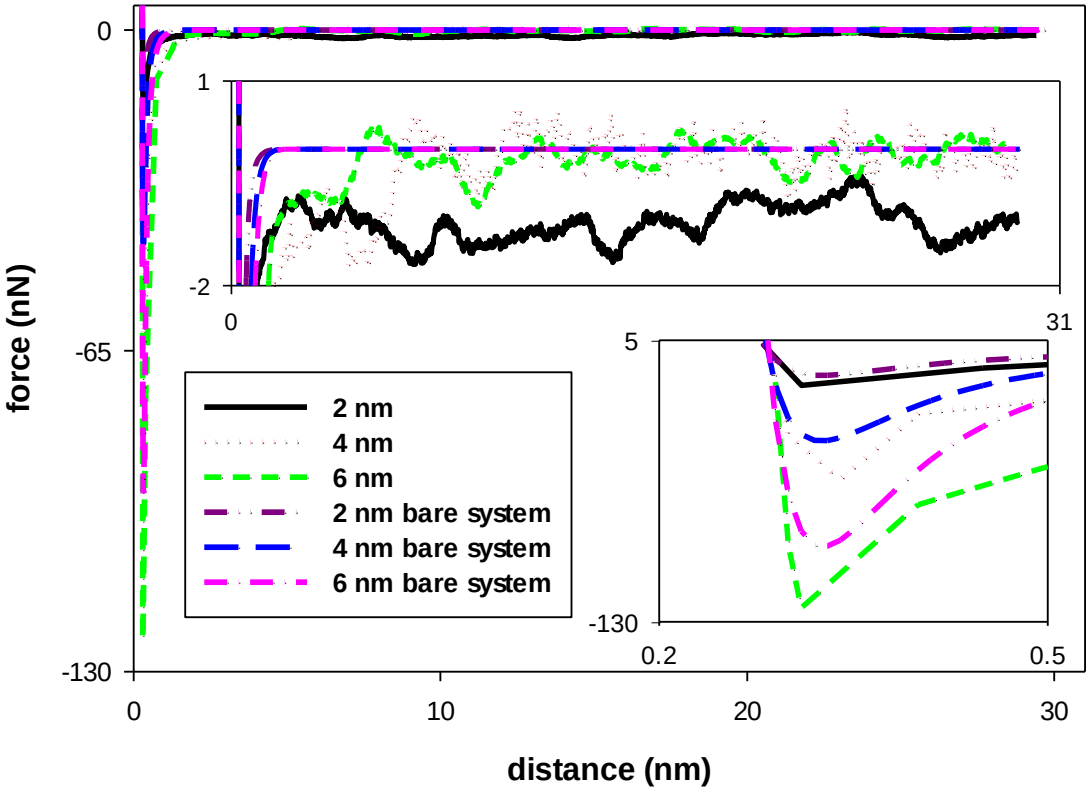

Figure 30 Force Curves for Cubic Pt/C Systems at the Hydration Level of λ = 15

Force curves of systems contain a cubic Pt of various sizes at the hydration level of λ = 15.

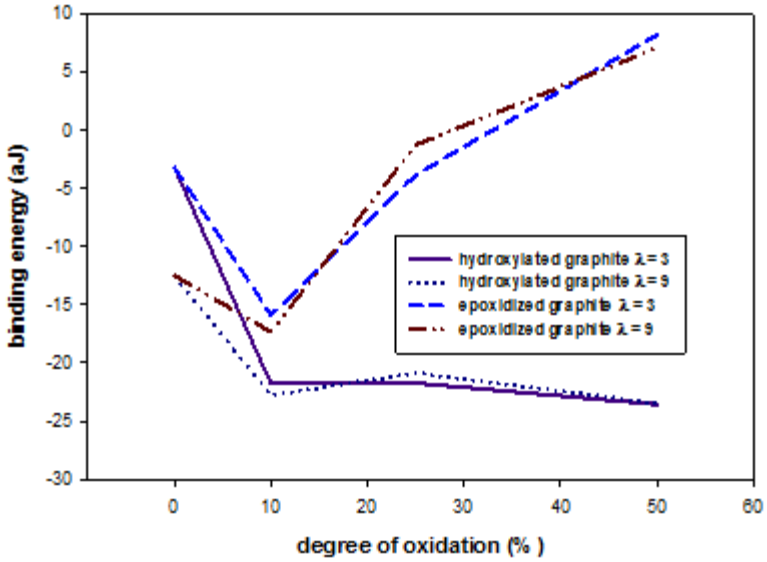

Figure 31 Binding Energies Between Ionomer Film and Oxidized Carbon Support.

Binding energy between the hydrated Nafion membrane and the oxidized rigid system (oxidized graphite and PtO) at different oxidation levels of graphite.

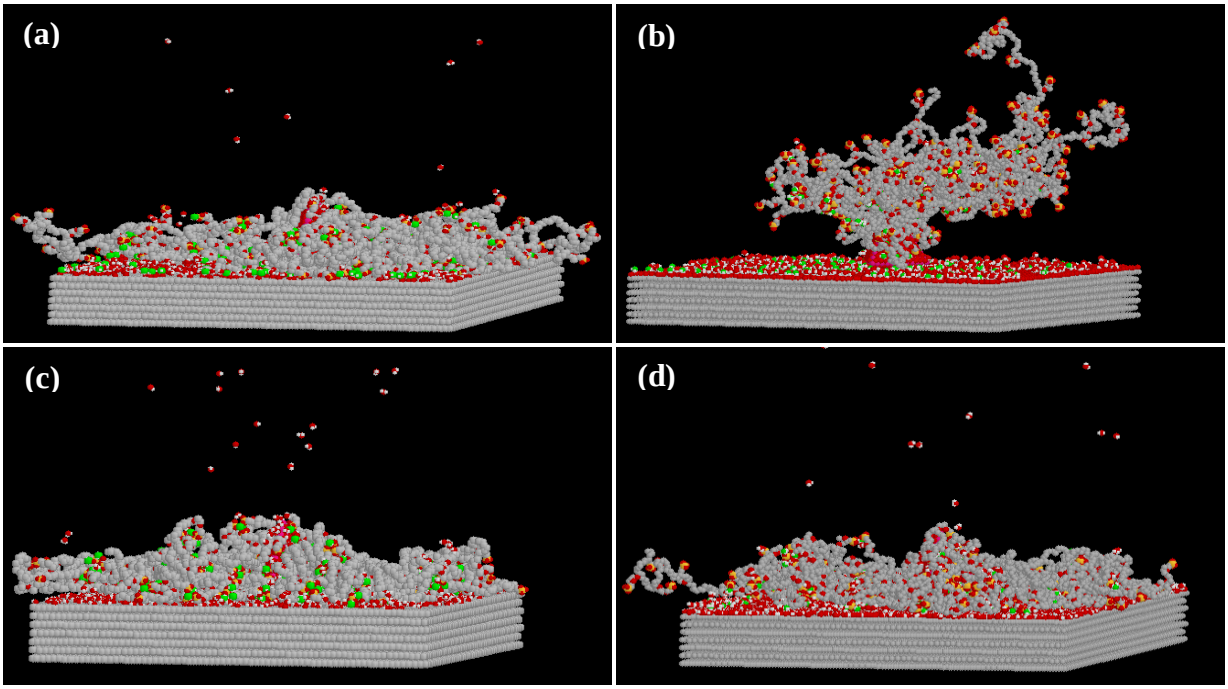

Figure 32 Ionomer Film Conformations on the Oxidized Carbon Support.

Snapshot showing the polymer conformation at the hydration level of $\lambda = 3$ for both epoxidized and hydroxylated graphite surface at oxidation rate 10% and 50%. (a) 10% epoxidized system. (b) 50% epoxidized system. (c) 10% hydroxylated system. (d) 50% hydroxylated system.

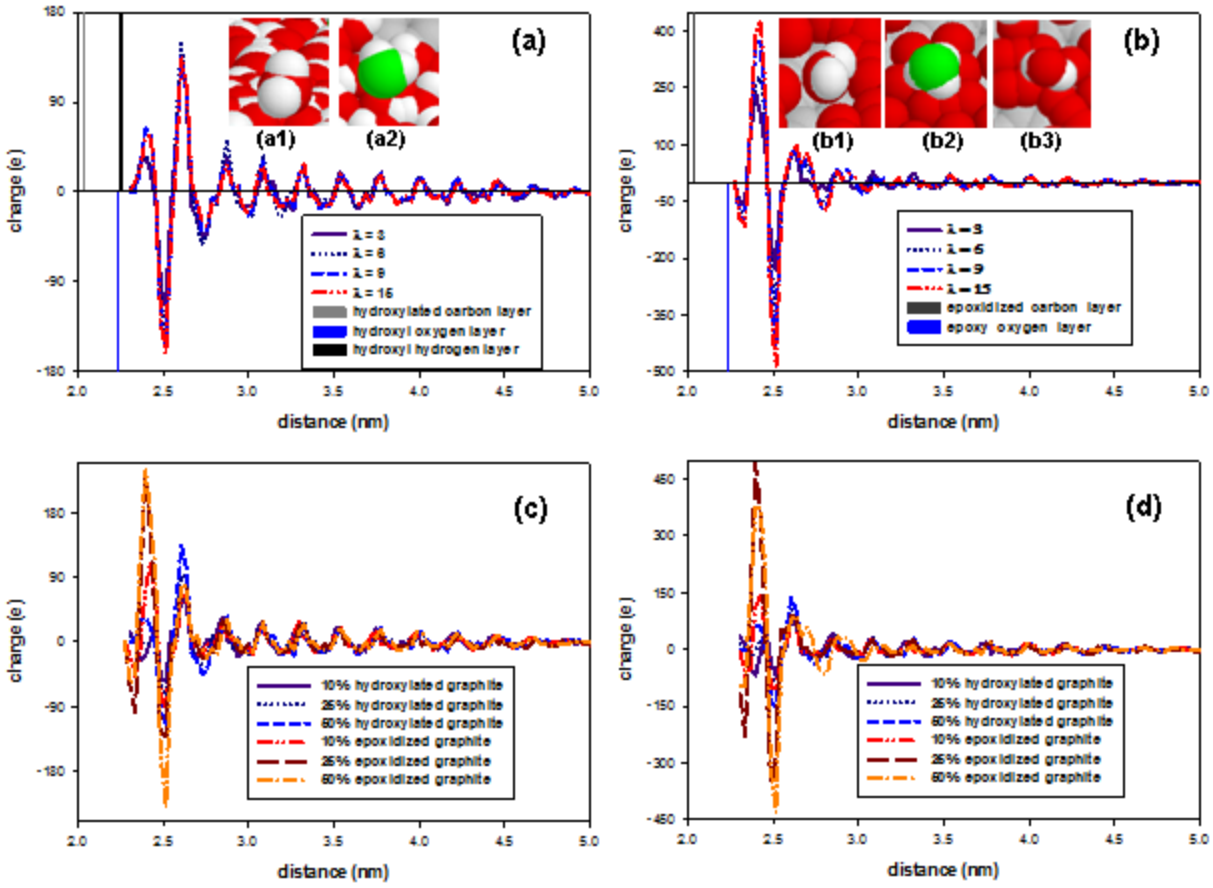

System charge distribution curves in the z-direction starting from the top carbon layer surface. (a) charge distribution curves of 50% hydroxylated graphite surface at different humidity levels with inserted snapshots illustrating the water and hydronium ions orientation on the OG surface. (b) charge distribution curves of 50% epoxidized graphite surface at different humidity levels with inserted snapshots illustrating the water and hydronium ions orientation on the OG surface. (c) charge distribution curves for all the oxidized systems at the hydration level of $\lambda = 3$. (c) charge distribution curves for all the oxidized systems at the hydration level of $\lambda = 9$.

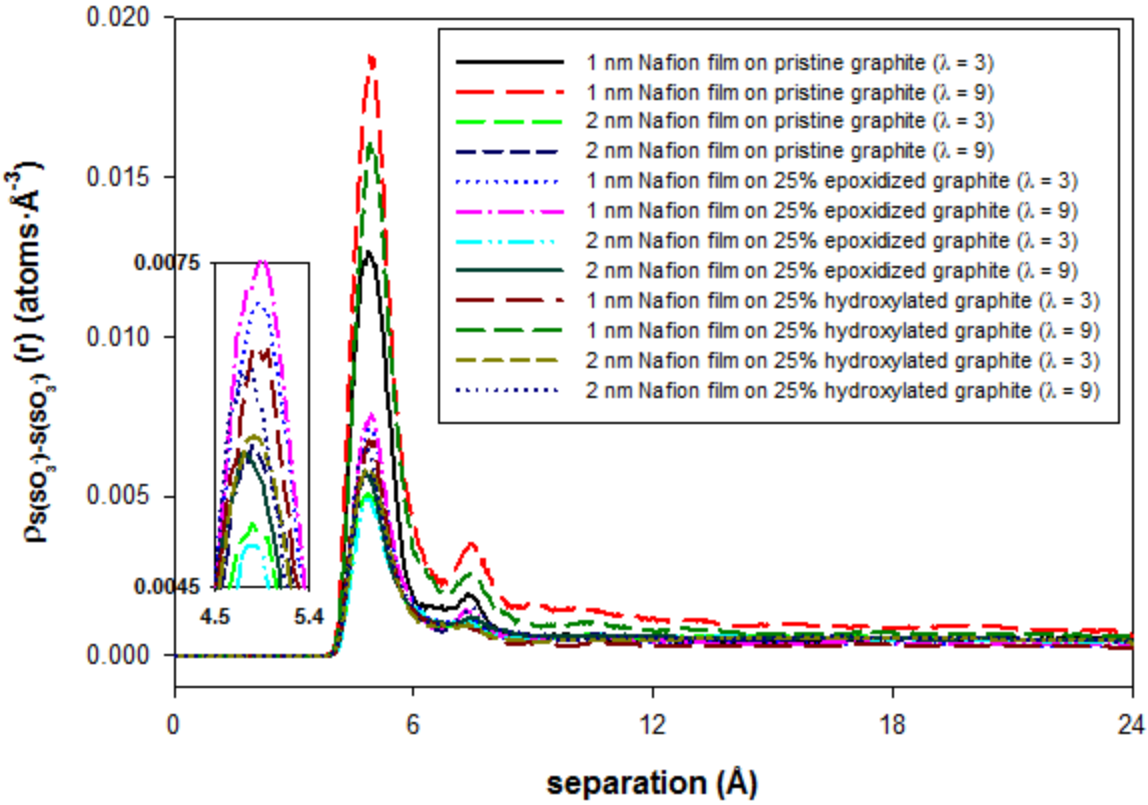

Radial density functions of sulfur-sulfur clusters for the systems with no catalyst nanoparticles.

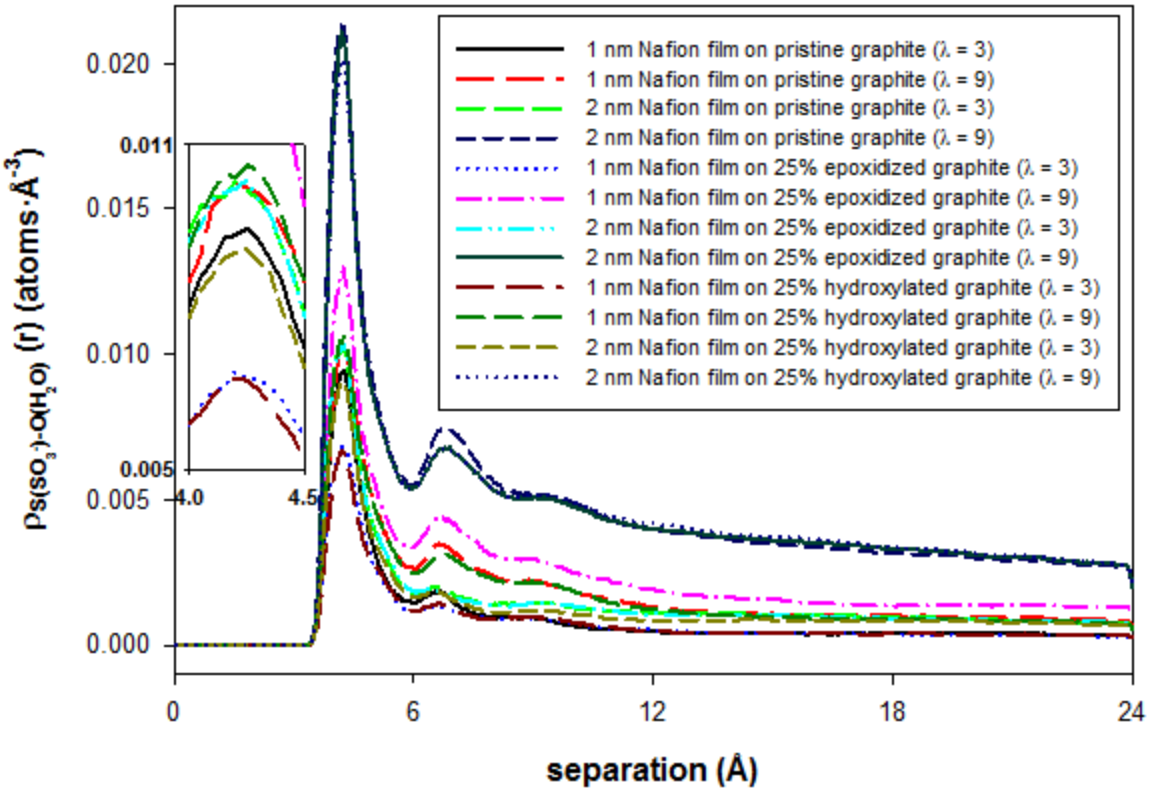

Figure 35 Radial Density Functions of Sulfur-Water for No Catalyst Systems.

Radial density functions of sulfur-water clusters for the systems with no catalyst nanoparticles.

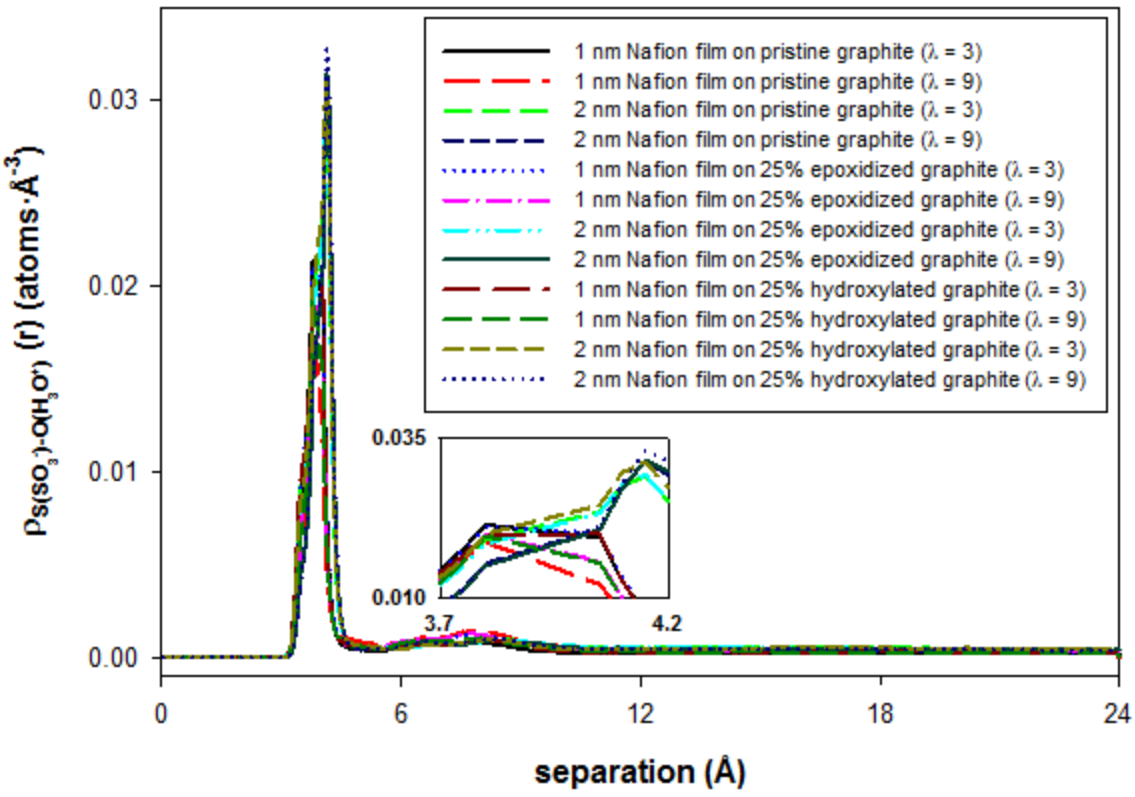

Figure 36 Radial Density Functions of Sulfur-Hydronium Ions for No Catalyst Systems

Radial density functions of sulfur-hydronium ions clusters for the systems with no catalyst nanoparticles.

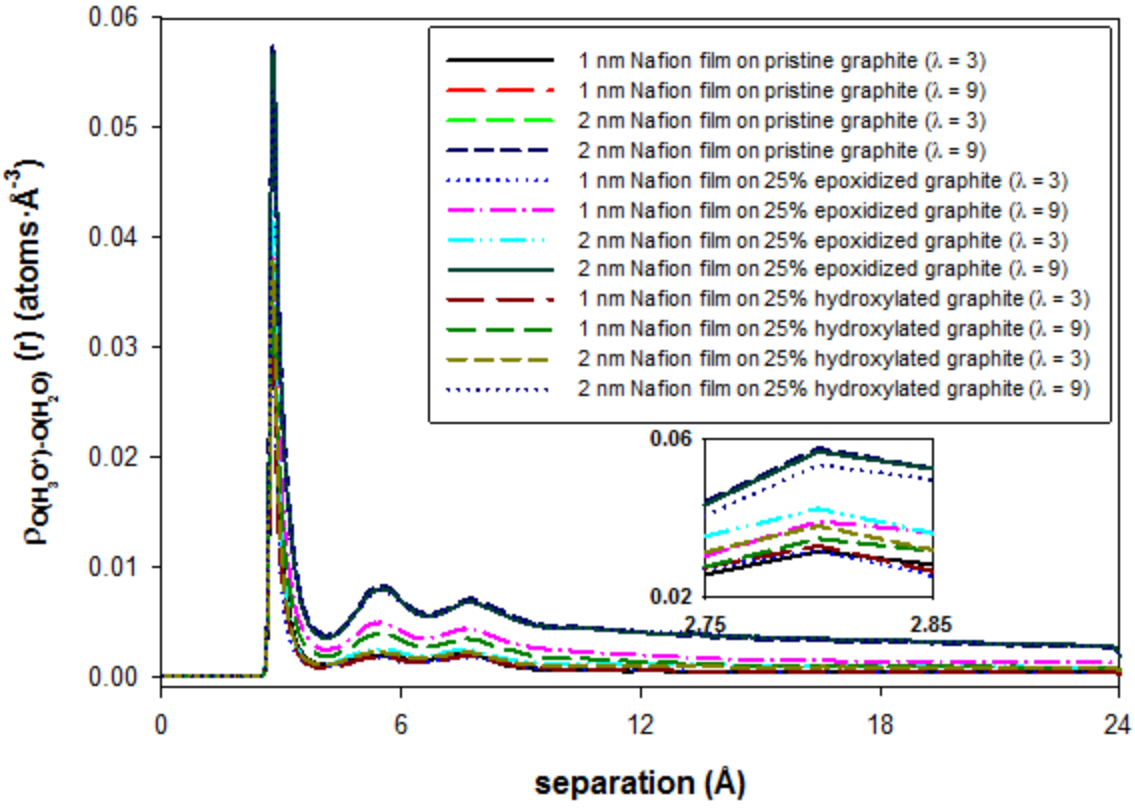

Figure 37 Radial Density Functions of Hydronium Ion-Water for No Catalyst Systems

Radial density functions of hydronium ion-water clusters for the systems with no catalyst nanoparticles.

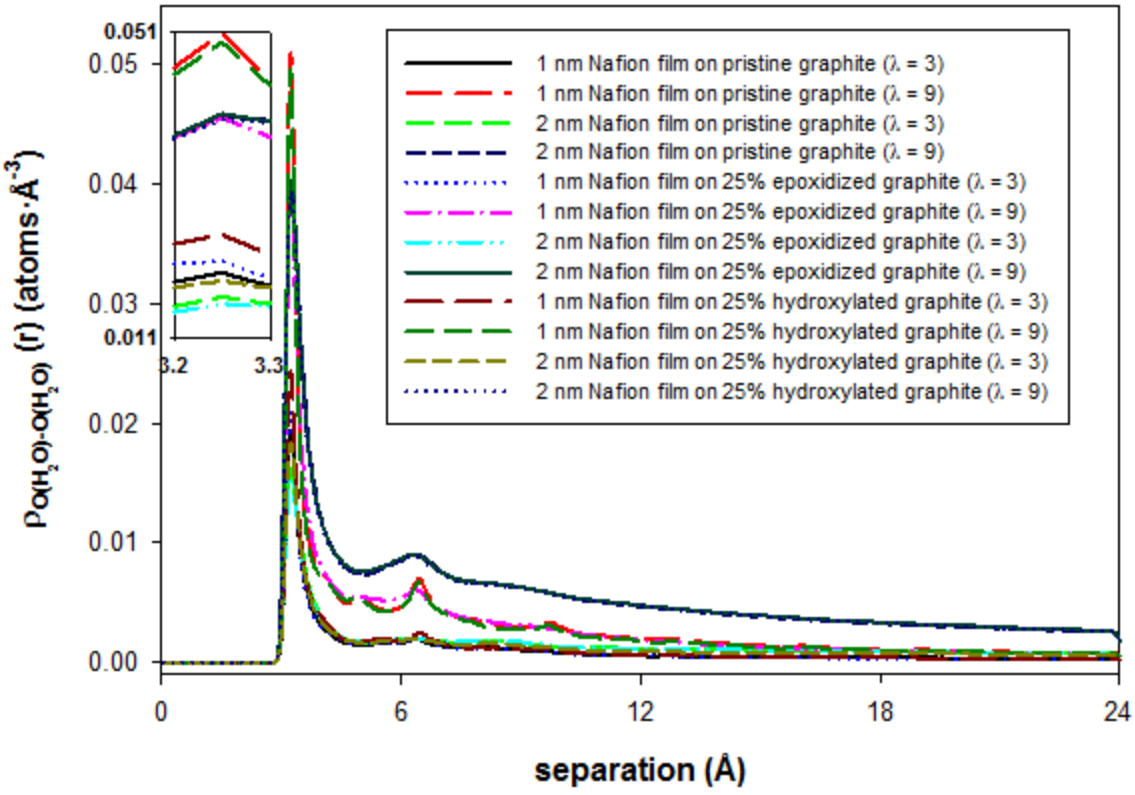

Figure 38 Radial Density Functions of Water-Water for No Catalyst Systems

Radial density functions of water-water clusters for the systems with no catalyst nanoparticles.

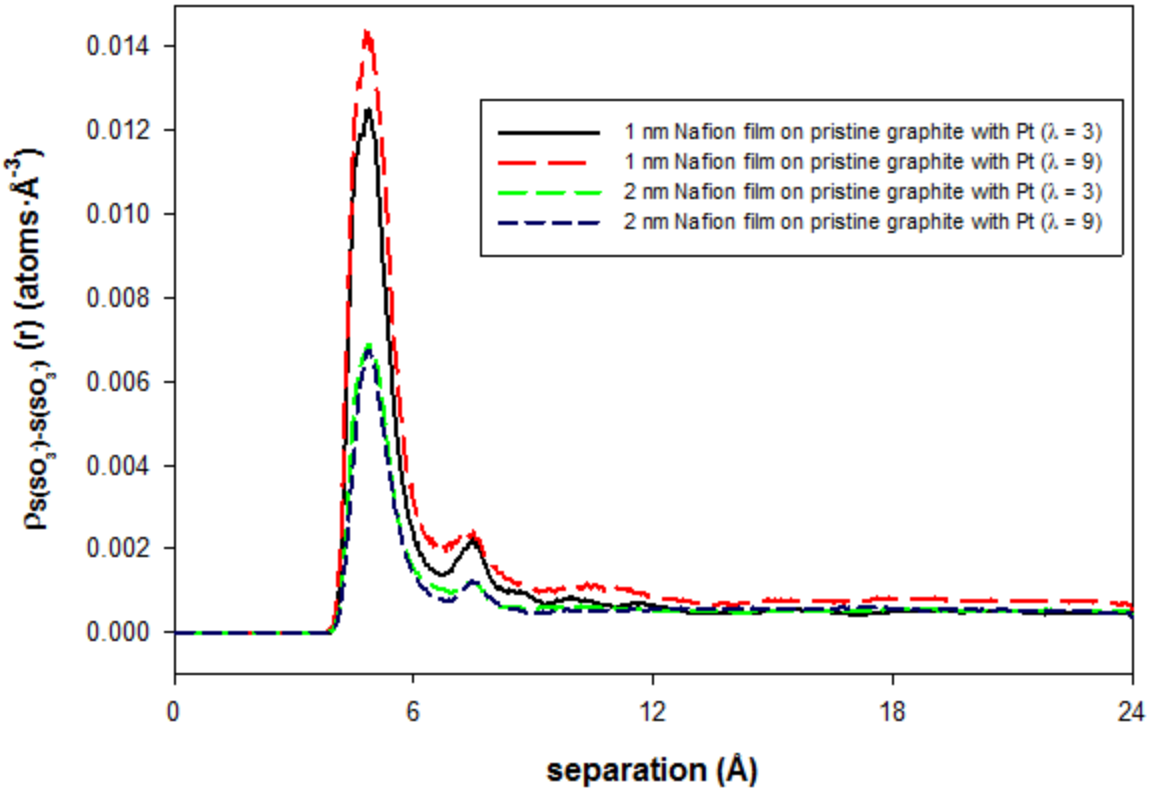

Figure 39 Radial Density Functions of Sulfur-Sulfur for Pt Catalyst Systems

Radial density functions of sulfur-sulfur clusters for the systems with Pt catalyst nanoparticles.

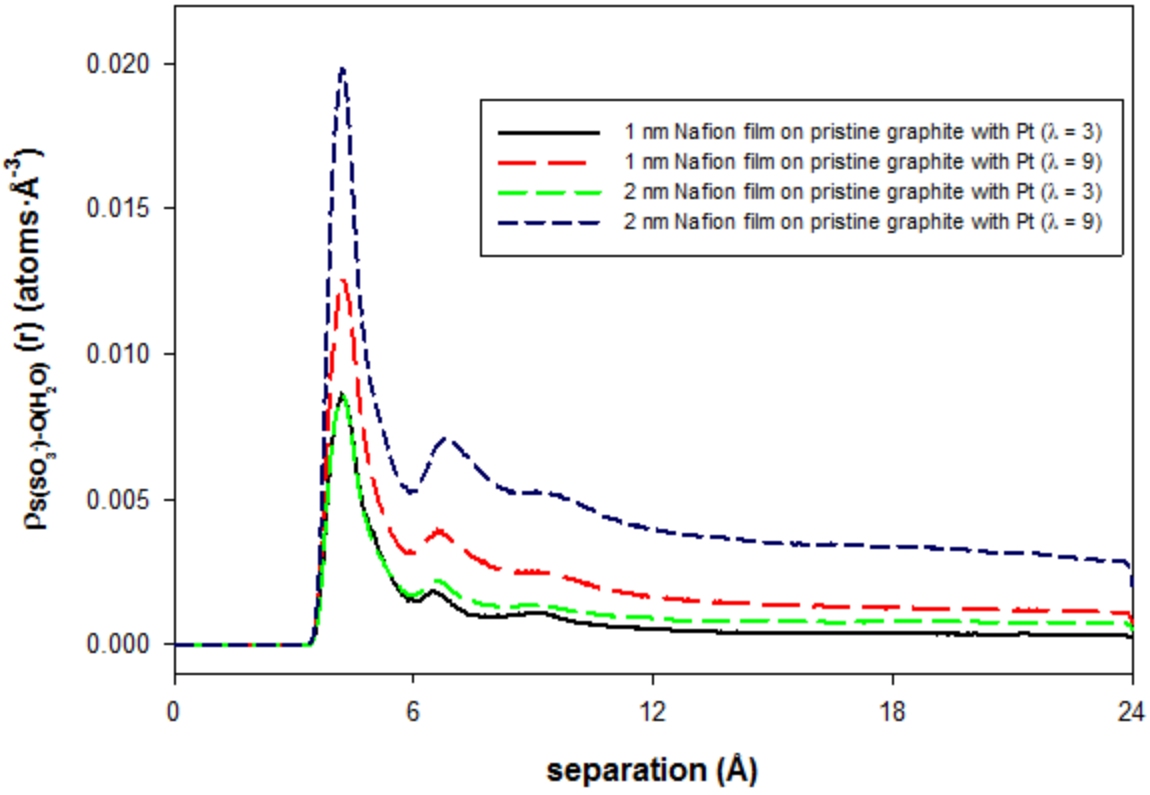

Figure 40 Radial Density Functions of Sulfur-Water for Pt Catalyst Systems

Radial density functions of sulfur-water clusters for the systems with Pt catalyst nanoparticles.

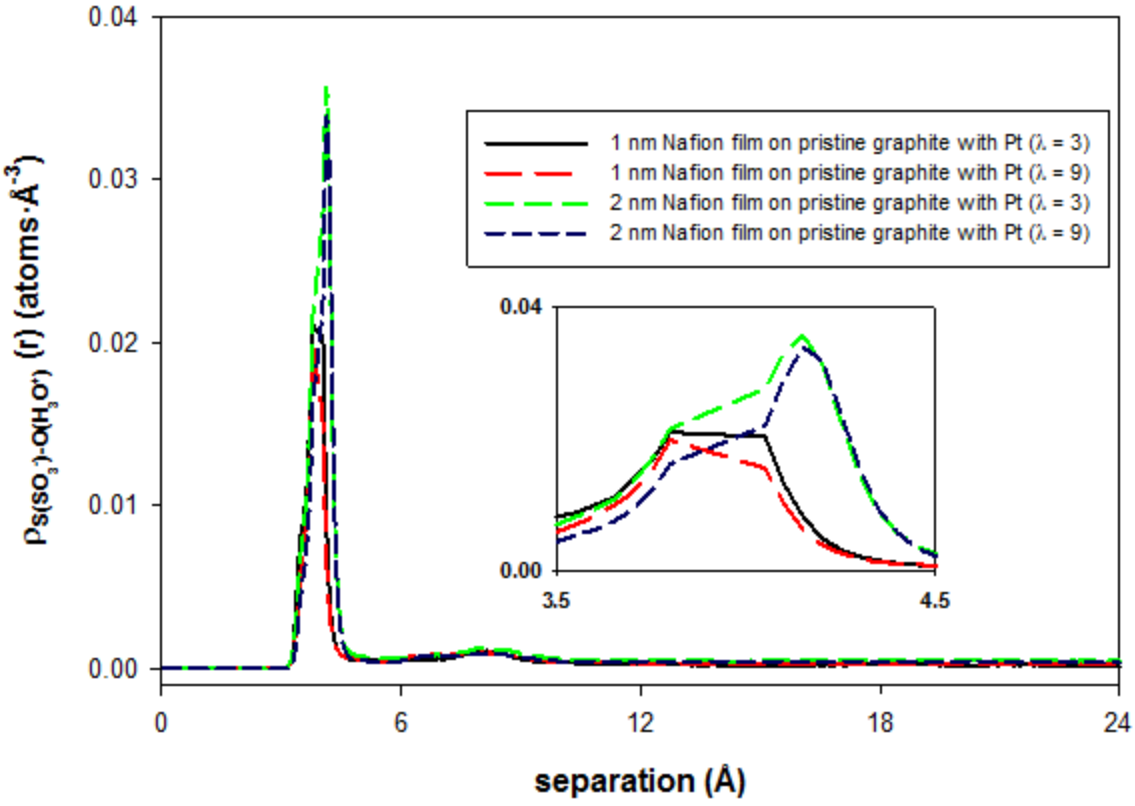

Figure 41 Radial Density Functions of Sulfur-Hydronium Ions for Pt Catalyst Systems

Radial density functions of sulfur-hydronium ions clusters for the systems with Pt catalyst nanoparticles.

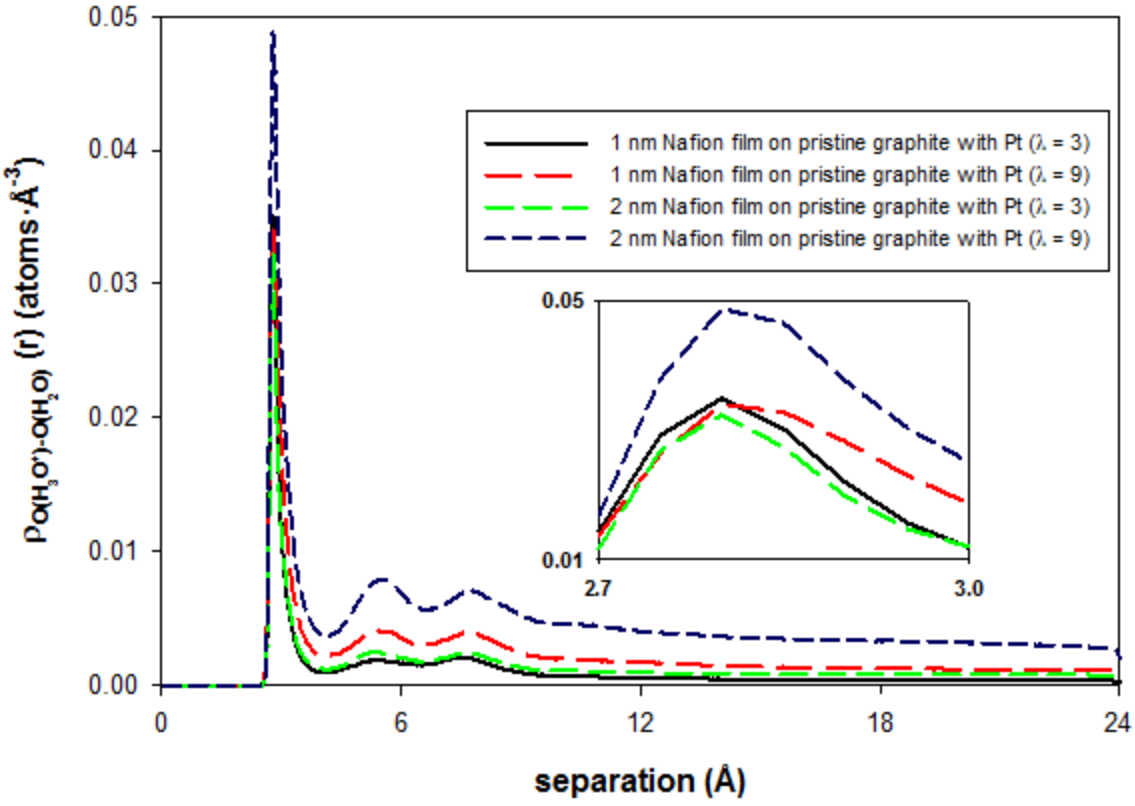

Figure 42 Radial Density Functions of Hydronium Ion-Water for Pt Catalyst Systems

Radial density functions of hydronium ion-water clusters for the systems with Pt catalyst nanoparticles.

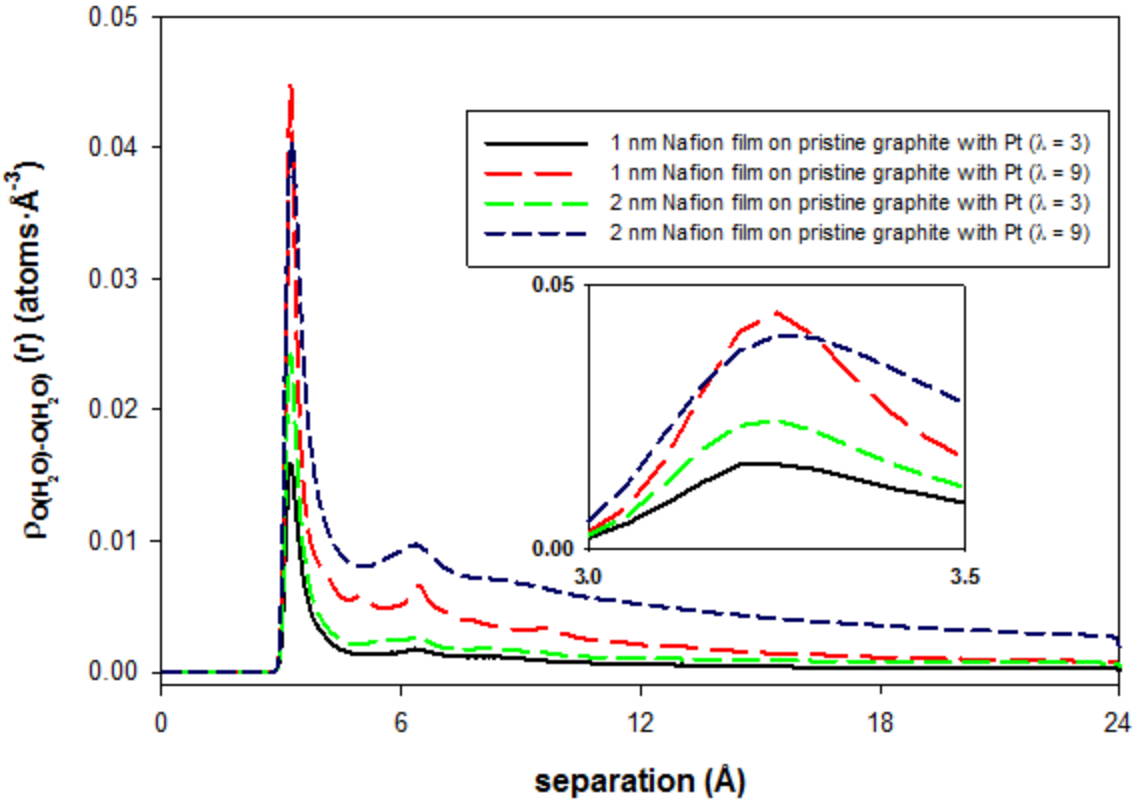

Figure 43 Radial Density Functions of Water-Water for Pt Catalyst Systems

Radial density functions of water-water clusters for the systems with Pt catalyst nanoparticles.

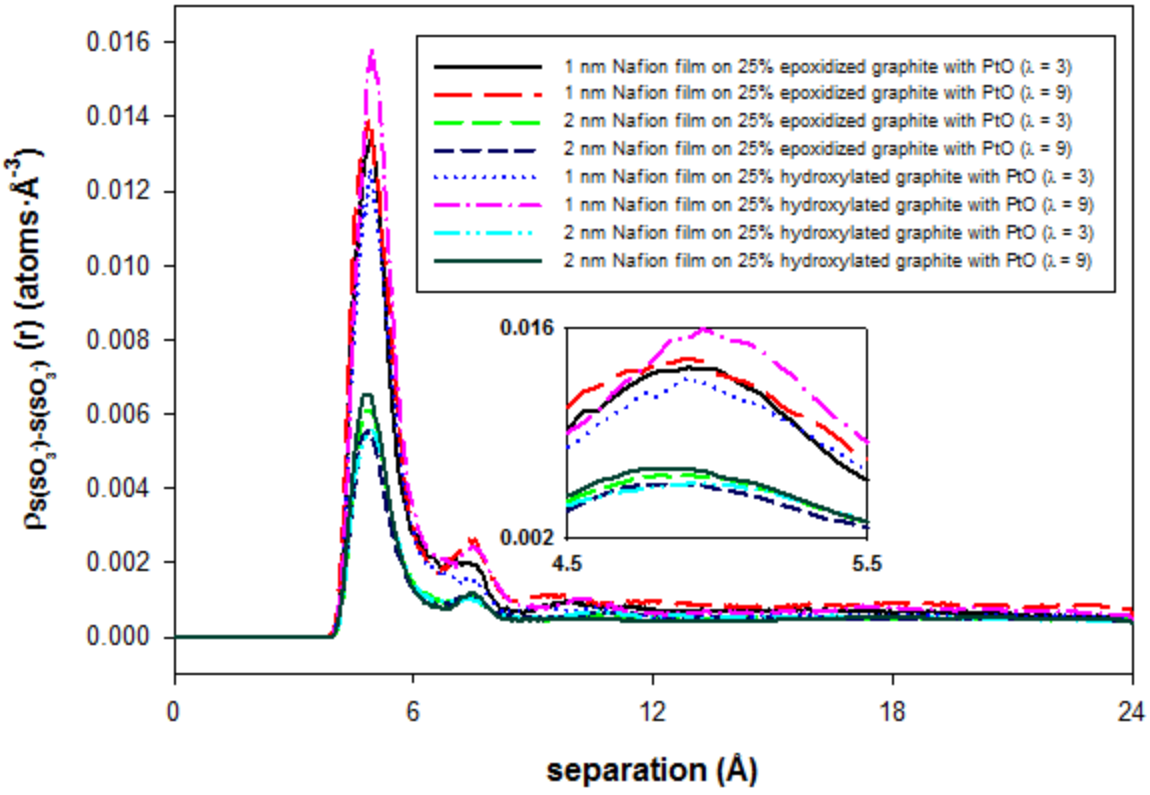

Figure 44 Radial Density Functions of Sulfur-Sulfur for PtO Catalyst Systems

Radial density functions of sulfur-sulfur clusters for the systems with PtO catalyst nanoparticles.

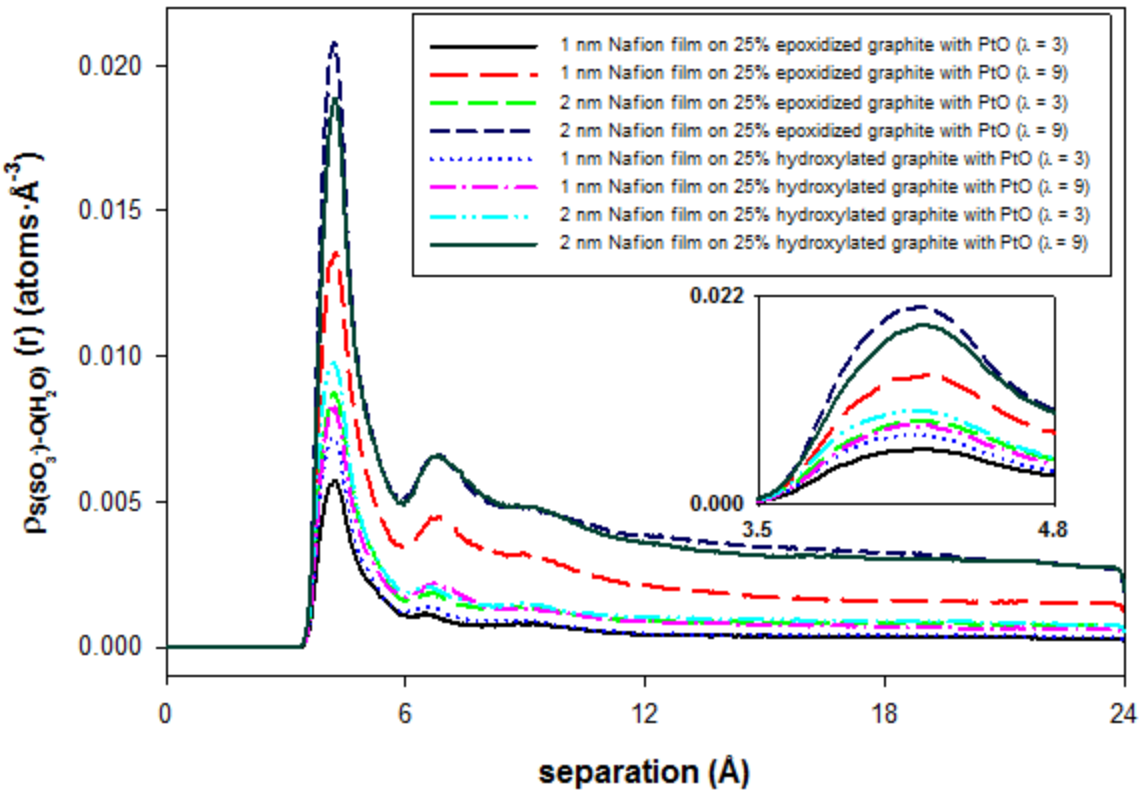

Figure 45 Radial Density Functions of Sulfur-Water for PtO Catalyst Systems

Radial density functions of sulfur-water clusters for the systems with PtO catalyst nanoparticles.

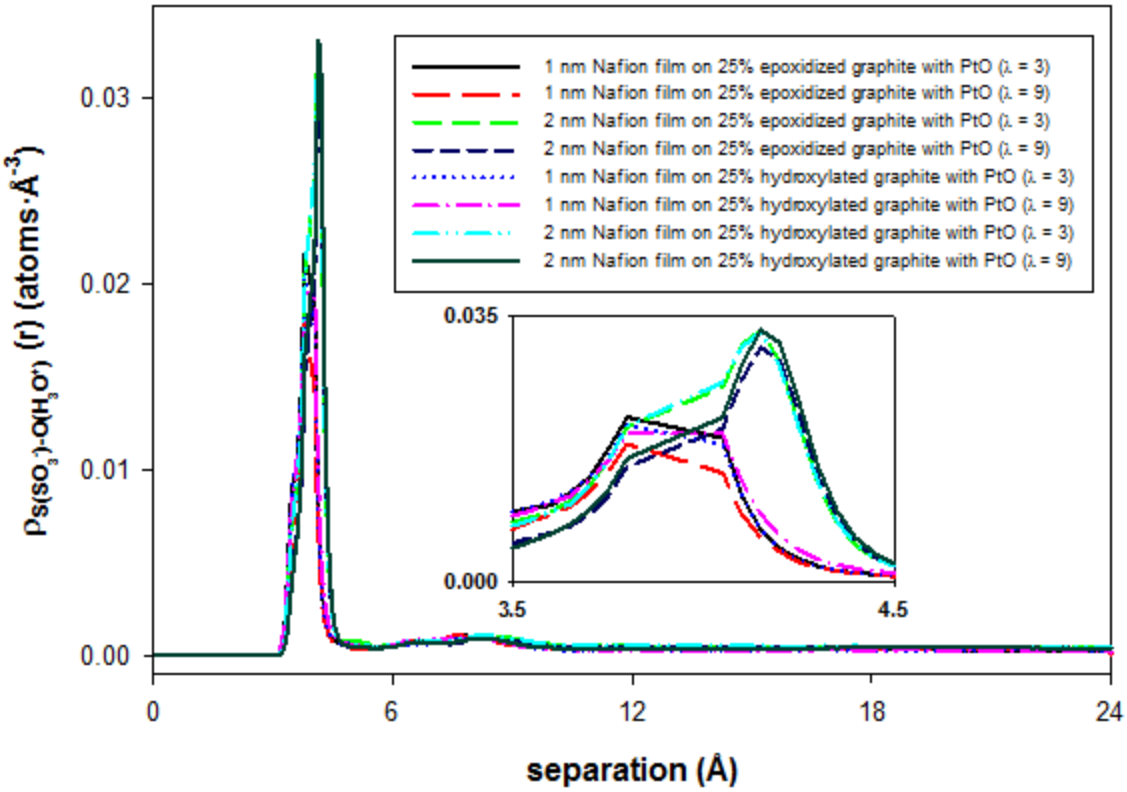

Figure 46 Radial Density Functions of Sulfur-Hydronium Ions for PtO Catalyst Systems

Radial density functions of sulfur-hydronium ions clusters for the systems with PtO catalyst nanoparticles.

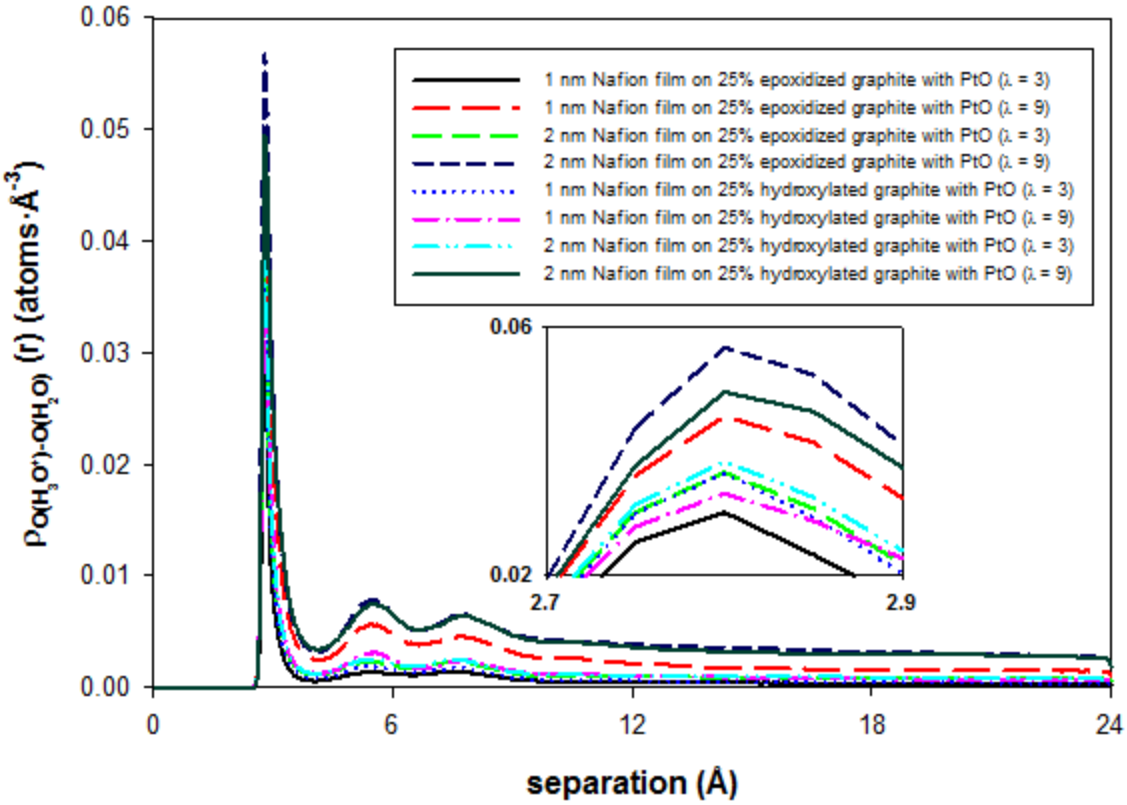

Figure 47 Radial Density Functions of Hydronium Ion-Water for PtO Catalyst Systems

Radial density functions of hydronium ion-water clusters for the systems with PtO catalyst nanoparticles.

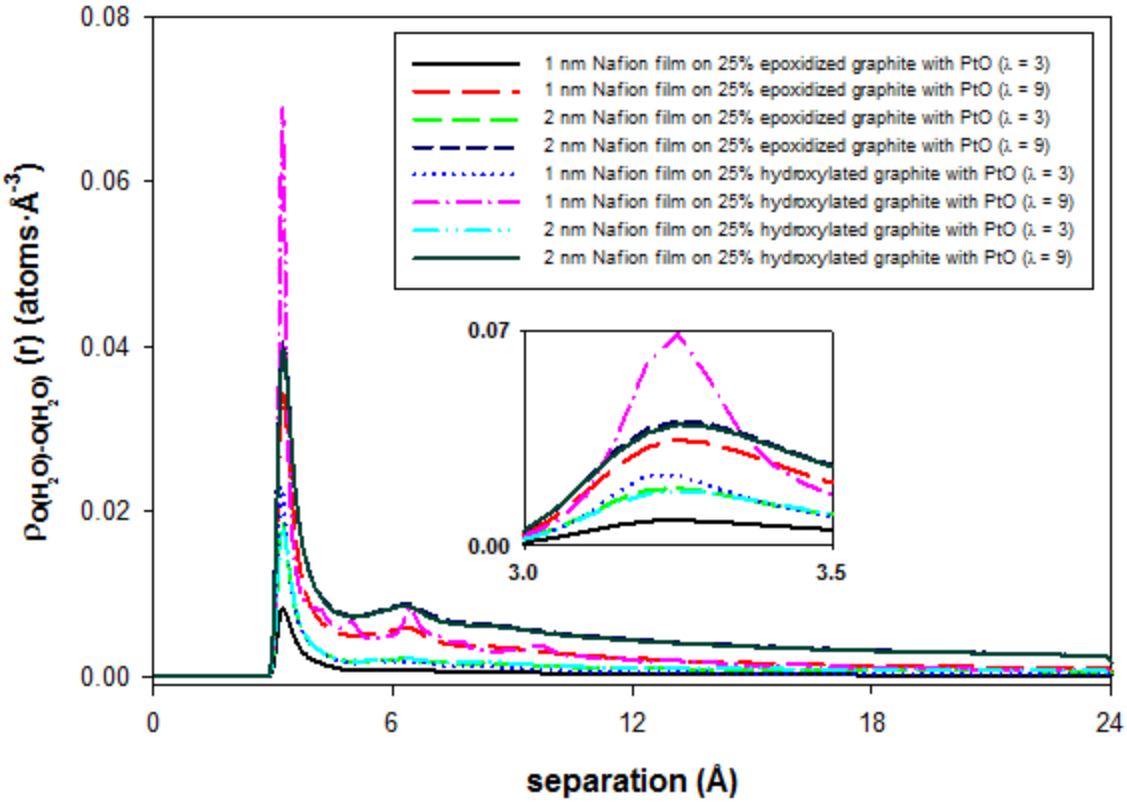

Figure 48 Radial Density Functions of Water-Water for PtO Catalyst Systems

Radial density functions of water-water clusters for the systems with PtO catalyst nanoparticles.

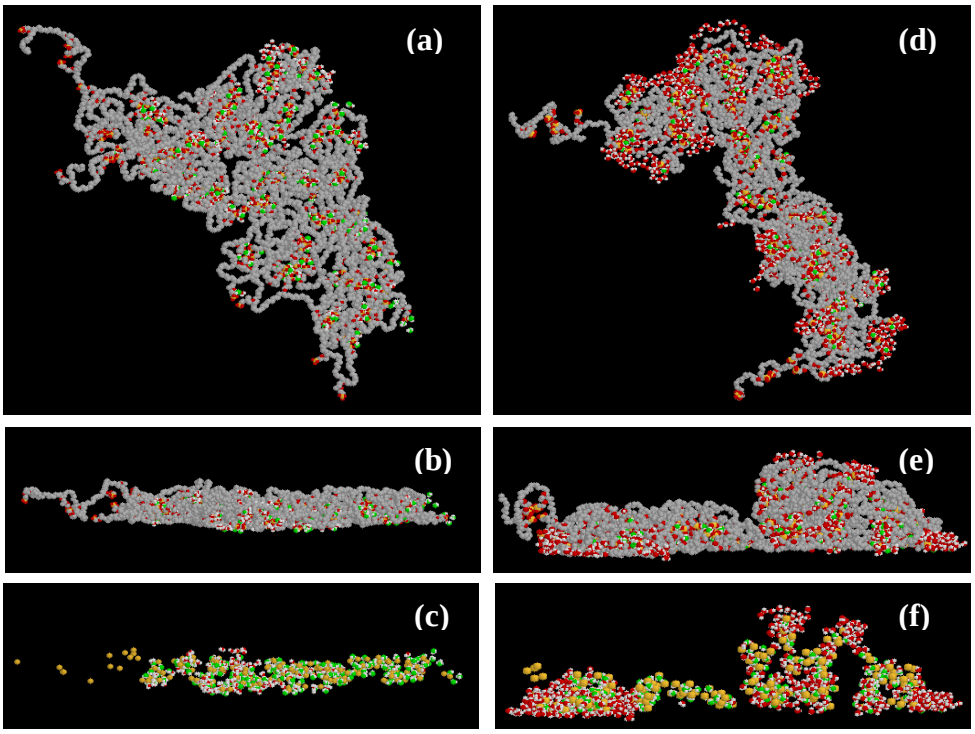

Figure 49 Snapshots of 1 nm Ionomer Film on 25% Epoxidized Carbon Surface.

A series of snapshots of the 1 nm Nafion film from the 25% epoxidized graphite system at hydration levels of $\lambda = 3$ and $\lambda = 9$. (a)-(b) are the top view and side view of the system of the hydrated Nafion film at hydration level of $\lambda = 3$. (c) is the same as (b) except the atoms from the Nafion polymer are not shown. (d)-(e) are the top and side view of the system at the hydration level of $\lambda = 9$. (f) is the same as (e) except the atoms from the Nafion polymer are not shown. The epoxidized graphite surface is not shown in the system for a better view. Color legend: grey is the united atom CF_x, green is oxygen in the hydronium ion, red is oxygen in water and Nafion, white is hydrogen and orange is the sulfur.

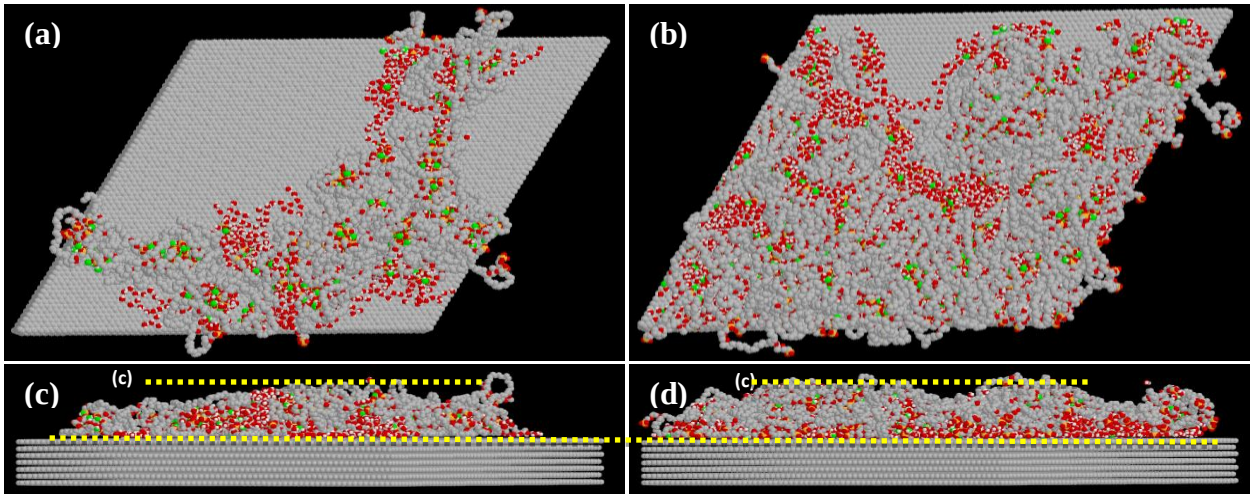

Figure 50 Snapshots of 1 nm and 2 nm Ionomer Film on Pristine Graphite Surface.

Snapshots of the hydrated Nafion films on the pristine graphite system at the hydration level of $\lambda = 9$. (a) top view of the 1 nm film (b) top view of the 2 nm film (c) side view of the 1 nm film (d) side view of the 2 nm film. Yellow dashed lines in (c) and (d) are the benchmark for film thickness and are separated by a distance of 2.6 nm. The water molecules located 7 Å away from the film are omitted for a clearer view. Color legend as in Figure 49 with the addition that graphitic carbon is gray.

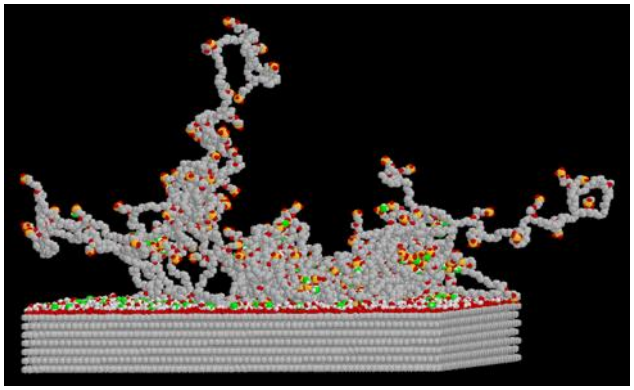

Figure 51 Partial Delamination of 1 nm Ionomer Film on 25% Epoxidized Surface.

Snapshots showing the partial delamination phenomenon of the 1 nm hydrated Nafion film on the 25% epoxidized graphite system at the hydration level of $\lambda = 3$. Color legend as in Figure 49.

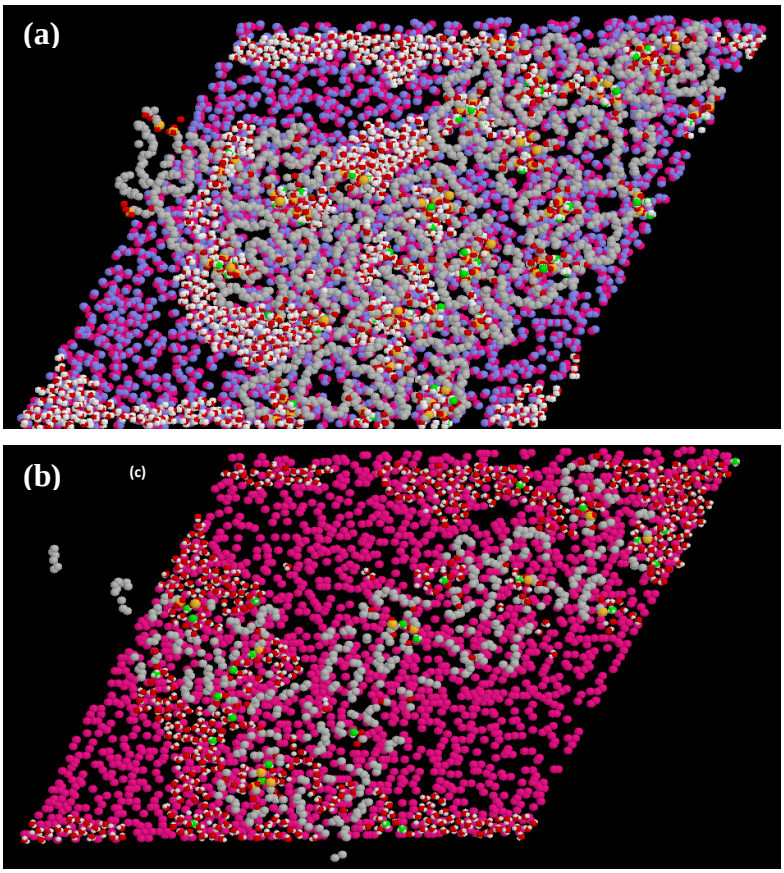

Figure 52 Interfacial Bonding of Sulfonic Acid Groups to the Oxidized Carbon Support.

Snapshots depicting the interfacial bonding of sulfonic acid groups to the oxidized graphite surface for the systems that contain a 1 nm thick Nafion film and the hydration level of $\lambda = 9$. (a) hydroxylated graphite surface (b) epoxidized graphite surface. The carbon represents graphite is hidden for a better view of the interfacial structure. Color legend as in Figure 49 with the additions that pink is the surface oxygen (hydroxyl or epoxy) and blue is the hydrogen from the hydroxyl group. Color of pink and blue are used instead of red (oxygen) and white (hydrogen) to avoid confusion with the water molecules on the surface. This is the only place that pink and blue are used to represent oxygen and hydrogen. One should not confuse this with the color legend in other figures.

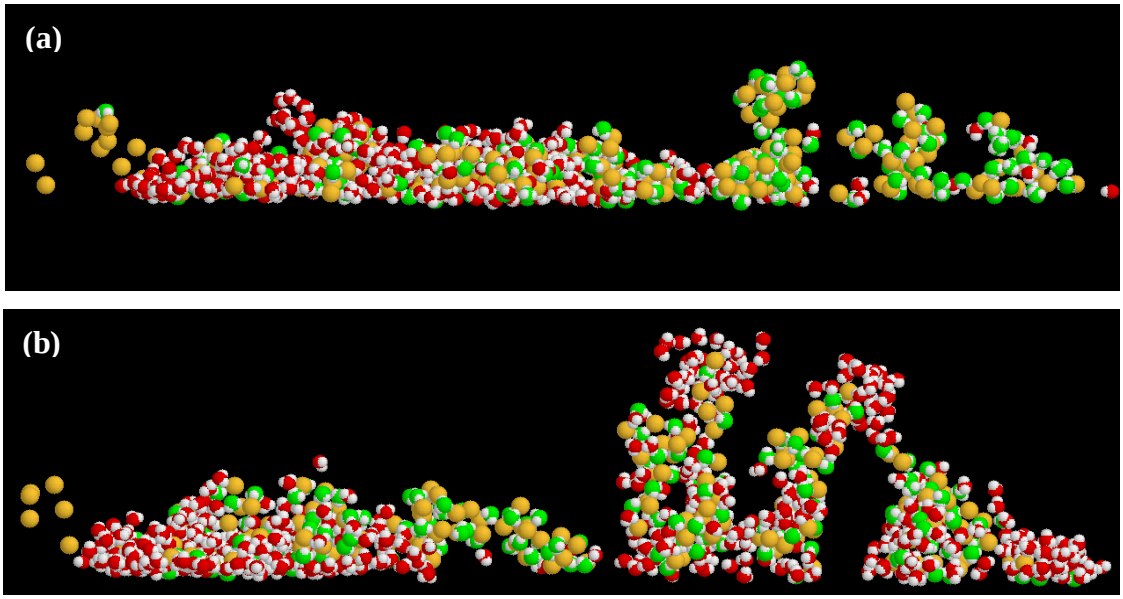

Figure 53 Snapshots Show the Water Molecules and Hydronium Ions within the Nafion Hydration Film

Snapshots show the water molecules and hydronium ions within the Nafion hydration film. The system studied contains the 1 nm thick Nafion film and the hydration level of $\lambda = 9$. Only the sulfur atoms from the Nafion film are shown in this pair of snapshots for a better view of the water and hydronium ions distribution. (a) 25% hydroxylated system (b) 25% epoxidized system. Color legend as in Figure 49.

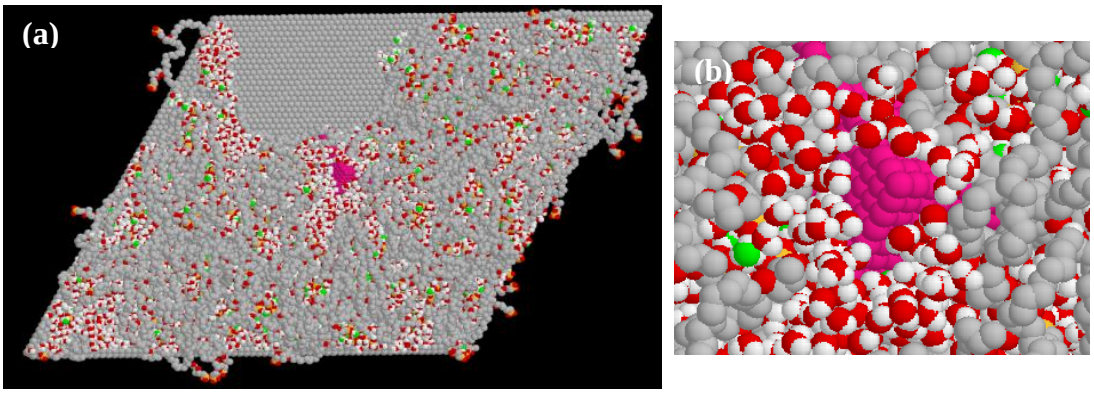

Figure 54 Snapshots Show the Water Distribution on the Pt Catalyst

Snapshots show the water distribution on the Pt catalyst. Water molecules that are not in the vicinity of Nafion film are hidden in the snapshot. The system studied is the 2 nm hydrated Nafion film on the pristine graphite surface at the hydration level of $\lambda = 9$ with a 4 nm Pt nanoparticle. The snapshot located on the right is the close up for the area around the Pt nanoparticle. Color legend as in Figure 49 with the addition that platinum is pink.

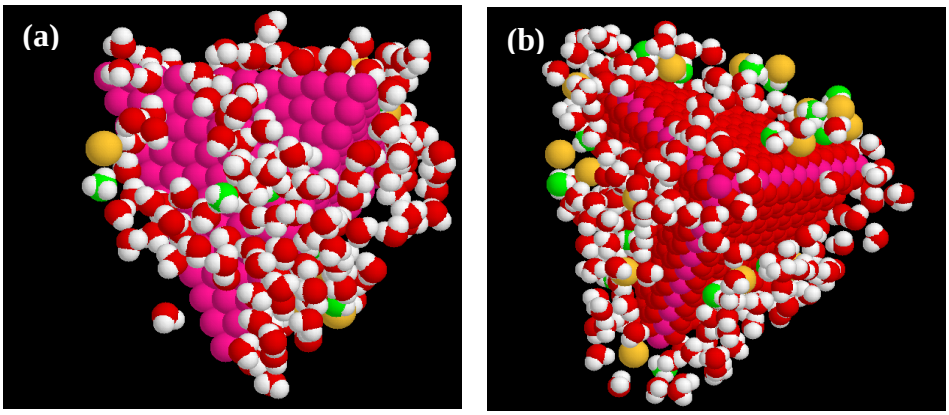

Figure 55 Snapshots Show the Differences in the Aqueous Domain Surrounding the Nanoparticles

Snapshots show the differences in the aqueous domain surrounding the nanoparticles. For clarity, water, hydronium ions and only the sulfur atoms of Nafion are shown. (a) Pt system. (b) PtO system. Color legend as in Figure 49 with the addition that platinum is pink and oxygen of PtO is red.

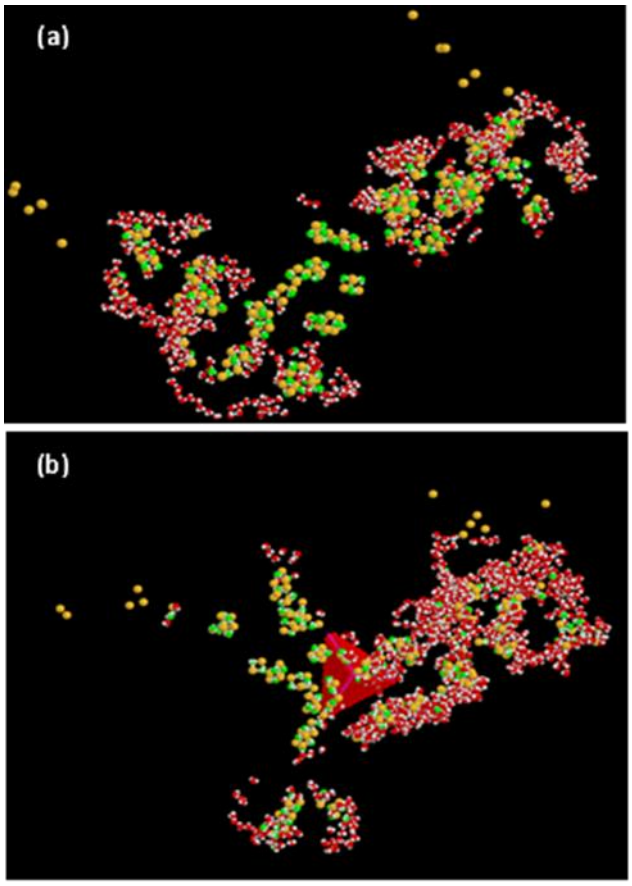

Figure 56 Snapshots Show the 25% Epoxidized Graphite System with the Hydration Level of λ = 9 and 1 nm Nafion Film

Snapshots show the 25% epoxidized graphite system with the hydration level of λ = 9 and 1 nm Nafion film. (a) no Pt system. (b) PtO system. The graphite surface is omitted and only water molecules, hydronium ions and sulfur atoms are shown in the hydrated film. Color legend as in Figure 49 with the addition that platinum is pink and oxygen of PtO is red.

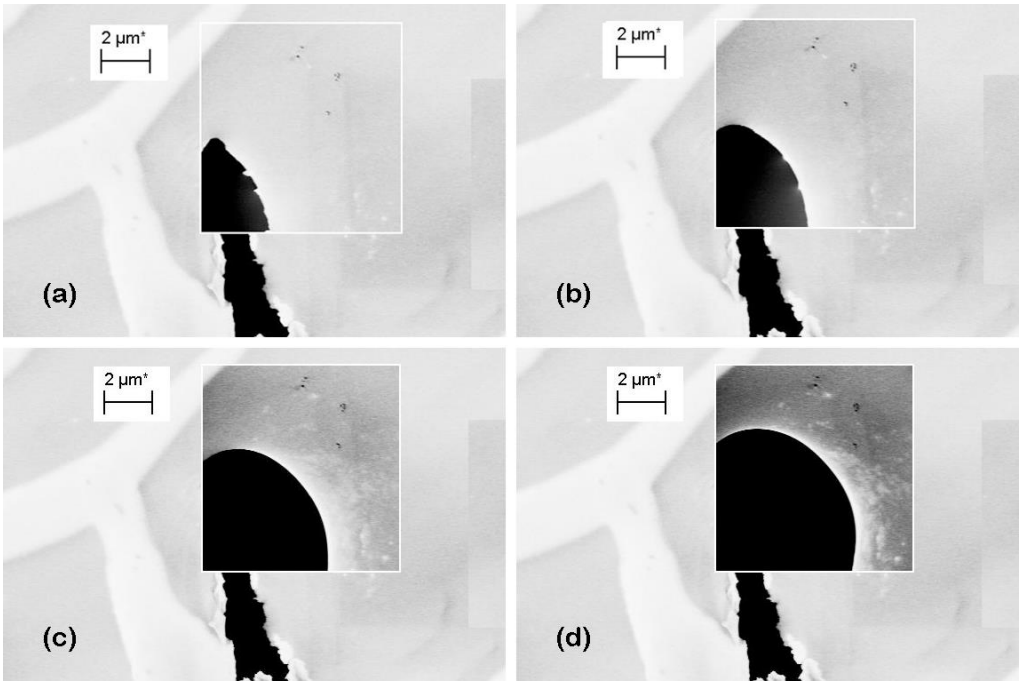

Figure 57 Radiation Damage of the 44 wt% Catalyst Layer Sample.

HAADF-STEM images (EHT = 15 kV scan speed = 35.30 $\mu m^2 s^{-1}$) of 44 wt% CL sample taken with the exposure time (t) increasing . (a) t=45 s. (b) t = 90s. (c) t = 196 s. (d) t = 271 s.

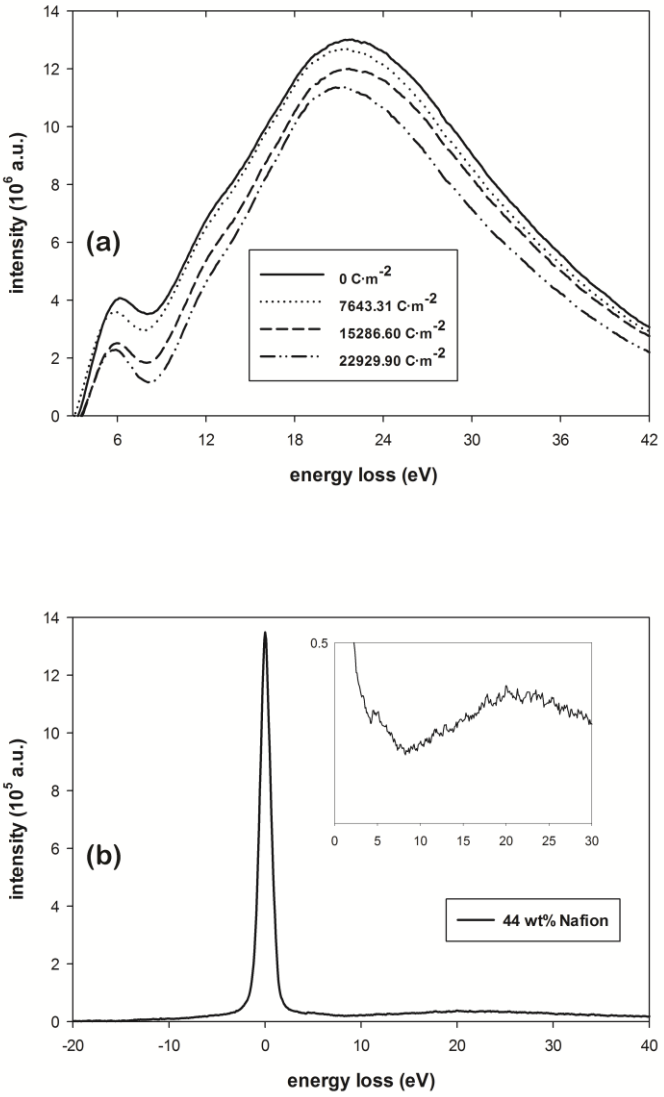

Figure 58 EELS Spectrums.

Low loss EELS spectrum recorded from 44 wt% Nafion CL sample. (a) Data below 3 eV are truncated because they are unreliable due to errors in zero-loss subtraction. (b) EELS spectrum including the zero-loss peak for the 44 wt% Nafion CL sample.

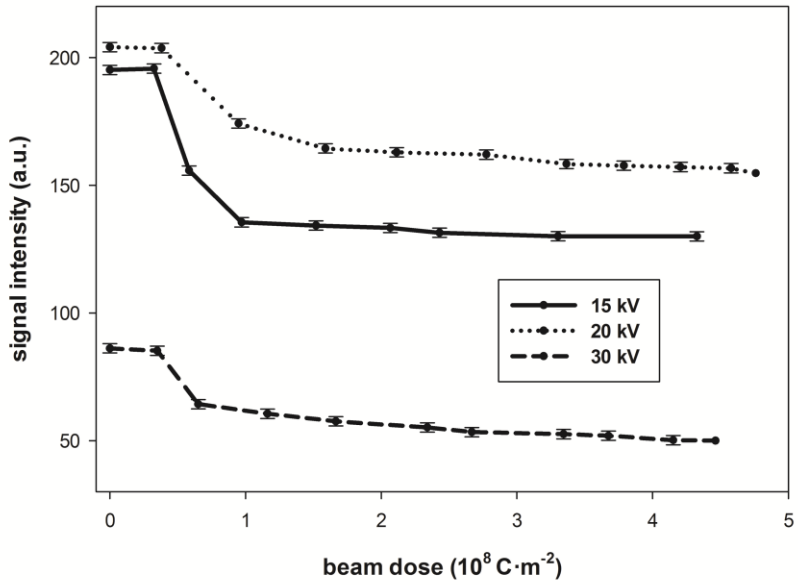

Figure 59 Effect of High Voltages on Signal Intensity Change.

Beam dose vs. signal intensity plots of 44 wt% Nafion CL samples at different high voltages for scan speed = 35.30 $\mu m^2 s^{-1}$.

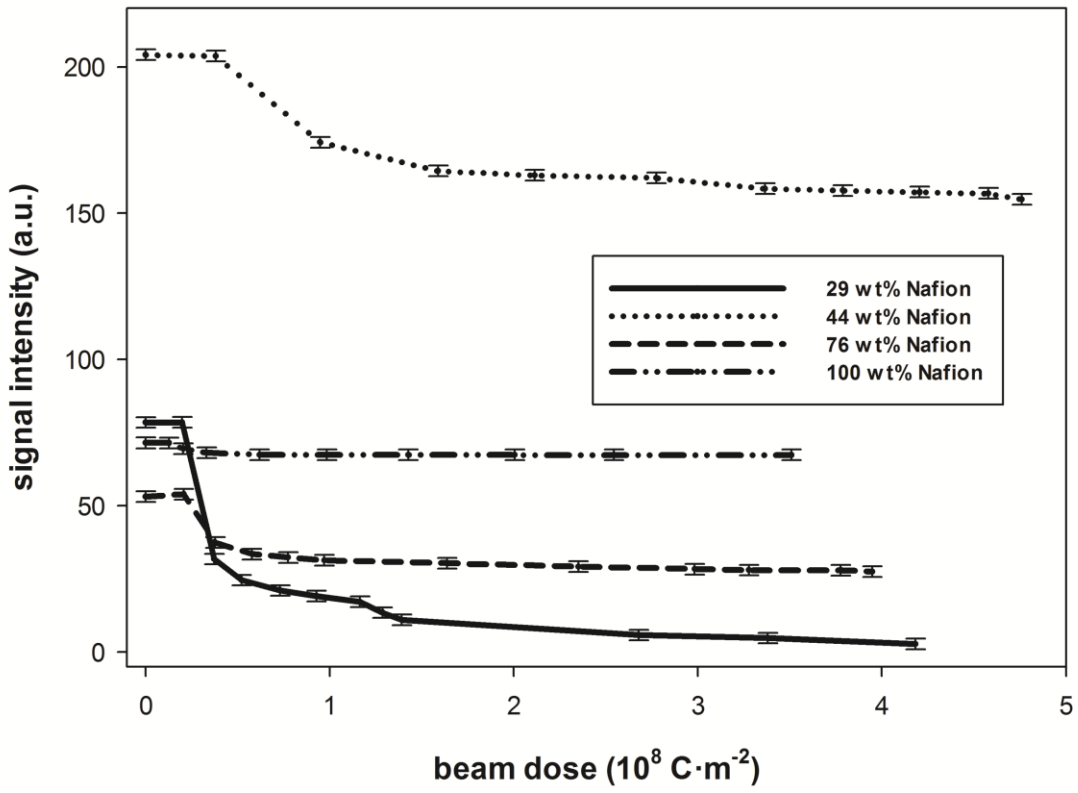

Figure 60 Effect of Nafion Composition on Signal Intensity Change.

Beam dose vs. signal intensity plots of samples of different Nafion composition for scan speed = 35.30 $\mu m^2 s^{-1}$.

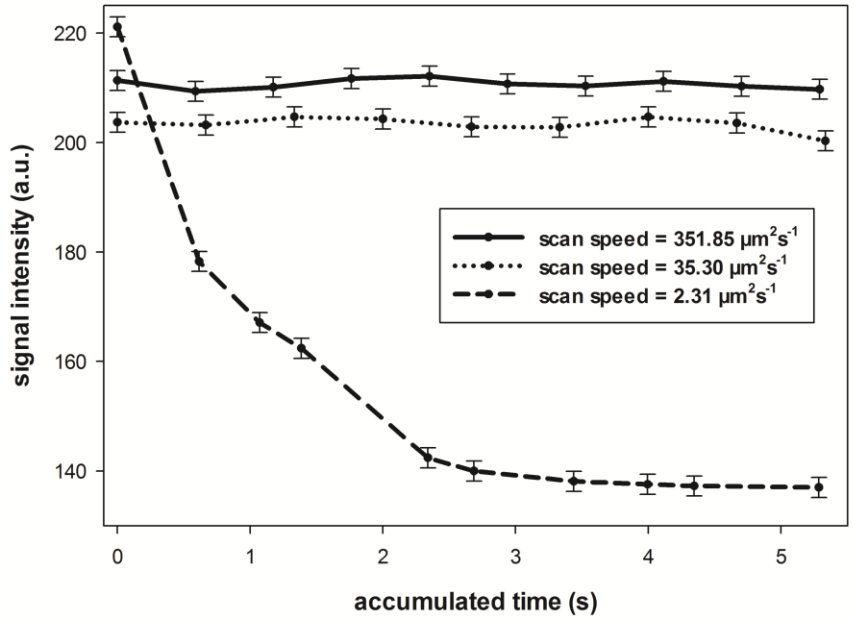

Figure 61 Effect of Scan Speed on Signal Intensity Change.

Beam dose vs. signal intensity plots of 44 wt% Nafion CL samples at different scan speeds.

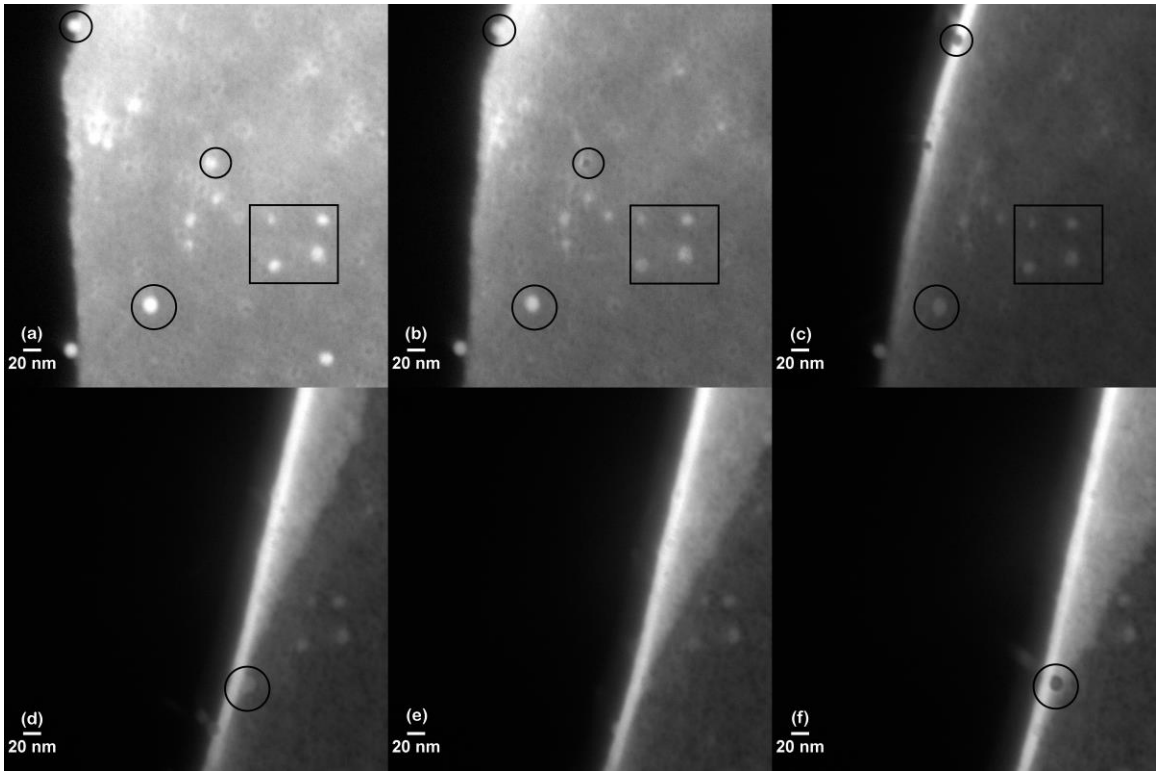

Figure 62 EFTEM Images Depict the Loss of Catalyst Nanoparticles.

EFTEM images of 44 wt% Nafion CL sample filtered at 57 eV. (a) –(f) are taken in a chronological sequence. The total elapsed time from frame (a) to frame (f) is 9 min.

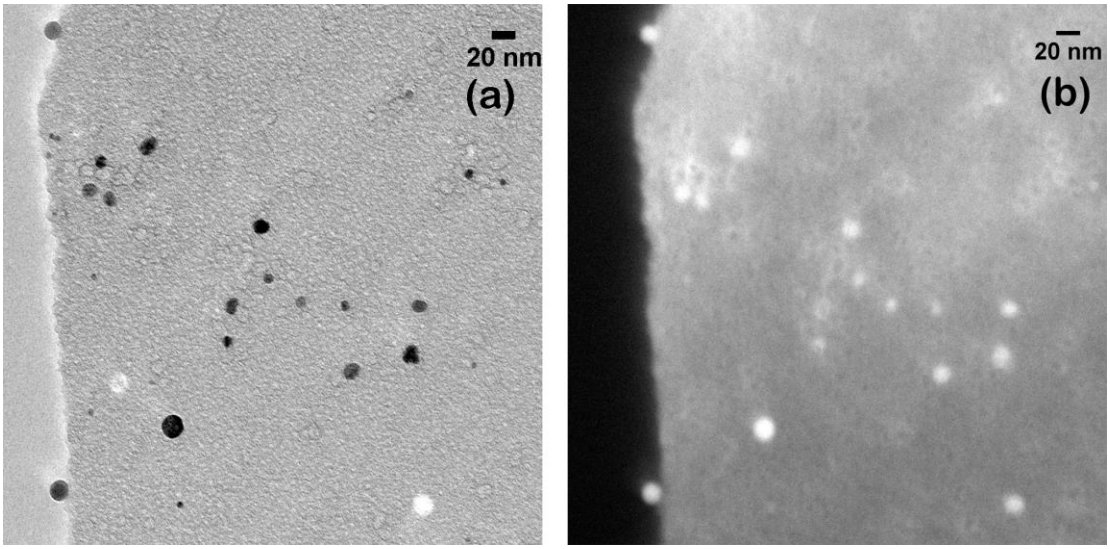

Figure 63 EFTEM images of 44 wt% Catalyst Layer Sample.

Comparison of EFTEM images of 44 wt% Nafion CL sample, (a) is filtered at 0 eV and (b) is filtered at 57 eV.

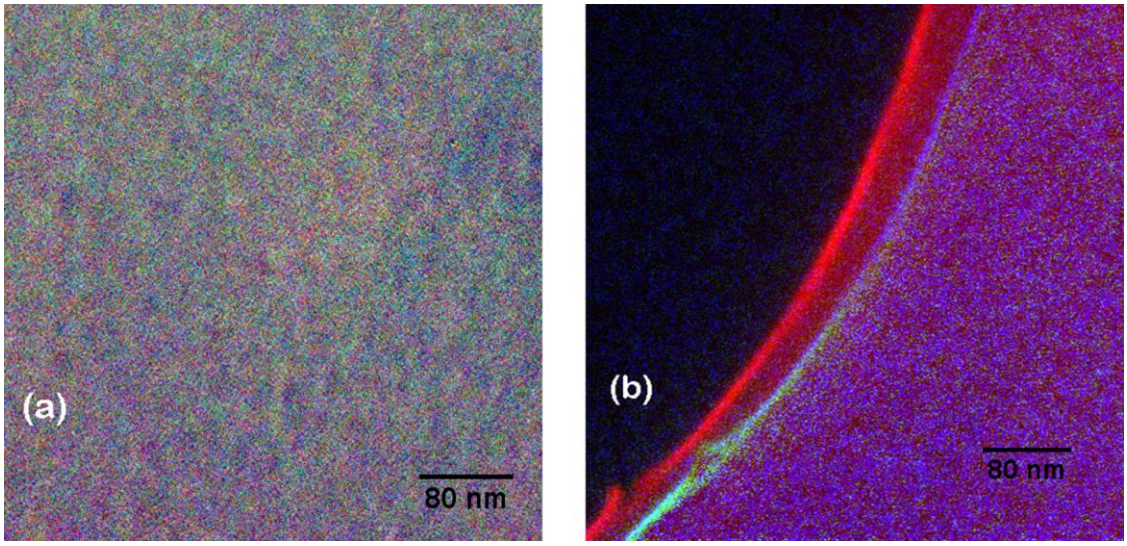

Figure 64 RGB Images Depict the Composition Change Before and After Radiation Damage.

RGB image of the 44 wt% Nafion CL sample before (a) and after (b) radiation damage. Red represents carbon, green is for fluorine.

VITA

Qianping He was born Feb. 28, 1984 in Zhuji, China. She is the first child of Fengling Yuan and Xinka He. She has a younger sibling Yingping He. She grew up in Shanghai and attended elementary and middle school there. She then went back to her home town to finish high school. In 2002, she was admitted to Zhejiang University of Technology and graduate four years later with a bachelor's degree in material science and engineering. In 2008, she came to the United States to continue her education with a master degree in chemical engineering and in 2009 she decided to quit the master program and pursue the Ph.D degree in chemical engineering in the University of Tennessee, Knoxville. She completed her Ph.D degree in Dec. 2013.